Spring 2005

Integrated modeling and parallel computation of laser-induced axisymmetric rod growth

Hong Lan

NOTE TO USERS

INTEGRATED MODELING AND PARALLEL COMPUTATION OF LASER-INDUCED AXISYMMETRIC ROD GROWTH

by

Hong Lan, M.S.

A Dissertation Presented in Partial Fulfillment
of the Requirements for the Degree
Doctor of Philosophy

COLLEGE OF ENGINEERING AND SCIENCE
LOUISIANA TECH UNIVERSITY

May 2005

LOUISIANA TECH UNIVERSITY

THE GRADUATE SCHOOL

02/04/2005
Date

We hereby recommend that the dissertation prepared under our supervision by Hong Lan

entitled Integrated Modeling and Parallel Computation of Laser-Induced Axisymmetric Rod Growth

be accepted in partial fulfillment of the requirements for the Degree of Doctor of Philosophy in Computational Analysis and Modeling

Raja Nassar
Supervisor of Dissertation Research

Richard J. Greechie
Head of Department

CAM
Department

Recommendation concurred in:

Advisory Committee

Approved:
Director of Graduate Studies

Approved:
Dean of the Graduate School

Dean of the College

GS Form 13
(5/03)

ABSTRACT

To fully investigate a pyrolytic Laser-induced chemical vapor deposition (LCVD) system for growing an axisymmetric rod, a novel integrated three-dimensional mathematical model was developed not only to describe the heat transport in the deposit and substrate, but also to simulate the gas-phase in the heated reaction zone and its effect on growth rate. The integrated model consists of three components: the substrate, rod, and gas-phase domains. Each component is a separate model and the three components are dynamically integrated into one model for simulating the iterative and complex process of rod deposition.

The gas-phase reaction is modeled by the gas-phase component, an adaptive domain attached on the top part of the rod. Its size and mesh decomposition is dynamically determined by the rod temperature distribution and the chosen threshold. The temperature and molar ratio are predicted and used to adjust the growth rate, by taking into account the diffusion limited growth regime, and to improve the simulation of entire deposition process. The substrate component describes the heat flow into the substrate, and the substrate surface temperature can be used to predict the initial rod growth which may affect the successive growth of the rod. The rod growth process is simulated using a layer-by-layer axisymmetric model. For each layer, the rod grows along the outward normal direction at each point on the rod surface. This simplified model makes the process more predictable and easier to control by specifying the height of the rod and the number of total iterations.

Finite difference schemes, iterative numerical methods, and parallel algorithms were developed for solving the model. The numerical computation is stable, convergent, and efficient. The model and numerical methods are implemented sequentially and in parallel using a standard C++ code and Message Passing Interface (MPI). The program can be easily installed and executed on different platforms, such as Unix and Windows XP. Computation in the gas-phase domain is encapsulated in a C++ class, and it is convenient for users to choose either the integrated or the kinetic model to perform simulation of rod growth. Parallel implementation improves the computational performance.

To demonstrate the capability of the integrated model, silane is chosen as the precursor to grow the axisymmetric rod with silicon as deposit and graphite as substrate. The integrated 3D LCVD model and the corresponding numerical methods are applied to simulate the gas-phase reaction process, and to predict heat transfer, molar ratio, initial and successive rod growths and growth time at each iteration. It is found that the diffusion-limited growth can affect the deposition process and must be taken into account when the temperature is higher than a certain threshold. The initial rod growth can affect the successive rod growth and its geometry. This modeling approach may provide a useful means for investigating the effect of different model parameters for optimizing the LCVD process.

APPROVAL FOR SCHOLARLY DISSEMINATION

The author grants to the Prescott Memorial Library of Louisiana Tech University the right to reproduce, by appropriate methods, upon request, any or all portions of this Dissertation. It is understood that "proper request" consists of the agreement, on the part of the requesting party, that said reproduction is for his personal use and that subsequent reproduction will not occur without written approval of the author of this Dissertation. Further, any portions of the Dissertation used in books, papers, and other works must be appropriately referenced to this Dissertation.

Finally, the author of this Dissertation reserves the right to publish freely, in the literature, at any time, any or all portions of this Dissertation.

Author Hong Lan

Date 02/04/2005

GS Form 14
(5/03)

TABLE OF CONTENTS

LIST OF TABLES

LIST OF FIGURES

NOMENCLATURE

English Symbols

A	species of deposit
AB_μ	molecule of precursor gas
B_μ	molecule of by-product
c	speed of light
c_D	heat capacity of deposit
c_S	heat capacity of substrate
C	constant
C_i	coefficient in the discrete scheme
D	gas diffusivity
D_{AB}	effective temperature dependent diffusion coefficient
e	base of logarithm
E_a	activation energy
G_r	Grashoff number
h	Planck's constant
h_{conv}	convective heat transfer coefficient
H_2	molecule of hydrogen
H_S	height of substrate
I_0	laser intensity

J_{loss} energy loss to the gas phase

K_0 growth rate constant

K_{des} thermodynamically limited rate constant

k_d thermal conductivity of deposit material

$k_D(T^D)$ temperature-dependent conductivity of deposit

k_{gas}, k_G thermal conductivity of gas species

$k_S(T^S)$ temperature-dependent conductivity of substrate

k_T thermal diffusion ratio

M number of elements in the r-direction

m the number of rows

n precursor concentration, the number of columns

$\hat{n}$ (x) unit normal vector

n_i index of reflection

N total particle density or the number of elements in the z-direction

N_{AB} particle density of species AB_μ

N_u Nusselt number

p precursor partial pressure, the number of processes

P laser power

P_0 average laser power

P_r Prandtl number

Q_{cond} heat loss rate due to conduction [J/s]

Q_{conv} heat loss rate due to convection [J/s]

Q_{in} heat input rate from light absorption [J/s]

Q_{rad} heat loss rate due to radiation [J/s]

Q''_{in} heat flux due to the distributed heat source [J/m^2s]

Q''_{loss} heat flux due to the distributed heat sink [J/m^2s]

Q'''_{in} distributed heat source [J/m^3s]

Q'''_{loss} distributed heat source [J/m^3s]

r radius

r_i coordinate at index i on the z axis

r_s steady state radius in the reaction zone

r_w reaction zone radius

R universal gas constant

R_g radius of gas phase domain

R_n normal deposition rate

R_0 axial deposition rate

R_s radius of substrate

Si molecule of silicon

SiH_4 molecule of silane

t time

T temperature

T_G gas-phase temperature

T_s surface temperature

T^D temperature of deposit

T^S temperature of substrate

T_{th} threshold temperature

T_∞ ambient temperature

W_S width of substrate

X_{AB} molar ratio of species AB_μ

z paraxial position along beam focus, height or coordinate

z_0 Reyleigh range of focused beam

Z_g height of the gas phase domain

Greek and Other Symbols

Υ deposit volume per unit surface area

α_T a constant.

ν average gas velocity

$\Gamma(z)$ wavefront radius of curvature

δT_{th} width of threshold temperature

ΔH_{des} enthalpy of the deposition

$\Delta\vec{Z}(x,y)$ local normal deposit growth

Δt time interval

ε_s surface emissivity

θ convergence angle

Θ Temperature excess

λ wavelength of light

Λ angular spectral absorbance

μ ligand in precursor gas AB_μ

ρ_D density of deposit

ρ_S density of substrate

σ Stephan-Boltzman constant

σ_1 standard deviation of the intensity distribution of the laser beam

ϕ incident angle from the surface normal vector

ω beam waist radius or over-relaxation factor

ω_0 beam waist radius at focus

$\Im$ angular spectral reflectance

∇^2 Laplace operator

∇ del operator

Ω computational domain

$\partial\Omega_1$ outer boundary

$\partial\Omega_2$ inner boundary

φ a parameter

Superscript

D deposit material

S substrate material

Subscript

∞ ambient condition, or infinity norm

i index of grid in the r-direction

j	index of grid in the z-direction
μ	ligand in precursor gas AB_μ

ACKNOWLEDGMENTS

With the achievement of the terminal degree in my life, I am grateful to all the people who have contributed to this dissertation.

First and foremost, it is a great honor to express my deep gratitude to my advisor, Dr. R. Nassar, for his guidance, assistance, encouragement, and support in all steps of my doctoral program. Also, I especially thank my co-advisor, Dr. W. Dai, for his outstanding insights and valuable suggestions for the quality of my dissertation. They were always patient, thoughtful and available throughout my Ph.D. study. I would also thank the members of my committee, Dr. R. Greechie, Dr. V. Phoha, and Dr. A. Paun, for taking time to read my dissertation and to make this work a reality.

This dissertation is dedicated to my husband, Chaoyang Zhang, for his inexhaustible support and assistance from prelims to defense and through several stops along the way, and my lovely sons, Benny and Max, for their pride in me and for showering me with their unconditional love through all my moods.

This dissertation is also dedicated to my parents. They gave me the foundation to start the journey when they gave me my first book and the courage to continue even when the journey was difficult.

CHAPTER 1

BACKGROUND AND OBJECTIVES

1.1 Background

With the development of Microstructure Technology (MST), microstructures with dimensions smaller than 1 millimeter are new products used in consumer, industrial, IT and medical applications. Micromachining, the production technology behind MST, is based on processing originating from the semiconductor industry. Typical devices have features smaller than feasible by traditional manufacturing techniques, with dimensions measured in micrometers, sometimes in nanometers, and rarely in millimeters.

The fabrication of three-dimensional microstructures includes processes such as etching and deposition. Laser-induced Chemical Vapor Deposition (LCVD) is an emerging technique in freeform fabrication of high aspect ratio microstructure with many practical applications [Bäuerle 1986].

To develop a micro scale freeform fabrication process, a laser beam is used as an energy source to induce precipitation of a solid material from a surrounding medium. Precursors for freeform fabrication must be chemicals which can be modified, dissociated, or decomposed in such a way that at least some portion of the precursor molecule solidifies, precipitates, or adsorbs onto an evolving part surface when the

induction factor is applied, thereby forming the part. The decomposition of precursor molecules in LCVD can be activated thermally or non-thermally or by a combination of both. The type of process activation can be verified from the morphology of the deposition and from measurements of the deposition rate as a function of laser power, wavelength, and substrate materials.

LCVD results in the deposition of material in a microscopic heated region created by a focused laser beam. The process has extraordinary capabilities that derive from the small size of the heated reaction zone, a unique mechanism for precise control of the thermal deposition near the focus of a laser beam, and direct control of the direction in which deposition occurs.

While much progress has been achieved in recent years in the fabrication of microstructures, there remain some constraints. Current processes are limited both in the part shapes that can be manufactured and in the materials that can be exploited.

Analytic solutions can be obtained under some assumptions [Kirchenko 1990] [Bäuerle 1990] [Brugger 1972] [El-Adawi 1986] for some simple cases. However, it is impossible to develop a general three-dimensional mathematical model to completely describe the correlation between temperature and deposit growth and derive its exact solution. Usually, for each specific physical problem one should develop a simplified mathematical model and solve it using a numerical method.

Several studies in the literature are related to numerical simulations related to deposit spot, rod growth, direct writing of a line, or surface scanning in two-dimensions [Arnord 1993] [Maxwell 1996] [Lan 2003] [Zhang 2003]. In this simulation, the laser beam is focused on one fixed point, or scans all the pixels on the surface of the substrate

or deposit according to a specified pattern. However, in different temperature regions, the growth rate of deposit is different. Therefore, this growth rate, depending on the temperature, can be kinetically limited or mass transport limited. To produce a microstructure with high resolution, a model considering both kinetically limited and mass transport limited growth should be developed for process control and optimization.

In this dissertation, mathematical models are developed for 3D-LCVD with kinetically limited and mass transport limited reactions. These models are then implemented to deposit pyrolytic graphite, and silicon, in order to form a three-dimensional shape rod. This rod form is a building block for more complex microstructures.

1.2 Research Objectives

The goal of this research is to study the transport and thermal phenomena that underlie the 3D-LCVD process and to simulate the process for fabricating a rod using LCVD with both kinetically-limited and diffusion limited reactions, so that the deposit geometry can be predicted during pyrolytic growth for given process conditions and material properties.

Three-dimensional LCVD is a very complicated process. The surface temperature determines the reaction region and the growth rate of the deposit. Growth changes the shape of the deposit and the concentration of the precursor gas, which in turn affects the surface temperature of the deposit. This dual relationship between growth and temperature makes it difficult to solve the problem analytically. Hence, numerical analysis must be employed.

In this dissertation, a three-dimensional mathematical model is developed to describe the heat transport in the deposit and substrate as well as the heat exchange at the interface. This model describes the temperature distribution and growth and for both kinetically limited and diffusion limited reactions.

A differential method shall be applied to discretize the governing equations. An effective numerical method, stable and convergent for iterative calculations, will be developed for solving the coupled equations in the three-dimensional mathematical model.

An example involving deposition of silicon on a graphite substrate is selected to demonstrate the application of the model. From this model, it is possible to determine the temperature distribution on the surface of deposit, the temperature distribution in the reaction zone, and the geometry of the deposited rod. Results of this model will contribute to process control and optimization for microstructure fabrication.

1.3 Organization of the Dissertation

This dissertation contains a three-dimensional mathematical model that combines both kinetically limited and mass transport limited reaction. Since the mathematical model is for simulating the physical phenomena by numerical methods, not only the numerical methods but also the physical principles and mechanisms underlying the physical phenomena need to be understood and expressed correctly. The numerical methods corresponding to the mathematical model should be stable and convergent. After the mathematical model and numerical methods are developed and verified, they are applied to simulate specified physical problems.

The structure of this dissertation is as follows:

Chapter 2 provides the necessary technical background. A review of LCVD is given with emphasis on the deposit and growth rates for kinetically limited and mass transport limited reactions.

Chapter 3 presents details of the three-dimensional LCVD mathematical model for generating a microstructure considering kinetically limited reactions.

Chapter 4 proposes an integrated rod growth model considering both kinetically limited and mass transport limited reactions, derives the coupled governing equations and investigates all model components and their data flows.

Chapter 5 provides numerical methods corresponding to the mathematical model. The numerical scheme, iteration algorithm, and computation details are given.

In chapter 6, parallel algorithms are designed and implemented with standard C++ and MPI for solving the integrated rod growth model to achieve high performance.

In chapter 7, the three-dimensional model and corresponding numerical methods are applied to simulate the LCVD process for generating a silicon rod microstructure. The model results include prediction of the temperature distribution on the surface of the rod, temperature distribution of the reaction zone, and rod shape.

Chapter 8 presents discussion and conclusions.

CHAPTER 2

INTRODUCTION TO LCVD

2.1 LCVD

Laser chemical vapor deposition (LCVD) is an important technique in free-form fabrication of high aspect ratio microstructures. The system consists of a laser beam, a vacuum chamber, and a movable stage, as shown in Figure 2.1.

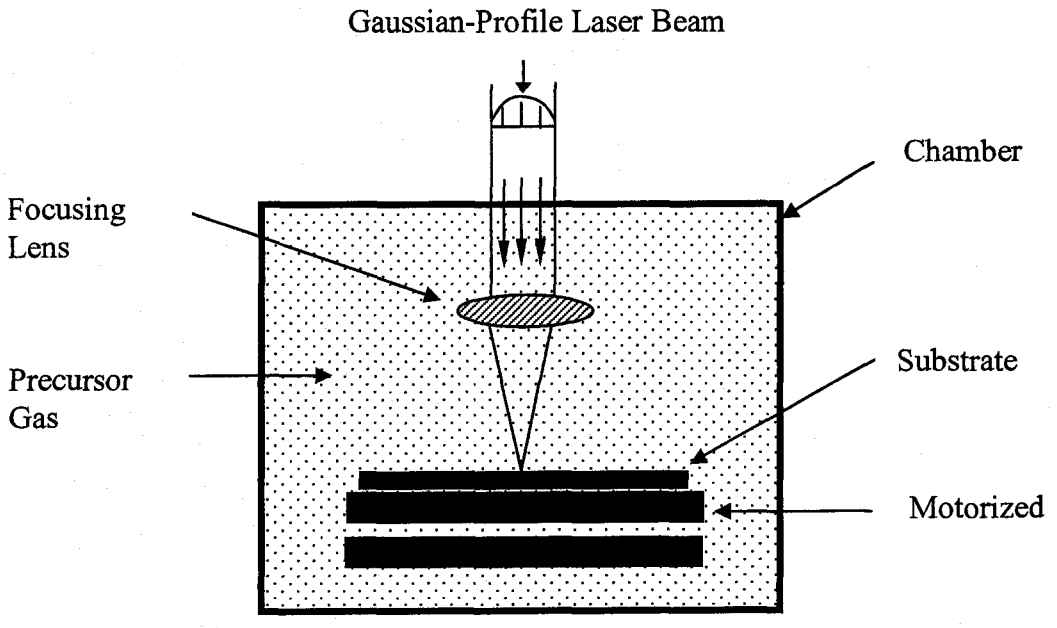

Figure 2.1 LCVD Schematic

The laser beam (usually of Gaussian profile) is the heat source. It is focused through a chamber window onto a substrate target. The reactive gas is introduced into the chamber. When the temperature increases, the reactive gas reacts at or near the focal spot on the substrate, leaving behind the solid-phase reaction product (deposit). The laser induces this decomposition by either thermal- or photo-excitation. Precursors are chosen so that the by-products of the reaction are volatile and return to the surrounding gas mixture. If the focal spot is scanned across the substrate, a trace of material is left behind, in a manner similar to other rapid prototyping systems, and microstructures with different pre-specified shapes can be manufactured. A rod can be obtained if the laser beam is focused at a fixed point on the surface of the substrate or deposit.

2.2 LCVD Mechanism

LCVD is carried out through three possible mechanisms of precursor dissociation: photolytic, pyrolytic and a combination of both processes. The emphasis in this research is on pyrolytic LCVD.

2.2.1 Photolytic LCVD

Photolytic deposition is usually the slower of the two. It occurs when the precursor compound is dissociated directly by light, the incident photons breaking the molecular bonds of the compound through their absorption. Depending on the precursors employed, both single and multi-photon excitations may be required to drive the photolytic dissociation reactions.

Photolysis of a precursor gas is generally carried out in a parallel or a direct-write orientation of the beam relative to the substrate. In the parallel configuration, the beam is parallel to the substrate, whereas it is incident in the latter. The parallel configuration is

employed to grow blanket deposits across a wafer, and is often denoted by photo-assisted CVD. The direct-write process is essentially the same as the photo-assisted CVD, and deposition occurs only near the focus of the beam where dissociated radicals diffuse to the deposit surface from the gas-phase, and/or adsorbed precursor molecules are dissociated on the substrate surface [Maxwell 1996][Nassar 2002].

Photolytic deposition rates of organametallic compounds are usually several orders of magnitude smaller than pyrolytic deposition rates. Thus, photolytic LCVD can create very thin metallic film at relatively low temperatures. For this reason, photolytic LCVD has been used for the customization and repair of integrated circuit (IC) interconnects. Direct-write photolysis qualifies as a freeform fabrication process, although the comparatively small volumetric deposition rates do not justify its use for the manufacturing of MEMS products.

2.2.2 Pyrolytic LCVD

Pyrolytic deposition, on the other hand, operates through absorption of a precursor onto a substrate (or deposit) surface and subsequent thermal dissociation of the compound through heating of the solid surface. In this case, the substrate is chosen to be absorptive of the light, and the precursor is chosen to be transparent to the incident radiation. The mechanism of pyrolytic LCVD is represented in Figure 2.2, where a heated reaction zone, of radius r_w, is generated by a laser beam of radius, ω_0, focused on the substrate.

Pyrolytic deposition generally occurs at much higher rates (often by several order of magnitudes than its photolytic counterpart). Pyrolytic reaction occurs at the surface only within the laser heated reaction zone, and the surface temperature outside of this

region is assumed to be below the threshold temperature, T_{th}, for deposition. The local deposition rate at each surface point is determined by the temperature at the surface, the activation energy and the ability of the precursor reactants, and by-products to transport to and from the surface. When a reactive gas reacts in the reaction zone, it leaves behind any solid-phase reaction product, which leads to the growth of the deposit. At the same time, precursor by-products desorb from the growth surface and diffuse into the ambient.

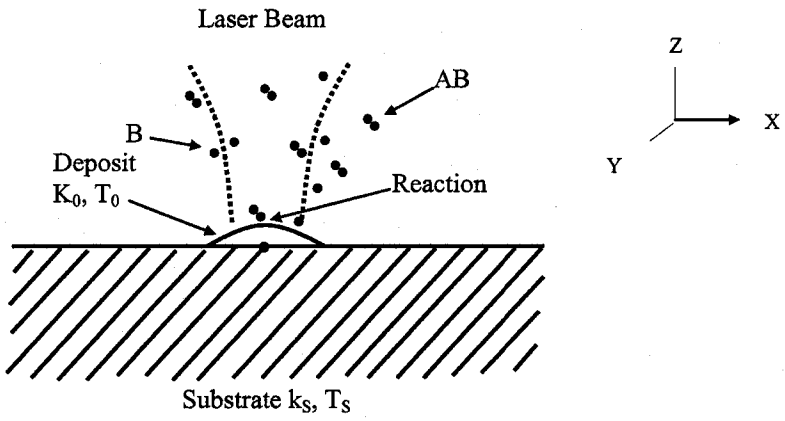

Figure 2.2 Pyrolytic Deposition

In most cases, precursors used in LCVD are of the form, $P = AB_\mu$, where A is a metal or element to be deposited, and B_μ are μ ligands loosely bound to B. Usually B is chosen such that it is not likely to remain as a by-product in the solid deposit, giving a pure deposit of A. The reaction of gas-phase molecules AB_μ shall be heterogeneous, i.e. it shall occur exclusively on the surface r_s. Here, species A condenses on the surface r_s and either forms the deposit or it reacts further, while atoms/molecules B immediately desorbs from the surface.

$$AB_\mu \rightarrow \cdots \rightarrow A(\downarrow) + \mu \cdot B(\uparrow) \tag{2.1}$$

More details about the reaction kinetics in laser-induced pyrolytic chemical processing can be found in [Bäuerle 1986, 1990]. In this dissertation, silane is chosen as the precursor, $P = SiH_4$. The pyrolytic CVD reaction can be described by the sequence of reactions:

$$SiH_4 \rightarrow \cdots \rightarrow Si(\downarrow) + 2H_2(\uparrow) \tag{2.2}$$

Here, as each SiH_4 molecule decomposes, one molecule of silicon (Si) and two molecules of hydrogen H_2 are produced. H_2 diffuses away from the reaction zone, i.e. in the opposite direction of SiH_4. This counter-diffusion of the reaction product influences the transport properties within the ambient medium, and thereby the overall reaction rates within the reaction zone.

2.3 Deposition Rates

The deposition rate is the most important factor in evaluating the ability of any LCVD process for fabricating a 3D microstructure. While the surface temperature drives the deposition rate of a heterogeneous pyrolytic reaction, the rate obtained depends on the reaction activation energy and the ability of the precursor reactant and by-product to transport to and from the surface.

Based on the surface temperature, the reaction rate falls into three areas. When the reaction rate is limited by the activation energy and temperature, the process is termed kinetically limited. When the precursor and by-product diffusion control the rate, the reaction is termed mass transport limited. For an exothermic reaction at high temperature, the reaction is termed thermodynamically limited. Figure 2.3 presents the three deposition rate limited regimes corresponding to the temperature variation.

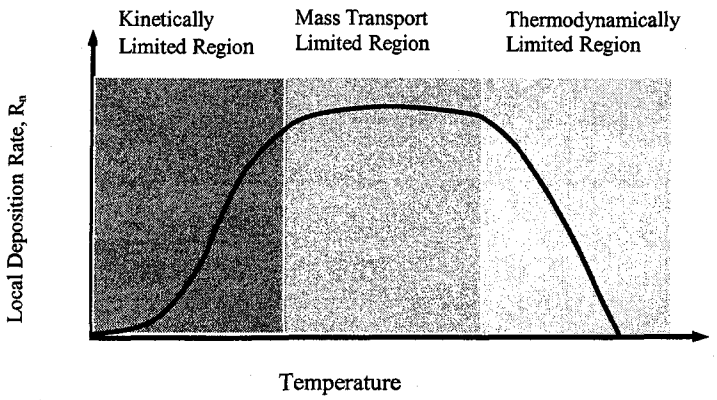

Figure 2.3 Deposition rate limited regimes

Usually a process is kinetically limited at low temperature and pressure, the reaction rate rising exponentially with increasing temperature. Eventually, as the reaction proceeds, relative conversion in the reaction zone becomes insufficient to support the continued exponential increase with temperature, and the deposition rate levels off.

2.3.1 Kinetically Limited Rates

A typical deposition rate vs. surface temperature is shown in Figure 2.3. This relation follows the Arrhenius equation below [Bäuerle 1990],

$$R_n = K_0(p,T)e^{-E_a/(RT)} \tag{2.3}$$

where K_0 is a concentration-dependent rate constant, p is the pressure, and E_a and R are the activation energy and the universal gas constant.

The local deposit rate, R_n, is prescribed only by the surface temperature, T, and the activation energy E_a. R_n is strictly defined as the magnitude of the rate at any given surface point, and is known as the normal deposit rate, where the vector $\vec{R}_n$ lies along the normal to the surface.

2.3.2 Mass Transport Limited Rates

When the surface temperature increases to a certain level, the process passes into the mass transport limited (or diffusion-limited) regime. The reaction proceeds rapidly enough and the relative conversion of reactants becomes large. The ability of the precursor to arrive at the surface of the reaction zone is insufficient to support the continued exponential increase with the increasing temperature. Hence, the deposit rate level no longer depends on Equation (2-2), but rather on the precursor concentration, n, given by the diffusion equation [Maxwell 1996],

$$D\nabla^2 n - \frac{\partial n}{\partial t} = 0 \tag{2.4}$$

where D is the diffusivity.

Different geometries of the deposit give rise to different solutions to this partial differential equation.

Once transport limitation commences, the hottest portions of the deposit grow at a constant rate while the edges grow at a kinetically limited rate. This process may result in non-uniform deposits.

2.3.3 Thermodynamically Limited Rates

For exothermic reactions at high temperatures, the free energy becomes less negative with temperature, thereby slowing the deposition rate. A process can be thermodynamically limited for several reasons. Often it is caused by an increase in the apparent activation energy due to the greater desorption of the precursor (or its intermediates) with temperature; i.e., the precursor desorbs before it can react. In this case the reaction rate can be modeled by the Langmuir-Hinshelwood equation:

$$R_n = \left(K_0 p^2 e^{-\frac{\Delta H_a}{RT}} \right) \Big/ \left(K_{des} e^{-\frac{\Delta H_{des}}{RT}} + p \right) \qquad (2.5)$$

Here, K_{des} and ΔH_{des} are the rate constant and the enthalpies of the deposition, respectively. If the pressure is very high, or the temperature moderates, the Langmuir-Hinshelwood rate reduces to an Arrhenius Reaction as presented in Equation (2.3) [Maxwell 1996].

2.3.4 LCVD Process Parameters

LCVD deposition is a process involving thermal, physical, and continuum mechanics. Determination of the deposition rate is the most important factor in modeling an LCVD process. The LCVD deposition rate is a function of many factors: laser fluence, vapor pressure, local temperature, activation energy, and conductivities of deposit and substrate.

As described before, an LCVD process may contain three regimes. In the kinetically limited regime, according to the Arrhenius law, the local deposit rate rise exponentially based on the surface temperature of the deposit. The heat transfer in the deposit and substrate depends on the laser beam conditions, surface properties, and fluid conditions. Laser beam conditions include laser power, laser intensity profile, wavelength, and spot/line geometry. Surface properties include optical absorption, reflectivity and emissivity, reflection index, material thermal conductivity, surface geometry and roughness. Fluid conditions include Nusselt Number, Reynolds Number, Grashoff Number, Prantle Number, and thermal conductivity of the fluid. These fluid parameters determine the thermal physics and continuum mechanics of the gas phase in the reaction zone.

When the temperature reaches a high value, mass transport becomes diffusion limited, convection limited, and surface limited. The diffusion limited case includes gas diffusivities, concentrations, size of the reaction zone, and gas temperature. The convection limited case includes Sherwood number, Schmidt number, Reynolds number, and concentrations. The surface limited case includes absorption and nucleation.

In the following chapters, more details on the LCVD process parameters will be given.

2.4 Theoretical Investigations

The microscopic mechanism and the growth rate involved in LCVD have been introduced briefly in the previous documentation. LCVD is a process that combines both physical and chemical processes that involve heat transfer, mass transfer, and chemical reactions. An overview of the theoretical solution for a pyrolytic LCVD will be given in this section. Also, some theoretical results on the kinetics and mass transport of the chemical process will be introduced.

The LCVD process is a complex mechanism relating surface temperature to the reaction rate, and deposit geometry. However, the problem can be simplified under certain assumptions. Arnold considered laser direct writing of a stripe onto a semi-infinite substrate under quasi-stationary conditions where the coordinate system was fixed with the laser beam, so the geometry of the stripe remains unchanged [Arnold 1993]. Details of a one-dimensional analytic solution for this problem, and self-consistent model calculations on pyrolytic laser direct writing were given. However, this approach ignores the gas-phase transport and assumes a purely heterogeneous reaction. As such, the model applies to laser direct writing of thermally well-conducting strips onto insulating

substrates. Results of these calculations were compared with experimental data on the direct writing of W lines.

The 3D LCVD problem can be simplified to a 2D LCVD problem for an axisymmetric shape. The temperature profile along the deposit height need to be determined to obtain the shape of any axisymmetric deposit. Some simplifications need to be made to obtain a solution. One simplification is to assume that the heat flux into and out of the deposit is in equilibrium by neglecting the time-dependence of the heat-flow. Another simplification is to assume that the conductivities of deposit and substrate are constants.

Under these assumptions, the diffusion equation may be expressed as [Maxwell 1996]

$$k_d \nabla^2 \Theta + Q'''_{in}(x,r,t) - Q'''_{loss}(x,r,t) = 0 \qquad (2.6)$$

where Θ is the temperature access, and Q'''_{in} and Q'''_{loss} are the distributed heat sources and sinks at or within the deposit boundaries. They can be due to absorption of the laser light, or convective/radiative losses at the deposit surface.

For an axisymmetric deposit of arbitrary profile, *r(x)*, where the height of the deposit is typically much greater than its width, it is reasonable to assume that the temperature gradient is largely one-dimensional along the axial x-coordinate. For a Gaussian beam absorbed completely at a rod tip, and for simultaneous convection and radiation from the rod surface, the temperature may be derived numerically from the expression:

$$\frac{d^2\Theta}{dx^2} + \frac{2}{r(x)}\frac{dr(x)}{dx}\frac{d\Theta}{dx} = \left(\frac{2}{k_d r(x)}\right)Q''_{loss}(x,r,t) - \left(\frac{2}{k_d r(x)}\right)Q''_{in}(x,r,t) \qquad (2.7)$$

where Q''_{in} and Q''_{loss} are the heat fluxes, $Q''' = Q'' / \gamma$, and γ the deposit volume per unit surface area.

If one ignores the spatial distribution and time variance of the laser input at the tip of the rod, and if radiation as a source of heat loss is ignored, then the temperature along the length of the deposit, $T(x,t)$ can be solved analytically.

Based on the temperature approximation in Equation (2.7), a simple rod growth simulation can be obtained which qualitatively describes the form of the rods deposited from various precursor chemistries [Maxwell 1996]. Beginning with a set of seed points that describe the initial deposit surface, the model calculates the unit normal to a curve passing through all points in the set, and then each point is successively translated according to the Arrhenius relation given in Equation (2.3). A simulation of graphite rod growth was presented, showing different stages in the evolution of a rod. This result was compared with experimental results from ethylene pyrolysis. In all cases, the simulation closely approximates the actual growth profiles, with the exception that the actual rods were somewhat broader and flattened near the tip. These deviations from the predicted kinetic shape may be explained by the mass transport limitation at the rod tip.

A mathematical model for heat transfer in the substrate during LCVD in which the three-dimensional and transient heat conduction equation is solved for a slab having finite dimension and moving at a constant velocity is given by Kar [Kar 1989]. The temperature-dependent thermophysical properties of the material of the slabs are considered, and both convective and radiative losses of energy from the slab to the surrounding medium are taken into account. The laser beam is considered to be Gaussian in shape. The three-dimensional nonlinear governing equation is linearized by using the

Kirchoff's transformation and then solved by successively applying the Fourier-transformation in the x, y, and z directions. Based on these considerations and techniques, an analytic expression for the three-dimensional and transient temperature field is obtained. Thermal analysis can provide information on the variation of film width with laser power and scanning speed, and the upper and lower limits of the operating scanning speed for LCVD processes. For a given laser power, the peak temperature varies linearly with the scanning speed of the laser beam on the log-log scale. Also, the peak temperature varies linearly with the laser power on the linear scale for a given scanning speed of the laser beam. Unfortunately, in some cases the deposit growth may greatly influence the temperature distribution of the substrate. This paper studied only the three-dimensional transient heat transfer in the substrate and did not include the deposit.

A mathematical model considering the influence of counterdiffusion on the reaction rate is presented by Kirichenko [Kirichenko 1990], in which investigations of a steady-state transport phenomena in laser-induced non-equimolecular heterogeneous gas-phase reaction are given. In this model, several assumptions were given, namely a semi-infinite substrate, the geometry of the surface is independent of time, steady state conditions, and the reaction zone is represented as a hemisphere whose surface temperature is uniform. For the isothermal gas-phase case, one assumes that the gas-phase is at a uniform temperature. Also, the total particle density and the diffusion coefficient were assumed to be constant. In this model, an analytic expression for the concentration of gas-phase molecules in a hemispheric deposit is presented, and the reaction rate is obtained. The paper presented only the gas-phase molecule concentration

and reaction rates for one specific deposit shape and but excluded the heat transfer in the deposit and substrate.

In general, for some simple physical problems with simple boundary conditions, analytic solutions can be obtained [Brugger 1972], [El-Adawi 1986], [Bäuerle 1990], and [Kirichenko 1990]. However, for arbitrary structures and conditions, analytic solutions are not possible, and the coupled equations for growth, gas diffusion, and heat flow must be solved numerically in three-dimensions.

2.5 Numerical Simulation

Numerical models of the deposition process are few. [Bäuerle 1984] used a finite element method to simulate the temperature rise for the system of nickel deposited on a quartz substrate. This model does not permit the modeling of irregularly shaped deposits. [Allen 1986] used a finite difference technique to model the growth of a nickel film on a quartz substrate. The gas phase diffusion was neglected. [Maxwell 1996] presented a mathematical model based on a stationary laser focal spot to predict the transport and thermal phenomena that underlie the three-dimensional LCVD process. Based on his study, a numerical model for simulating an axisymmetric rod growth was obtained [Dai 1999] and [Lan 2003] used a finite difference method to model the fabrication of 3-D convex and concave microlenses. Growth was assumed to be kinetically determined with no gas diffusion limitation. [Skouby 1988] used a finite element technique to model the growth of film including diffusion. However, it was assumed that the film acted merely as a laser power attenuator for the substrate and ignored the temperature distribution in the solid.

2.6 Conclusions

Use of lasers as a material processing tool has led to many applications. As described in the literature, much work has been done to simulate the LCVD process. From these mathematical models, one can examine the effects of various parameters on the performance of the process.

Accompanying the rapid progress in the application of LCVD in microfabrication, it is necessary to develop a model that can predict the laser beam dwell time across the substrate to obtain solid deposit considering both kinetic and diffusion effects. Because of the complexity of the process of LCVD, no mathematical model can completely simulate all its physical and chemical properties. However, mathematical modeling may provide some useful information for experimental control and application by simulating the LCVD process and predicting the influence of various parameters and different conditions on its performance.

Some research work has been done in mathematical modeling of LCVD, in which either diffusion is not considered or the diffusion effect is processed in a simplified manner.

To obtain a deposit with both kinetic and diffusion effects, one should know the laser power, the laser beam distribution, the solid deposit temperature distribution, and the diffusion zone temperature distribution. One may use mathematical modeling to predict the effects of these physical parameters on growth of the deposit. Little research work has been done to simulate such a problem.

In this study, a mathematical model and a corresponding numerical method will be developed to generate a laser-induced chemical vapor deposit on a substrate considering both kinetic and diffusion effects.

CHAPTER 3

A KINETICALLY LIMITED 3D LCVD MODEL

A three-dimensional (3D) laser-induced chemical vapor deposition (3D-LCVD) process will be explored in this chapter. A mathematical model will be presented which describes the heat transfer in the deposit and substrate, and predicts the shape of a 3D microstructure. In this chapter, we do not consider the kinetics in the gas phase and the mass transfer limitation. The emphasis in this chapter is on the analysis of kinetically limited growth rates. A strong correlation exists between the geometry of the deposit and the laser-induced temperature distribution in an LCVD process. To obtain the temperature distribution, it is critical to determine the chemical reaction zone and the growth rate on the surface of the substrate.

3.1 Physical Description

The temperature rise induced by the absorbed laser radiation on a material surface or within its bulk is one of the basic quantities in laser processing. Therefore, knowledge of the temperature distribution is a prerequisite for both fundamental investigations and technical applications. When the laser beam (usually of a Gaussian profile) is focused in a chamber onto a substrate target, the surface temperature and hence the growth rate is determined by the balance of heat flow into and out of the deposit. In LCVD, heat losses

are through radiation, convection, and conduction to the substrate. The laser power absorbed at the deposit surface, in conjunction with heat losses, drives the reaction and determines how the surface temperature will change over time. Figure 3.1 shows the three primary mechanisms that contribute to heat loss in 3D-LCVD.

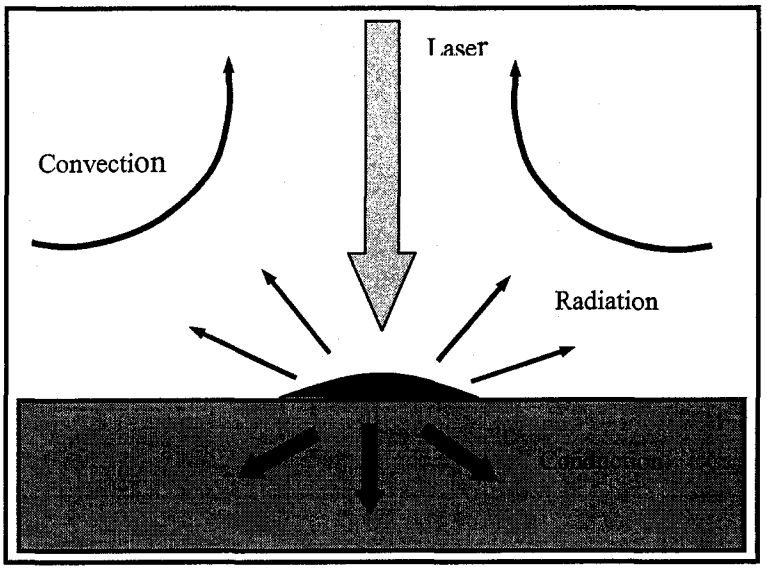

Figure 3.1 Conductive, Radiative and Convective Heat Losses

The simple continuity expression describes the balance of the heat flow through the deposit boundaries:

$$Q_{in} = Q_{cond} - Q_{conv} - Q_{rad} \tag{3.1}$$

where Q_{in} represents the heat transfer rate from the absorbed laser fluence, Q_{conv} the heat loss rate due to convection, Q_{rad} the loss rate from radiation, and Q_{cond} the heat conduction rate. These four terms will be discussed in the following sections.

3.1.1 Gaussian Laser Beam

The power delivered to the surface determines the local surface temperature, and hence the growth rate and deposit shape. Among the most important beam shapes employed in laser processing is the Gaussian beam. The spatially-dependent intensity of a laser beam can be obtain from the solution of the equation for the propagation of paraxial waves, defined a

$$I(r,z) = I_0\left[\frac{\omega_0}{\omega(z)}\right]^2\left[e^{-\frac{2r^2}{\omega^2(z)}}\right] \tag{3.2}$$

where I_0 is the peak beam intensity (i.e., the power density), $\omega(z)$ is the $1/e^2$ beam waist radius at any axial position z, and ω_0 is the $1/e^2$ spot radius at the focus. In terms of the average laser power, P_0, within a circle of ω_0 radius, the peak intensity becomes

$$I_0 = \frac{2P_0}{\pi\omega_0^2} \tag{3.3}$$

The spatially-dependent intensity at the focal plane may be written as

$$I(r,z) = \frac{2P_0}{\pi\omega^2(z)}\left[e^{-\frac{2r^2}{\omega^2(z)}}\right] \tag{3.4}$$

Integrating Equation (3.4) over r, one obtains that the power delivered to a surface at the focal plane within a circle of radius, r, is

$$P(r,z) = P_0\left[1 - e^{-\frac{2r^2}{\omega^2(z)}}\right] \tag{3.5}$$

If r is equal to $\omega(z)$ in Equation (3.5), $P(r,z)=0.86P_0$, which means the total power delivered to a surface within a $1/e^2$ spot size is 0.86 P_0.

As an incident beam passes into the surface of a solid, the radiation is attenuated, some of it is reflected, and the rest is eventually absorbed or completely transmitted. The optical absorption and attenuation coefficients of the deposit and substrate materials may be critical in determining the absorbed heat flux. In this dissertation, it will be assumed that the laser light not reflected at a gas-solid boundary is transmitted into the solid and eventually completely absorbed within the solid. Let $\Im$ be the spectral reflectance at the gas-solid boundary, and n_i the deposit index of the reflection. Then the angular spectral absorption coefficient, Λ, is given by:

$$\Lambda = 1 - \Im(\phi) \tag{3.6}$$

where ϕ is the local incidence angle, and $\Im(\phi)$ is the angular spectral reflectance defined by [Seigel 1992]:

$$\Im(\phi) = \frac{1}{2}\left\{\left[\frac{\cos\phi - \sqrt{n_i^2 - \sin^2\phi}}{\cos\phi + \sqrt{n_i^2 - \sin^2\phi}}\right]^2 + \frac{n_i^2\cos\phi - \sqrt{n_i^2 - \sin^2\phi}}{n_i^2\cos\phi + \sqrt{n_i^2 - \sin^2\phi}}\right\} \tag{3.7}$$

The deposit index of refraction n_i, can be obtained from Smell's law. This expression is valid only for a randomly polarized beam, and a given wavelength, λ.

The heat transfer rate, Q_{in}, at the surface of deposit or substrate can be specified as a function of the radial distance from the centerline, r, and the angle of incidence, $\phi(r)$, to the unit surface normal vector, $\hat{n}(x,r,t)$. Assuming a Gaussian incident beam and absorption over a surface, from Equations (3.2) and (3.4), we can obtain an approximate expression for the heat flux Q_{in}'':

$$Q_{in}''(r) = 2P_0\frac{\Lambda[\phi(r)]}{\pi\omega^2(z)}e^{-\frac{2r^2}{\omega^2(z)}}(\hat{z},\hat{n}(x)) \tag{3.8}$$

To obtain the heat transfer rate, Q_{in}, in Equation (3.1), the expression in Equation

(3.8) should be integrated over the absorption surface, s. From Equations (3.6) to (3.8), one can calculate the heat transfer rate, Q_{in}. Note that the shape of deposit will influence the heat transfer rate. In the case where the deposit shape is changing over time, the exact solution to Equation (3.8) must be obtained iteratively with the equation of growth over time since the reflectance depends on the shape, and the induced temperature depends on the reflectivity.

3.1.2 Natural Convection

The rate of heat convection from a solid body into a surrounding medium can be described by:

$$Q_{conv} = A_s h_{conv}(T_s - T_\infty) \tag{3.9}$$

where A_s is the surface area of a heated body, h_{conv} is the convective heat transfer coefficient, and T_s is the body surface temperature.

Using the following relation, h_{conv} can be determined from the dimensionless Nusselt number, N_u,

$$h_{conv} = N_u \frac{k_{gas}}{2r_s} \tag{3.10}$$

where k_{gas} is the thermal conductivity or the heat transfer coefficient of the dominant gas species.

The Nusselt number, which represents the ratio of convection to the conduction losses, is an empirical expression that depends on the dimensionless Grashoff and Prandtl number, G_r and P_r. The Grashoff number is a measure of the ratio of buoyancy to viscous forces in the precursor gas. The Prandtl number is the ratio of the kinematic viscosity to the thermal diffusivity. The Nusselt number in Equation (3.10) is of the form, for a given body geometry,

$$N_u = C + f(G_r + P_r) \tag{3.11}$$

where C is a constant which depends on the body geometry.

The heat loss rate depends on the geometry and size of the body. For instance, heat loss from a rod during 3D-LCVD depends on the rod's radius and length. An empirical formulation has been widely accepted for the laminar Nusselt number over a sphere:

$$N_u = 2 + 0.43(G_r + P_r)^{1/4}. \tag{3.12}$$

For a rod less than 1000μm in diameter, the Nusselt number can be approximated to an accuracy of 15% by the non-zero value:

$$N_{u\,sphere} \approx 2. \tag{3.13}$$

When natural convection occurs over a solid cylinder of uniform temperature, the Nusselt number will be of the form:

$$N_u = 0.36 + f(G_r + P_r). \tag{3.14}$$

For small Grashoff number,

$$N_{u\,cylinder} \approx 0.36. \tag{3.15}$$

Above formula is a crude approximation to the actual situation where the shape may be parabolic or even dimpled; however, it is adequate for the purpose of this dissertation.

3.1.3 Radiation

Radiation from a blackbody surface into a medium of refractive index, n_i, can be described by the Planck's distribution, which gives the spectral emission vs. wavelength, λ, and surface temperature, T_s:

$$Q''_{rad}(\lambda, T_s) = \frac{2\pi n_i^2 hc}{\lambda^5 (e^{(hc)/(\lambda T_s)} - 1)} \tag{3.16}$$

Here, h is Planck's constant, and c is the speed of light in a vacuum. Assuming a deposit of emissivity ε_s, and integrating Equation (3.16) over all wavelengths, one arrives at the Stephan – Boltzmann equation for hemispherical total emissive power (where σ is the Stephan – Boltzmann constant):

$$Q''_{rad}(T_s) = \varepsilon_s n_i^2 \sigma T_s^4 \ . \tag{3.17}$$

For the hemispherical geometry of a rod tip, the heat loss rate, Q_{rad} due to radiation into an infinite region filled with a precursor gas of refractive index, n_i can be estimated from [Maxwell 1996]:

$$Q_{rad}(T_s) = (\frac{4}{3})\pi r_s^2 \varepsilon_s n_i^2 \sigma (T_s^4 - T_\infty^4) \ . \tag{3.18}$$

For a deposit with arbitrary geometry, one can obtain the heat loss due to radiation from Equation (3.17) and the surface area.

3.1.4 Discussion

For the growth of the deposit on the substrate, there exist several stages. At the initial stage, heat conduction to the substrate is dominant since the deposit surface area is generally small and as such radiation and convection are insignificant. Once a deposit forms, the laser beam will hit the surface of the deposit and the temperature then depends on the optical and thermal properties of both deposit and substrate. During the transient growth regime, conduction to the substrate diminishes. As a result, the properties of the substrate become less important, and eventually it can be assumed that conduction in the rod is one-dimensional or linear. For an insulated deposit on a highly conductive substrate, a large linear gradient over the rod will result. However, for a conductive

deposit on an insulated substrate, the base temperature will be high, and little gradient will occur over the rod. If the conductivity k_d of the deposit is much larger than the conductivity k_s of the substrate, it is difficult to grow a relatively long rod, since the entire rod would grow outward and broaden the rod.

In the case of graphite, nickel, and iron, the thermal conductivity drops with temperature; Beginning at about 20 ~ 200K, it falls continuously until the Curie point (just below the melting point). This process further isolates the heated zone and increases the peak temperature, which in turn further lowers the conductivity. As a result, the growth terminates at some height from the substrate where the peak temperature exceeds the melting point [Maxwell 1996].

3.2 Governing Equations and Boundary Conditions

In the LCVD process the balance of heat flow into and out of a deposit determines the surface temperature and hence the growth rate.

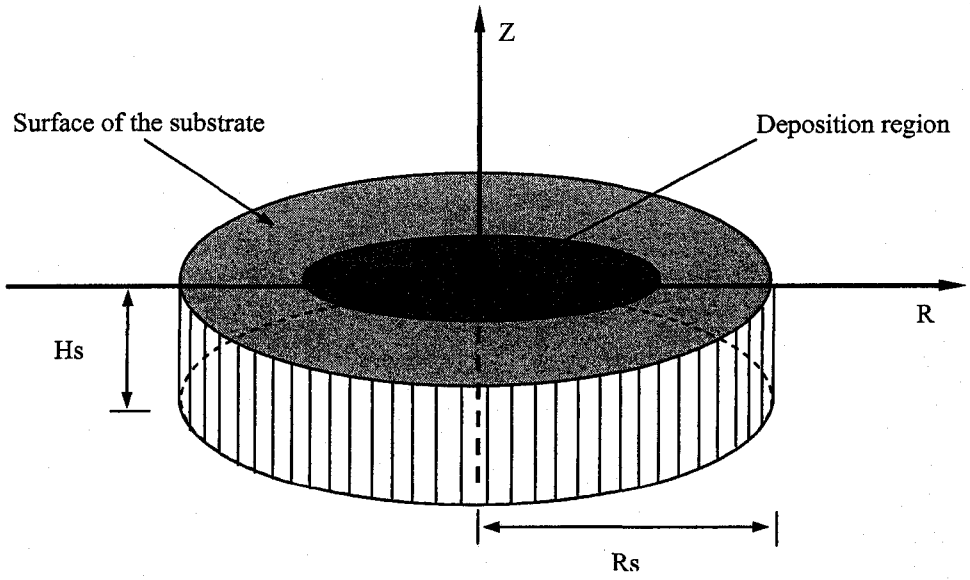

Figure 3.2 Cylindrical coordinate system for the substrate

We consider a round stationary substrate with the laser beam hitting in the center of the surface of the substrate. The deposit region and the substrate in a cylindrical coordinate system are shown in Figure 3.2.

We can assume that the substrate is insulated and the heat transfer on the interface of the deposit, and substrate can be ignored if the conductivity of the substrate is much smaller than that of the deposit. This assumption can simplify the calculation but limits the application range of the model. A three-dimensional heat transfer equation is used to describe the LCVD process. Our model contains heat transfers in the deposit and substrate as well as that on their interface, so it can be used to study the temperature profile for different deposit and substrate materials.

3.2.1 Deposit Temperature

Based on the heat equation, the temperature distribution induced by the absorption of laser radiation within the solid can be calculated. In most cases, the temperature is a function of both the spatial coordinates and time. With fixed laser parameters, the temperature distribution depends on the optical absorption within the irradiated zone, on the transport of heat out of this zone and, if relevant, on the transformation enthalpies for, melting, vaporization, and on chemical reaction enthalpies (exothermal or endothermal). In this study, we ignore the transformation and chemical reaction enthalpies. In a coordinate system, the heat equation that describes the heat flow through the deposit can be written as

$$c_D(T^D)\rho_D(T^D)\frac{\partial T^D}{\partial t} - \nabla[k_D(T^D)\nabla T^D] = Q_{in} - Q_{loss} \tag{3.19}$$

where $T^D \equiv T^D(z,r,t)$ is the temperature of the deposit at any point (z,r), in the

cylindrical coordinate system, and any time t. The parameters $\rho_D(T^D)$, $c_D(T^D)$ and $k_D(T^D)$ denote the temperature-dependent density, heat capacity and thermal conductivity of the deposit, respectively. ∇ is the three-dimensional del operator. Q_{in} is the heat source at or within the deposit boundaries due to the absorption of the laser beam light, and Q_{loss} is heat loss.

The interfacial equations between the deposit and the substrate are

$$T^D = T^S \tag{3.20a}$$

$$k_D(T^D)\frac{\partial T^D}{\partial z} = k_S(T^S)\frac{\partial T^S}{\partial z} \tag{3.20b}$$

On the surface of the deposit

$$-k_D(T^D)\frac{\partial T^D}{\partial z} = J_{loss} \tag{3.21}$$

where J_{loss} describes the energy loss to the gas phase on the surface of the deposit.

3.2.2 Substrate

The heat in the deposit will be transferred to the substrate through the interface once the solid is deposited on the surface of the substrate. We can assume that the substrate is isolated and the heat transfer on the interface of the deposit and substrate can be ignored if the conductivity of the substrate is much smaller than that of the deposit. If the ratio of the thermal conductivities of deposit and substrate is not too large, the heat transfer to the interface cannot be ignored since it will influence the temperature distribution of the deposit and hence the growth rates and the shape of the deposit. The energy transfer equation that describes the heat flow through the substrate is given by

$$c_S(T^S)\rho_S(T^S)\frac{\partial T^S}{\partial t} = \nabla[k_S(T^S)\nabla T^S] \tag{3.22}$$

where $T^S \equiv T^S(z,r,t)$ is the temperature of the substrate at any point (z,r), in the Cylindrical coordinate system, and at any time t. $\rho_S(T^S)$, $C_S(T^S)$ and $k_S(T^S)$ denote the temperature-dependent density, heat capacity and thermal conductivity of the substrate, respectively, and ∇ is the three dimensional del operator.

The initial condition ($t = 0$) is

$$T^S = T_i^S \tag{3.23}$$

where T_i^S is the initial temperature of the substrate.

3.2.3 Growth Rates

A complete 3D-LCVD model should include both growth kinetics and diffusive transport of the precursors. In this section, the emphasis is on the thermalphysics occurring during the 3D-LCVD process. The diffusive transport of the precursors will be discussed later in this chapter. The governing equations for heat flow through the deposit and the substrate can be used to predict the temperature distribution. Based on the temperature distribution on the surface of the deposit, one can predict the deposit growth rate from the Arrhenius law, Equation (2.3). The geometry of the deposit will affect the growth in the actual LCVD process. From a macroscopic viewpoint, one may assume that growth during 3D-LCVD occurs along the instantaneous normal vector at each point on the surface of an evolving deposit. While the temperature may affect the magnitude of growth at each point, the direction of deposition remains normal to the surface due to the nature of the diffusion, adsorption, nucleation, and coalescence processes that produce polycrystalline or amorphous deposits. The exception to this rule is the deposition of

single crystals, where growth may indeed be anisotropic due to lattice activation. For the following analysis, this normal-growth rule is assumed, so the growth is a normal vector that can expressed as follows:

$$\Delta\vec{z}_n(z,r) = K_0 e^{-\frac{E_a}{RT^D}} \Delta t \cdot \hat{n}(z,r) \tag{3.24}$$

where $\Delta\vec{z}_n(z,r)$ is the local deposit growth at a point on the surface of the deposit, K_0 is a concentration-dependent rate constant that can be determined empirically, E_a and R are the activation energy and universal gas constant, respectively. Δt is the time increment to obtain a deposit growth $\Delta\vec{z}_n(z,r)$. $\hat{n}(z,r)$ is the unit outward normal vector on the instantaneous surface of deposition.

Equation (3.24) can account for the threshold behavior of the deposition process. Only if the surface temperature T^D exceeds the threshold temperature does deposition become significant.

3.3 Modeling of a Rod Microstructure

In the previous section we described the governing equations and corresponding boundary conditions. These equations can be used for simulating the 3D-LCVD processes in different situations, such as a spot, rod, direct writing, and so on. However, many factors regarding the governing equations may affect the temperature distribution and the growth rate. The complex interrelation among the heat flow between the deposit and substrate, the temperature field, and the deposit growth, makes it hard to obtain a satisfactory solution. One should simplify the above governing equations for different kinds of physical problems to reach the goal of predicting the shape of an axisymmetric rod.

3.3.1 Problem Description

By simplifying the above governing equation, we can develop an effective mathematical model to simulate the growth of an axisymmetric rod. We consider an axisymmetric rod deposit as shown in Figure 3.3.

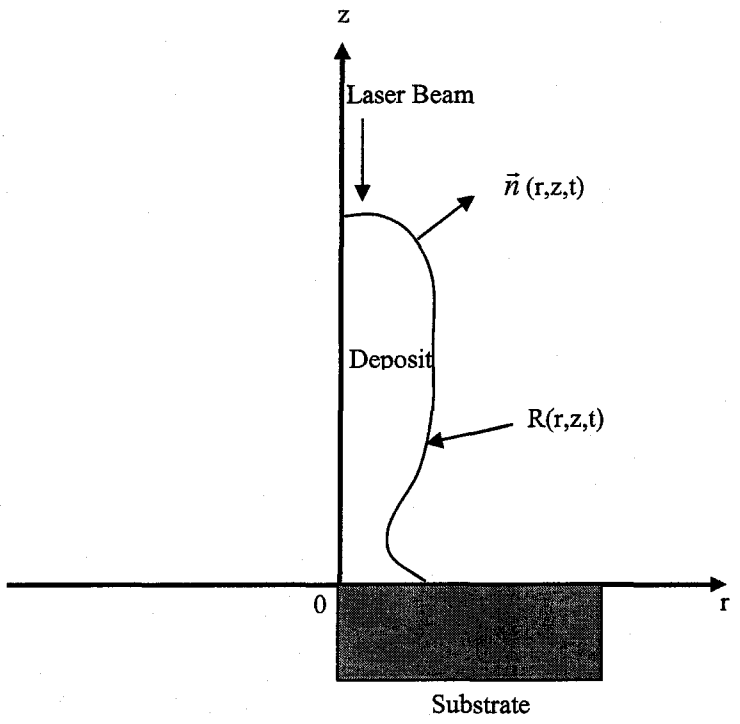

Figure 3.3 Axisymmetric Rod

The instantaneous surface of the deposit is defined by the vector function $R(z,r,t)$. The surface unit normal at each point is given by $\hat{n}(z,r,t)$, where z and r are the coordinates and t is time. If the radius of the surface r can be expressed as a single-valued function of z, i.e., $r(z)$, $R(z,r,t)$ can be expressed as $R(z,t)$. Then in this coordinate system, the instantaneous deposit surface and the unit normal vector at each point may be described by the vectors

$$R(z,r,t) = z(t)\cdot\hat{z} + r(z,t)\cdot\hat{r} \tag{3.25}$$

and

$$\hat{n}(z,t) = -\frac{1}{\psi}\cdot\left(\frac{dr(z,t)}{dz}\right)\cdot\hat{x} + \frac{1}{\psi}\cdot\hat{r} \tag{3.26}$$

in which, $\psi = \sqrt{1+\left(\frac{dr(z,t)}{dz}\right)^2}$.

3.3.2 Prediction of Deposit Temperature

To solve for the shape of an axisymmetric deposit, the temperature profile along the deposit length $T^d(z,t)$ must be known. From the governing equations given in the previous section, the temperature can be obtained. However, we may simplify the equations further using arguments given by [Maxwell 1996].

First, we assume that the heat flux into and out of the deposit is in equilibrium and the temperature distribution over the deposit is at steady state; second, the material properties are constants; and last, the temperature gradient is largely one-dimensional along the axial z coordinate.

Let γ be the deposit volume per unit surface area. The heat sources Q_{in} and sinks Q_{loss} are related to the heat fluxes Q''_{in} and Q''_{loss} by $Q = Q''/\gamma$. Given that the shape of the axisymmetric deposit is defined by $r(z)$, the heat conduction equation of deposit can be simplified to

$$k_D\frac{d}{dz}\left(\pi r^2(z)\frac{dT^D}{dz}\right) + 2\pi r(z)Q''_{in} - 2\pi r(x)Q''_{loss} = 0 \tag{3.27}$$

For a Gaussian beam absorbed completely at a rod tip, and simultaneous convection and radiation from the rod surface, Q''_{in} and Q''_{loss} may be expressed as

$$Q''_{in}(z,r) = 2P_0 \frac{\Lambda}{\pi\omega^2(z)} e^{-\frac{2r^2}{\omega^2(z)}} (\hat{z} \cdot \hat{n}(z)) \tag{3.28}$$

and

$$Q''_{loss}(z,r) = h_{conv}(T^D - T_\infty) + \sigma\varepsilon(T^D - T_\infty) \tag{3.29}$$

where P_0 is the laser intensity, $\omega(z)$ is the laser beam waist radius at any axial position relative to the rod tip, Λ is the absorption coefficient, the parameter σ is the Stefan-Boltzmann constant ε is the thermal emissivity, and T_∞ is the ambient temperature.

The laser input flux may be treated as the boundary condition at the rod tip. Assuming that heat conduction within the rod averages the spatial dependence of the input power, the boundary condition for a flat rod tip may be expressed as

$$\frac{dT^D}{dz} = \frac{1}{k_D \pi r^2} \left(\lambda P_0 - h_{conv}(T^D - T_\infty) \right), \tag{3.30}$$

where h_{cond} denotes the heat transfer coefficients on the surface of the substrate and

, for a constant beam radius ω, $\lambda = \frac{2\Lambda}{\pi\omega^2}$. Here, z is at the tip of the rod.

Conduction to the substrate at the base of the rod is represented by the boundary condition

$$\frac{dT^D}{dz} = \frac{1}{k_D \pi r^2} Q_{cond} \tag{3.31}$$

where z is at the base. The power passing into the substrate, Q_{cond}, generates an average temperature T^B at the interface between the rod and the substrate. A solution to the problem of a uniform heated circular disc on a semi-infinite solid has been derived by

Carslaw and Jaeger [Carslaw 1959]. The average base temperature of the heat flow though such a disc can be expressed as

$$T^B = \frac{8rQ_{cond}}{3\pi k_S} \tag{3.32}$$

So the boundary condition in Eq. (3.32) can be expressed as

$$\frac{dT^D}{dz} = \frac{3k_S T^D}{8k_D r^3} \tag{3.33}$$

3.3.3 Prediction of Rod Growth

Once the temperature is obtained, from Equation (3.27) rod growth can be calculated with the following equation

$$\Delta\vec{z}_n(z,r) = K_0 e^{-\frac{E_a}{RT^D}} \Delta t\left(-\frac{1}{\psi}\left(\frac{dr(z,t)}{dz}\right)\cdot\hat{x} + \frac{1}{\psi}\cdot\hat{r}\right) \tag{3.34}$$

in which, $\psi = \sqrt{1+\left(\frac{dr(z,t)}{dz}\right)^2}$.

3.3.4 Prediction of Substrate Temperature

To determine the initial surface of an axisymmetric rod, the heat conduction equation for the substrate must be solved. For a cylindrical domain, the steady state heat conduction equation can be simplified as

$$k_S \frac{1}{r}\frac{\partial}{\partial r}\left(r\frac{\partial T^S}{\partial r}\right) + k_S \frac{\partial^2 T^S}{\partial z^2} = 0 \tag{3.35}$$

For a stationary cylindrical substrate, boundary conditions can be specified as follows:

$$\frac{\partial T^S}{\partial z} = \frac{\lambda P_0 + h_{cond}(T^S - T_\infty)}{k_s} \qquad \text{at } z = 0, 0 \le r \le R_d \qquad (3.36a)$$

$$T^S = T_\infty \qquad \text{at } z = 0, R_d \le r \le R_s \qquad (3.36b)$$

$$T^S = T_\infty \qquad \text{at } z = -H_s \qquad (3.36c)$$

$$T^S = T_\infty \qquad \text{at } r = R_s \qquad (3.36d)$$

where T_∞ is the ambient temperature. R_S and H_S are the radius and height of the substrate, respectively. $\lambda = \frac{2\Lambda}{\pi\omega^2}$, where ω is the laser beam radius, and Λ the absorption coefficient.

Note the two kinds of boundary conditions at the surface $z = 0$ of the substrate. At the beginning, when there is no deposition, the laser beam hits directly on the surface of substrate. The boundary condition in the reaction zone at the surface $z = 0$ of the substrate is given by Equation (3.36a). When there is a deposit on the substrate and the laser beam hits on the tip of the deposit, the boundary condition in the reaction zone at the surface ($z = 0$) of the substrate is given by Equation (3.20).

CHAPTER 4

AN INTEGRATED 3D LCVD MODEL WITH KINETICALLY AND MASS TRANSPORT LIMITED PROCESS

In Chapter 3, we considered only kinetically limited growth of deposit, in which the deposit process is controlled by the laser-induced temperature distribution and the magnitude of growth at each point increased exponentially with increased temperature. When the surface temperature increases to a certain level, the deposit process passes into the diffusion regime in which the deposit rate depends on the precursor concentration. This necessitates the inclusion of mass transport limited deposition rates into our model to achieve more accurate prediction of deposit growth and control of the deposition process. In this chapter, we first derive the governing equations to describe the gas-phase mass transport, gas-phase temperature distribution, and reaction rate influenced by molar ratio of species, and then develop a model to predict the mass transport limited deposit growth with and without gas phase heating in a cylindrical coordinate system. Finally, we combine the kinetic limited and mass transport limited models to simulate the rod growth, considering both deposit and substrate.

4.1 A General Gas-Phase Mass Transport Limited Model

As described in Section 2.2.2, pyrolytic deposition operates through absorption of a precursor onto a substrate (or deposit) surface and subsequent thermal dissociation of the compound through heating of the solid surface. Laser-induced chemical vapor deposition depends on the chemical reactions happening in the reaction zone, as shown in Figure 2.2. To analyze how the chemical reaction affects the growth rate of deposition, the reaction kinetics of pyrolytic laser chemical processing must be investigated.

In most cases, precursors used in LCVD are of the form, $P = AB_\mu$, where A is a metal or element to be deposited, and B_μ are μ ligands which are loosely bound to B. Usually B is chosen such that it is not likely to remain as a by-product in the solid deposit, giving a pure deposit of A. The reaction of gas-phase molecules AB_μ shall be heterogeneous, i.e. it shall occur exclusively on the surface r_s. Here, species A condenses on the surface r_s and either forms the deposit or it reacts further, while atoms/molecules B immediately desorb from this surface.

$$AB_\mu \rightarrow \cdots \rightarrow A(\downarrow) + \mu \cdot B(\uparrow) \tag{4.1}$$

More details about the reaction kinetics in laser-induced pyrolytic chemical processing can be found in [Bäuerle 1986, 1990].

4.1.1 Gas-Phase Mass Transport in a Cartesian Coordinate System

A number of assumptions are made to simplify the analysis: the reaction in equation (4.1) is sufficiently slow so the pressure gradients within the gas-phase are negligible; the gas-phase volume is semi-infinite; heat losses by thermal radiation are disregarded; gas viscosity is ignored.

Based on the above assumptions, the equations of continuity for the individual specie in the stationary condition can be written as

$$\nabla J_i = 0 \tag{4.2}$$

where i represents species AB_μ or B, J_i is the total flux of specie i with respect to the stationary coordinates, and ∇ represents divergence.

For the species AB_μ this flux can be written [Kirichenko 1990] as

$$J_{AB} = -N \cdot D_{AB} \cdot \left(\nabla X_{AB} + k_T \cdot \nabla \ln T_G\right) + N_{AB} \cdot v \tag{4.3}$$

where N is the total particle density, D_{AB} the effective temperature dependent diffusion coefficient, k_T the thermal diffusion ratio, T_G the gas-phase temperature, N_{AB} the particle density of species AB_μ, v the average particle velocity of the gas, and X_{AB} the molar ratio of species AB_μ where X_{AB} is defined as

$$x_{AB} = \frac{N_{AB}}{N} \tag{4.4}$$

where N is the total particle density.

Equations (4.2) and (4.3) describe the distribution of the molar ratio X_{AB} in domain Ω. To investigate the gas-phase reaction kinetics, we need to define the boundaries of the domain Ω and specify the boundary conditions to solve Equations (4.2) and (4.3), obtain the molar ratio distribution X_{AB}, and hence determine the deposit growth rate. The domain Ω and the corresponding boundaries are shown in Figure 4.1.

We assumed that the gas-phase volume is semi-infinite. For convenience of calculation, we now assume that the gas-phase volume is large enough so that the boundary condition at the outer boundary $\partial\Omega_1$ can be given as

$$\left.\frac{\partial X_{AB}}{\partial \vec{n}}\right|_{\partial\Omega_1} = 0 \tag{4.5}$$

where $\vec{n}$ is the unit normal vector at the outer boundary.

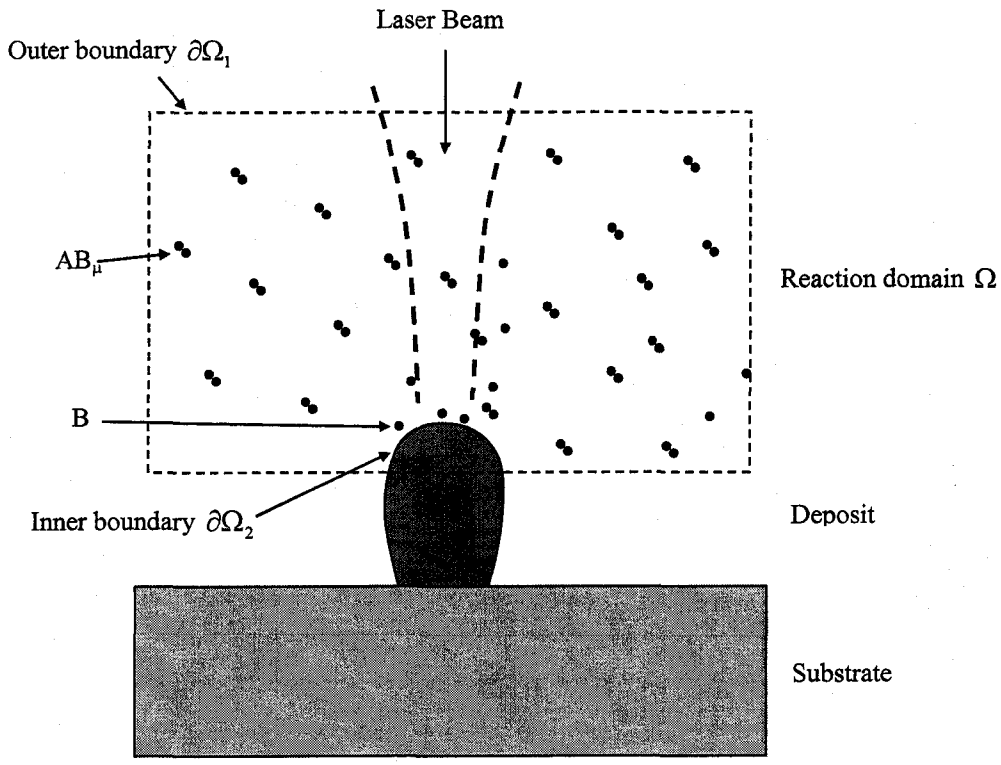

Figure 4.1 Reaction domain and boundaries

The inner boundary $\partial\Omega_2$ is the interface between gas and deposit (or substrate) on which the molecule A is deposited. Specifying the inner boundary condition is not straightforward because the molar ratio on this boundary results from the complex chemical reaction. On the inner boundary, the total flux of species shall be balanced by the reaction rate

$$(J_{AB})_{\Omega_2} = -K_{\Omega_2} \cdot (N_{AB})_{\Omega_2} = -K_{\Omega_2} \cdot N_{\Omega_2} \cdot (X_{AB})_{\Omega_2} \tag{4.6}$$

Here, K_{Ω_2} is the rate constant and is given by the Arrhenius law

$$K_{\Omega_2} = K_0 \cdot e^{-\frac{E_a}{k_B \cdot T_{\Omega_2}}}, \tag{4.7}$$

where ΔE is the apparent chemical activation energy, and k_B is the Boltzmann constant. The temperature on the inner boundary shall be uniform and is given by

$$T_{\Omega_2} = T_\infty + \Delta T_{\Omega_2}, \tag{4.8}$$

where T_∞ is the temperature far away from the reaction zone and ΔT_{Ω_2} the laser-induced temperature rise.

Applying equation (4.3) at the inner boundary gives

$$(J_{AB})_{\Omega_2} = -N_{\Omega_2} \cdot (D_{AB})_{\Omega_2} \cdot \left(\frac{\partial X_{AB}}{\partial \vec{n}}\bigg|_{\Omega_2} + k_T \cdot \frac{\partial \ln T}{\partial \vec{n}}\bigg|_{\Omega_2}\right) + (N_{AB})_{\Omega_2} \cdot v_{\Omega_2} \tag{4.9}$$

where

$$v_{\Omega_2} = \frac{1}{N_{\Omega_2}}[(J_{AB})_{\Omega_2} + (J_B)_{\Omega_2}] = (\mu - 1) K_{\Omega_2} \cdot (X_{AB})_{\Omega_2}, \tag{4.10}$$

$$N_{\Omega_2} = \frac{N(\infty) \cdot T(\infty)}{T_{\Omega_2}},$$

and

$$(D_{AB})_{\Omega_2} = D_{AB}(\infty) \cdot \left(\frac{T_{\Omega_2}}{T(\infty)}\right)^n, \qquad 1.5 \le n \le 2$$

Substituting equation (4.6) to equation (4.9), we have

$$-K_{\Omega_2}\cdot N_{\Omega_2}\cdot (X_{AB})_{\Omega_2} = -N_{\Omega_2}\cdot D_{\Omega_2}\cdot (\frac{\partial X_{AB}}{\partial \vec{n}}\Big|_{\Omega_2} + k_T\cdot \frac{\partial \ln T}{\partial \vec{n}}\Big|_{\Omega_2}) + N_{\Omega_2}\cdot (X_{AB})_{\Omega_2}\cdot v_{\Omega_2} \quad (4.11)$$

From equation (10), equation (4.11) can be rewritten as

$$(\mu-1)\cdot K_{\Omega_2}\cdot (X_{AB})_{\Omega_2}{}^2\cdot + K_{\Omega_2}\cdot (X_{AB})_{\Omega_2} - D_{\Omega_2}\cdot (\frac{\partial X_{AB}}{\partial \vec{n}}\Big|_{\Omega_2} + k_T\cdot \frac{\partial \ln T}{\partial \vec{n}}\Big|_{\Omega_2}) = 0 \quad (4.12)$$

Equation (4.12) specifies the boundary condition for calculating the molar ratio X_{AB} of species AB_μ at the inner boundary $\partial\Omega_2$.

4.1.2 Gas-Phase Heat Flow in a Cartesian Coordinate System

The temperature distribution in the gas-phase reaction domain is modeled as well in order to model the mass transport. The gas is heated by conduction of energy away from the hot area of deposit. The process is considered to be at steady state. Since there is no source term, the heat transport equation can be written as

$$\nabla(k_G\cdot \nabla T_G) = 0 \quad (4.13)$$

where T_G is the temperature in the gas-phase domain and k_G the thermal conductivity of the gas mixture.

The gas temperature is equal to the surface temperature T_S of the rod at the inner boundary $\partial\Omega_2$.

$$(T_G)_{\partial\Omega_2} = T_S . \quad (4.14)$$

The outer boundary condition for determining the temperature distribution within the reaction zone is

$$\frac{\partial T_G}{\partial \vec{n}}\Big|_{\partial\Omega_2} = 0 . \quad (4.15)$$

4.2 A Gas-Phase Mass Transport Limited Model for Rod Growth

A general gas-phase mass transport limited model and its boundary conditions have been presented in the previous section. Many factors regarding the governing equations may affect the temperature distribution and the growth rate. The complex interrelation among the heat flow between the deposit and substrate, the temperature field in the gas-phase and the solid phase, the mass transport, and the deposit growth makes it difficult to obtain an accurate solution. To simulate the deposit growth of an axisymmetric rod, we simplify the above governing equations and present a model in a cylindrical coordinate system in the following section. The gas-phase reaction domain in a cylindrical coordinate system is shown in Figure 4.2. The governing equations of the gas-phase mass transport for growing a rod are derived in Section 4.2.1, and heat transfer is derived in Section 4.2.2.

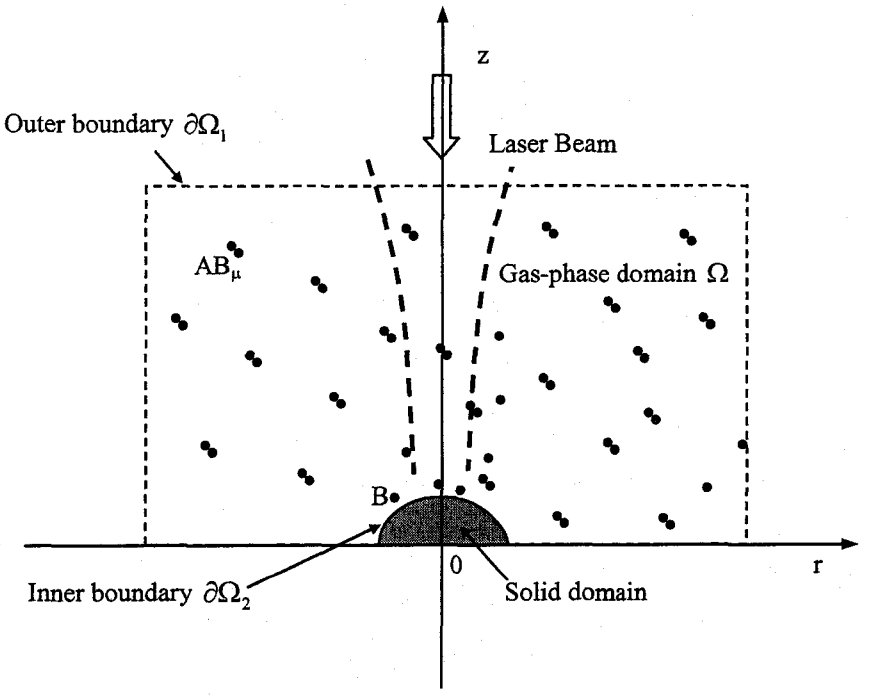

Figure 4.2 Gas-phase reaction domain in a cylindrical coordinate system

4.2.1 Gas-Phase Mass Transport in a Cylindrical Coordinate System

In a cylindrical system, the equation of continuity, equation (4.2), for the individual species i, where i is AB_μ or B, can be written as

$$\nabla J_i = \frac{1}{r}\left[\frac{\partial}{\partial r}(r\cdot(J_i)_r)+\frac{\partial}{\partial z}(r\cdot(J_i)_z)\right]=0. \tag{4.16}$$

For the species AB_μ, flux J_{AB} has the following expression in the cylindrical coordinate

$$\begin{aligned} J_{AB} &= -N\cdot D_{AB}\cdot[(\frac{\partial X_{AB}}{\partial r}+k_T\cdot\frac{\partial \ln T_G}{\partial r})+N_{AB}\cdot v_r]\cdot\vec{e}_r \\ &+[(\frac{\partial X_{AB}}{\partial z}+k_T\cdot\frac{\partial \ln T_G}{\partial z})+N_{AB}\cdot v_z]\cdot\vec{e}_z \end{aligned} \tag{4.17}$$

From

$$J_{AB}=(J_{AB})_r\cdot\vec{e}_r+(J_{AB})_z\cdot\vec{e}_z \tag{4.18}$$

and

$$N_{AB}=N\cdot X_{AB} \quad , \tag{4.19}$$

one can obtain the following equations

$$(J_{AB})_r=-N\cdot D_{AB}\cdot(\frac{\partial X_{AB}}{\partial r}+k_T\cdot\frac{\partial \ln T_G}{\partial r})+N\cdot X_{AB}\cdot v_r \tag{4.20}$$

$$(J_{AB})_z=-N\cdot D_{AB}\cdot(\frac{\partial X_{AB}}{\partial z}+k_T\cdot\frac{\partial \ln T_G}{\partial z})+N\cdot X_{AB}\cdot v_z \tag{4.21}$$

The average gas velocity is obtained as

$$v=\frac{1}{N}[J_{AB}+J_B]=\frac{\mu-1}{N}J_{AB}. \tag{4.22}$$

From equation (4.22), we have

$$N \cdot v_r = (1-\mu) \cdot (J_{AB})_r \tag{4.23}$$

$$N \cdot v_z = (1-\mu) \cdot (J_{AB})_z \tag{4.24}$$

From equations (4.20), (4.21), (4.23), and (4.24), we have

$$(J_{AB})_r = -N \cdot D_{AB} \cdot (\frac{\partial X_{AB}}{\partial r} + k_T \cdot \frac{\partial \ln T_G}{\partial r}) + (1-\mu) \cdot X_{AB} \cdot (J_{AB})_r \tag{4.25}$$

$$(J_{AB})_z = -N \cdot D_{AB} \cdot (\frac{\partial X_{AB}}{\partial z} + k_T \cdot \frac{\partial \ln T_G}{\partial z}) + (1-\mu) \cdot X_{AB} \cdot (J_{AB})_z \ . \tag{4.26}$$

Rewriting equations (4.25) and (4.26) gives

$$(J_{AB})_r = \frac{-N \cdot D_{AB} \cdot (\frac{\partial X_{AB}}{\partial r} + k_T \cdot \frac{\partial \ln T_G}{\partial r})}{1+(\mu-1) \cdot X_{AB}} \tag{4.27}$$

$$(J_{AB})_z = \frac{-N \cdot D_{AB} \cdot (\frac{\partial X_{AB}}{\partial z} + k_T \cdot \frac{\partial \ln T_G}{\partial z})}{1+(\mu-1) \cdot X_{AB}} \ . \tag{4.28}$$

In the cylindrical coordinate system, we can derive the following equation for molar ratio calculation from equations (4.16), (4.27) and (4.28).

$$\begin{aligned} &\frac{1}{r} \cdot \{\frac{\partial}{r} \cdot [r \cdot \frac{-N \cdot D_{AB} \cdot (\frac{\partial X_{AB}}{\partial r} + k_T \cdot \frac{\partial \ln T_G}{\partial r})}{1+(\mu-1) \cdot X_{AB}}] + \\ &\frac{\partial}{z} \cdot [r \cdot \frac{-N \cdot D_{AB} \cdot (\frac{\partial X_{AB}}{\partial z} + k_T \cdot \frac{\partial \ln T_G}{\partial z})}{1+(\mu-1) \cdot X_{AB}}]\} = 0 \end{aligned} \tag{4.29}$$

where

$N = \frac{N(\infty)}{T_G^*(X_{AB})}$, $T_G^*(X_{AB}) = \frac{T_G}{T(\infty)}$, $N(\infty)$, and $T(\infty)$ are constants.

k_T is the thermal diffusion ratio, $k_T = \alpha_T \cdot X_{AB} \cdot (1-X_{AB})$, α_T is a constant, and

$$D_{AB} \approx D_{AB}(\infty) \cdot T_G^{*n}(X_{AB}),\ T_G^{*n}(X_{AB}) = [\frac{T_G}{T(\infty)}]^n,\ \text{n} \cong 1.5 - 2.5.$$

The outer boundary conditions of molar ratio X_{AB} on the boundary $\partial\Omega_1$ are given as follows:

$$\frac{\partial X_{AB}}{\partial r} = 0\ , \tag{4.30}$$

$$\frac{\partial X_{AB}}{\partial z} = 0\ . \tag{4.31}$$

The inner boundary condition on the inner boundary $\partial\Omega_2$ is given by Equation (4.12).

Equations (4.29) and its boundary conditions specified in Equations (4.30), (4.31), and (4.16) form a closed system to predict the distribution of the molar ratio X_{AB} which, in turn, is used to correct the growth rate and to achieve more accurate control of rod growth. It is seen that the gas-phase temperature distribution must be obtained first in order to compute the molar ratio from Equation (4.29). The gas-phase heat transfer is described in Section 5.2.2.

4.2.2 Gas-Phase Heat Flow in a Cylindrical Coordinate System

As discussed in the previous section, the temperature distribution in the gas-phase needs to be calculated in order to calculate the molar ratio. For the cylindrical coordinate system, we assume that thermal conductivity does not vary with temperature. The heat transfer Equation (4.13) has the following expression

$$k_D \cdot \frac{1}{r} \cdot [\frac{\partial}{\partial r}(r \cdot \frac{\partial T_G}{\partial r}) + \frac{\partial}{\partial z}(r \cdot \frac{\partial T_G}{\partial z})] = 0 \tag{4.32}$$

The gas temperature at the inner boundary $\partial\Omega_2$ is equal to the surface temperature of the rod,

$$T_G = T_S \tag{4.33}$$

The outer boundary conditions of the temperature distribution calculation within the gas-phase reaction domain is

$$\frac{\partial T_G}{\partial r} = 0 \tag{4.34}$$

$$\frac{\partial T_G}{\partial z} = 0 \tag{4.35}$$

Equations (4.32) – (4.35) form a closed system for computing the temperature distribution in the gas-phase reaction domain which is used for calculating the molar ratio in Equation (4.29).

4.3 Integrated Rod Growth Model with Both Kinetically Limited and Mass Transport Limited Rates

In Chapter 3 a LCVD kinetically limited model has been proposed, in which the deposit growth was assumed to be kinetically determined with no gas diffusion limitation. However, growth rate can be either kinetically limited or mass transport limited, depending on the temperature. In Sections 4.1 and 4.2, the kinetics of the chemical reaction in the gas-phase has been investigated and the governing equations describing mass and heat transfers within the gas-phase reaction domain have been derived. To produce a microstructure with high resolution, a integrated model considering both kinetically limited and mass transport limited growth must be developed

for process control and optimization. In this section, we combine two models together to obtain a integrated model that describes laser-induced chemical vapor deposition (3D-LCVD). The complete model consists of (i) heat transfer in the deposit, substrate and gas-phase domain, (ii) mass transport in the gas-phase domain, (iii) growth rate depending on both laser-induced temperature and molar ratio. The shape of a 3D axisymmetric rod microstructure is predicted considering both kinetically limited and mass transport limited growth rates. The integrated model consists of eight components: Gaussian laser beam,

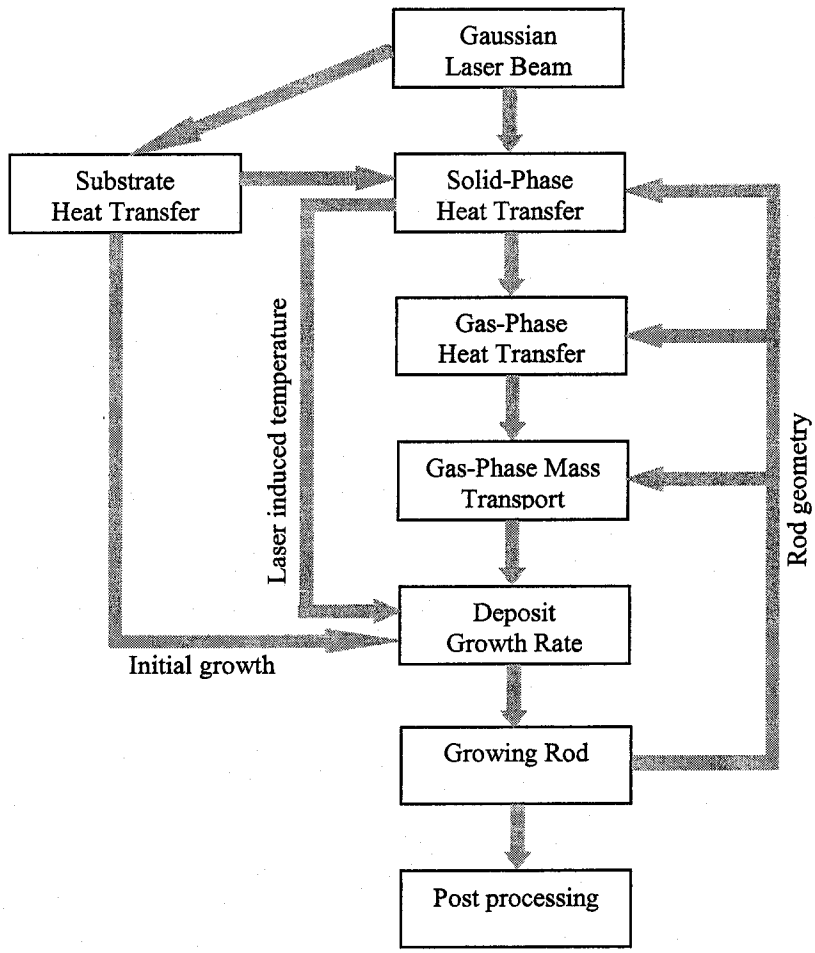

Figure 4.3 Components of the integrated LCVD model and their data flow (considering both kinetically limited and mass transport limited regions)

substrate heat transfer, solid-phase heat transfer, gas-phase heat transfer, gas-phase mass transport, deposit growth rate, growing rod, and post processing, as shown in the diagram of Figure 4.3.

At the initial stage, there is no deposit on the substrate, so a Gaussian laser beam is focused on the substrate directly. As the substrate absorbs heat, its temperature rises. If the temperature exceeds the threshold temperature, the deposit will be adsorbed onto the surface of the substrate. Deposit growth on the substrate provides the initial condition for subsequent rod growth. In the next stage, the laser beam is focused on the top of the deposit, instead of the substrate. The temperature distribution of the rod is predicted by the Solid-Phase Heat Transfer component. If the temperature on the surface of the rod is higher than a given value, the rod growth is no longer controlled by the kinetically limited region so the gas-phase reaction must be taken into account to update the growth rate on the surface of the rod. Hence, gas-phase heat transfer and gas-phase mass transport components are employed to predict the temperature distribution and molar ratio in the gas-phase reaction domain. The molar ratio and temperature on the surface of the rod are used to calculate the deposit growth rate by the deposit growth rate component. With the updated growth rate, the growing rod component can model the deposition on the surface of the rod and hence predict the shape of the rod in the next step. Based on the updated rod geometry and the Gaussian laser beam source, one can repeat the above process until the stop condition is satisfied. Finally, results such as temperature distribution, molar ratio, growth rate, and the rod geometry are analyzed. With this model, one may change the intensity of the Gaussian laser beam or use different deposit and substrate materials and compare the rod deposition processes. This approach

can provide an effective means to optimize the process by adjusting the different parameters.

For a brief review of the salient features of this modeling approach, we summarize the governing equations, boundary conditions, and description corresponding to each model component as follows.

(1) Gaussian Laser Beam

$$I(z,r) = 2P_0 \frac{\Lambda}{\pi\omega^2(z)} e^{-\frac{2r^2}{\omega^2(z)}} (\vec{z}\cdot\vec{n}) \tag{4.36}$$

where P_0 is the laser intensity, $\omega(z)$ the laser beam waist radius at any axial position relative to the rod tip, Λ the absorption coefficient, z and r the coordinates of the point of interest, $(\vec{z}\cdot\vec{n})$ the inner product of unit normal $\vec{n}$ and unit vector in the $\vec{z}$ direction.

(2) Substrate Heat Transfer

For a cylindrical domain, the steady state heat conduction equation can be simplified as

$$k_S \frac{1}{r}\frac{\partial}{\partial r}\left(r\frac{\partial T^S}{\partial r}\right) + k_S \frac{\partial^2 T^S}{\partial z^2} = 0, \tag{4.37}$$

where T^S is the temperature of the substrate at any point (z,r) in the cylindrical coordinate system, and k_S denotes the temperature-dependent thermal conductivity of the substrate. The boundary conditions are specified in equation (3.45).

(3) Solid-Phase Heat Transfer

$$k_D \frac{d}{dz}\left(\pi r^2(z)\frac{dT^D}{dz}\right) + 2\pi r(z)Q''_{in} - 2\pi r(x)Q''_{loss} = 0, \tag{4.38}$$

where T^D is the temperature of the substrate at any point (z,r) in the cylindrical

coordinate system, k_D denotes the temperature-dependent thermal conductivity of the deposit, $Q''_{in} = I(z,r)$ is defined in equation (4.36), and Q_{loss} is heat loss as defined in equation (3.38). The boundary conditions are specified in equation (3.45).

(4) Gas-Phase Heat Transfer

$$k_G \cdot \frac{1}{r} \cdot [\frac{\partial}{\partial r}(r \cdot \frac{\partial T_G}{\partial r}) + \frac{\partial}{\partial z}(r \cdot \frac{\partial T_G}{\partial z})] = 0, \tag{4.39}$$

where T_G is the temperature in the gas-phase domain and k_G the thermal conductivity of gas mixture. The boundary conditions are given by equations (4.33) – (4.35).

(5) Gas-Phase Mass Transport

$$\frac{1}{r} \cdot \{\frac{\partial}{r} \cdot [r \cdot \frac{-N \cdot D_{AB} \cdot (\frac{\partial X_{AB}}{\partial r} + k_G \cdot \frac{\partial \ln T_G}{\partial r})}{1 + (\mu - 1) \cdot X_{AB}}] + \frac{\partial}{z} \cdot [r \cdot \frac{-N \cdot D_{AB} \cdot (\frac{\partial X_{AB}}{\partial z} + k_G \cdot \frac{\partial \ln T_G}{\partial z})}{1 + (\mu - 1) \cdot X_{AB}}]\} = 0 \tag{4.40}$$

where X_{AB} is the molar ratio of species AB_μ, T_G the gas-phase temperature, N the total particle density, D_{AB} the effective temperature dependent diffusion coefficient, and

$N = \frac{N(\infty)T(\infty)}{T_G}$, $N(\infty)$ and $T(\infty)$ are constants, $k_T = \alpha_T \cdot X_{AB} \cdot (1 - X_{AB})$, α_T is constant,

$D_{AB} \approx D_{AB}(\infty) \cdot [\frac{T_G}{T(\infty)}]^n$, $n \cong 1.5 - 2.5$.

The outer and inner boundary conditions of the molar ratio X_{AB} are given by equations (4.30), (4.31) and (4.12).

(6) Deposit Growth Rate

When the reaction rate is limited by the activation energy and temperature, the process is termed kinetically limited. One can predict the deposit growth rate from the Arrhenius law, expressed as follows:

$$K = K_0 e^{-\frac{E_a}{RT_s}}, \tag{4.41}$$

where K_0 is a concentration-dependent rate constant that can be determined empirically, E_a and R are the activation energy and universal gas constant, respectively.

When the surface temperature increases to a certain level, the precursor and by-product diffusion control the growth rate. The process passes into the diffusion-limited region and the following expression is used for reaction rate calculation.

$$K = K_0 e^{-\frac{E_a}{RT_s}} \cdot p \cdot X_{AB} \tag{4.42}$$

where p is the total pressure, X_{AB} the molar ratio of species AB. Here, the total pressure is assumed constant in time and space for the gas-phase mass transport calculation.

(7) Growing a Rod

The geometry of the deposit will affect the growth in the actual LCVD process. For both kinetically limited and mass transport limited processes, growth of the deposit at each point on the surface of the rod is a normal vector that can be expressed as follows:

$$\Delta\vec{z}_n(z,r) = K \cdot \Delta t \cdot \hat{n}(z,t), \tag{4.43}$$

where $\Delta\vec{z}_n(z,r)$ is the local deposit growth at a point on the surface of the deposit, k the kinetically limited growth rate, Δt the time increment to obtain a deposit growth

$\Delta\vec{z}_n(z,r)$, and $\hat{n}(z,t)$ the unit outward normal vector on the instantaneous surface of deposition.

(8) Post Processing

The Post Process component of the model, calculates the normal unit vector at each point on the surface of the rod, determines the inner boundary of the gas-phase domain based on the shape of the rod, and analyzes the temperature distribution, molar ratio, and rod geometry. These steps will be discussed in details in the next chapter.

CHAPTER 5

NUMERICAL METHODS AND ALGORITHMS

Three-dimensional LCVD is a very complicated process. The surface temperature determines the reaction region and the growth rate of the deposit. Growth changes the shape of the deposit and the concentration of the precursor gas, which in turn affects the surface temperature of the deposit. This dual relationship between growth and temperature makes it difficult to solve the problem analytically. In general, for some simple physical problems with simple boundary conditions, analytic solutions can be obtained. However, for arbitrary structures and conditions, analytic solutions are not difficult to obtain, and the coupled equations for growth, gas diffusion and heat flow must be solved numerically in three dimensions. Usually, for each specific physical problem one should develop a simplified mathematical model and solve it using a numerical method. In this chapter, finite difference numerical methods are employed to discretize the coupled governing equations given in Chapter 4 and to develop computationally efficient algorithms to implement the model for simulating the process of fabricating a rod. In Section 5.1, a layer-by-layer numerical approach is presented to simulate the growth of an axisymmetric rod. In Section 5.2, a numerical method is given to simulate the temperature distribution of the rod. In Section 5.3, the finite difference method is proposed to discretize the governing equations of heat transfer in the substrate. Numerical

methods are developed to predict the temperature and the molar ratio distribution in the gas-phase reaction domain in Section 5.4 and Section 5.5, respectively. Section 5.6 discusses how to control the growth at each point on the surface of the rod.

5.1 A Layer-by-Layer Approach to an Axisymmetric Rod Growth

To simulate an axisymmetric rod growth based on the mathematical model described in Chapter 4, a numerical model needs to be developed. The rod can grow along the normal at a certain point on the surface. The growth along the normal can be divided into growths in the vertical and horizontal directions. Thus, we may partition the deposition process into a vertically growing process and a horizontally growing process. At time t, the deposit is decomposed into a number of layers, and each time it grows by an amount Δz in the z direction and Δr in the r direction. The new growth of the deposit depends on the current deposit shape and the temperature distribution on the surface induced by the laser beam. We assume that the temperature distribution in each layer to be the same so we do not have to discretize r. The mesh and layers of a rod are shown in Figure 5.1. This is the simple but effective layer-by-layer approach of modeling the growth of an axisymmetric rod [Dai 1999]. The shape of the rod is described by a sequence of discrete points (r_i, z_i), $i = 1,2,...,N$ on its surface. The grid points z_i in the z direction can be chosen according to the shape of the rod, $\Delta z_i = z_i - z_{i-1}$, with $z_1 = 0$ at the bottom and z_{N+1} at the tip of the rod. Near the tip and the bottom of the rod, the surface curvatures are large so the grid size Δz_i can be smaller. The smaller the specified grid size, the smoother is the rod shape.

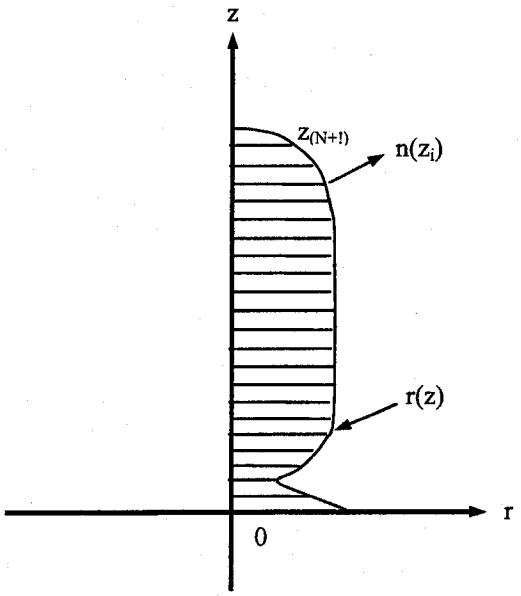

Figure 5.1 Mesh for the surface of an axisymmetric rod

5.2 Discretization of the Deposit Temperature Calculation

With the mesh shown in Figure 5.1, the heat conduction Equation (4.39) can be discretized as

$$-k_D \frac{r_{i-1/2}^2}{h^2} T_{i-1}^D + k_D \frac{r_{i-1/2}^2 + r_{i+1/2}^2}{h^2} T_i^D - k_D \frac{r_{i+1/2}^2}{h^2} T_{i+1}^D = S_i \qquad i = 2,...,N \qquad (5.1)$$

where S_i is the source term consisting of a Gaussian laser beam, convection term and radiation term, and $h = \Delta z_i$. Ignoring radiation term, we have

$$S_i = r_i \left[h_{conv} (T_i^D - T_\infty) - I(z_i, r_i) \right], \qquad (5.1)$$

where h_{conv} is the convection coefficient and $I(z_i, r_i)$ the heat source from the Laser beam,

$$I(z,r) = 2P_0 \frac{\Lambda}{\pi\omega^2(z)} e^{-\frac{2r_i^2}{\omega^2(z)}} \vec{n}(r_i, z_i) \tag{5.2}$$

The unit normal vector $\vec{n}(r_i, z_i)$ is discretized to give

$$\vec{n}(r_i, z_i) = -\frac{1}{\psi_i}\left(\frac{r_{i+1} - r_i}{2h}\right) \cdot \vec{z} + \frac{1}{\psi_i} \cdot \vec{r} \qquad \psi_i = \sqrt{1 + \left(\frac{r_{i+1} - r_i}{2h}\right)} \tag{5.3}$$

The boundary condition at the tip of the rod, given by Equations (3.39) can be discretized as

$$\frac{T_{N+1}^D}{h} = \frac{1}{k_D \pi r_{N+1}^2}\left(\lambda P_0 - h_{conv}(T_{N+1}^D - T_\infty)\right) \tag{5.4}$$

The boundary condition at the interface of the deposit and substrate, given by Equations (3.42) is discretized as

$$\frac{T_2^D - T_1^D}{h} = \frac{3k_S T_1^D}{8k_D r_1^3} \tag{5.5}$$

5.3 Discretization of Heat Transfer Equations in the Substrate

As previously discussed, the temperature distribution of the substrate must be obtained at the initial stage to specify the initial rod growth. Without an initial rod growth, the rod mesh described in Section 5.1 cannot be used. After the initial stage, the temperature calculation in the substrate may be also included in the entire modeling process, depending on heat transfer at the interface of the deposit and substrate. To numerically solve the heat transfer equations in the substrate, the cylindrical substrate domain should first be divided into a number of grids in the z and r directions. The mesh in the substrate is shown in Figure 5.2.

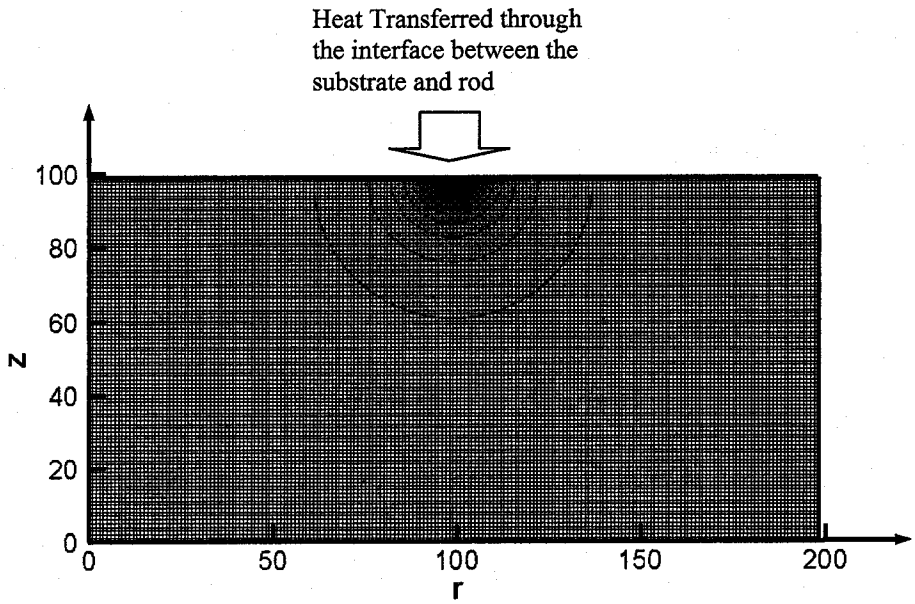

Figure 5.2. Substrate Mesh

The heat conduction equation for the substrate can be discretized, using a five-point finite difference scheme, as follows:

$$C_1\left(T^S\right)_{i,j-1} + C_2\left(T^S\right)_{i,j+1} + C_3\left(T^S\right)_{i-1,j} + C_3\left(T^S\right)_{i+1,j} - C_4\left(T^S\right)_{i,j} = 0 \tag{5.6}$$

where i and j are grid indices in the r and z directions, respectively,

$$\left(T^S\right)_{i,j} = T^S\left(z_i, r_j\right),$$

$$C_1 = \frac{r_{i,j} + r_{i,j-1}}{2r_{i,j}\left(r_{i,j} - r_{i,j-1}\right)^2},$$

$$C_2 = \frac{r_{i,j} + r_{i,j+1}}{2r_{i,j}\left(r_{i,j+1} - r_{i,j}\right)^2},$$

$$C_3 = \frac{1}{\left(z_{i,j} - z_{i-1,j}\right)^2}, \text{ and}$$

$$C_4 = C_1 + C_2 + 2C_3 .$$

The boundary conditions are discretized as follows:

$$\frac{\left(T^S\right)_{1,j} - \left(T^S\right)_{2,j}}{z_1 - z_2} = \frac{\lambda P_0 - h_{conv}\left[\left(T^S\right)_{1,j} - T_\infty\right]}{k_s} , \tag{5.7}$$

and

$$\frac{\left(T^S\right)_{i,2} - \left(T^S\right)_{i,1}}{r_2 - r_1} = 0 \tag{5.8}$$

$$\left(T^S\right)_{i,j} = T_\infty \tag{5.9}$$

By solving the above equations, the temperature distribution of the substrate can be obtained. The initial deposit on the substrate can be calculated as

$$h(r_j) = K_0 e^{-E_a / R\left(T^S\right)_{0,J}} , \tag{5.10}$$

where $h(r_j)$ is the deposit growth at grid point r_j in the r direction.

The deposit growth $h(r_j)$ is shown in Figure 5.3. To use the mesh described in Section 5.1 for modeling rod growths in subsequent steps, the deposit growth height $h(r_j)$ must be converted into a width distribution $r(z_i)$, where z_i is the deposit grid of the rod. This task can be accomplished using linear interpolation techniques.

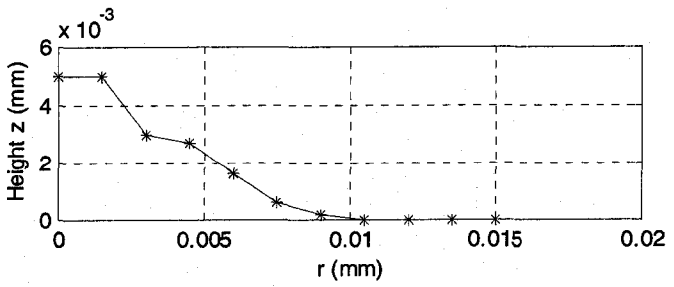

Figure 5.3 Initial growth

5.4 Discretization of the Gas-Phase Heat Transfer Equations

The r and z directions of the gas-phase reaction domain can be divided into M and N grids. For simplicity, we assume that the grid sizes are the same in *the* r and z directions, denoted by Δr and Δz, respectively. The mesh is given in Figure 5.4, where the shaded area is the solid domain. This shaded area is part of the rod not involved in the gas-phase computation. A finite difference method can be used to solve the gas-phase heat transfer equation and the differential equation.

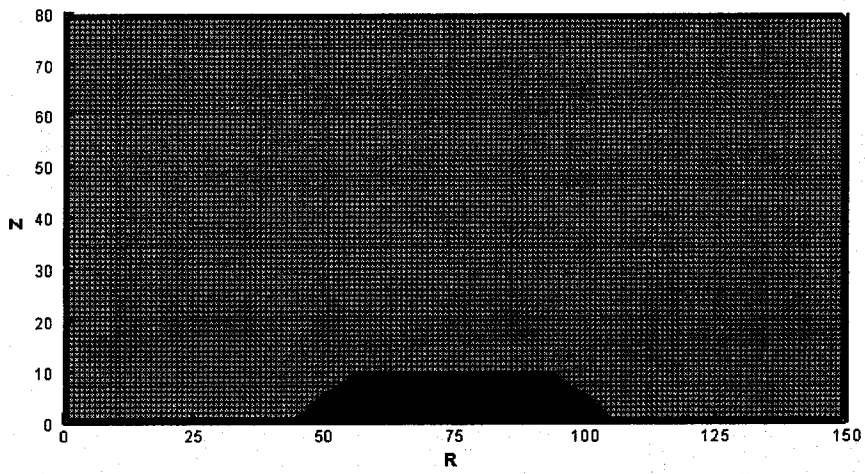

Figure 5.4. Mesh in the gas-phase reaction domain

Considering constant thermal conductivity of the gas mixture, from Equation (4.39), one can obtain the following equation

$$\frac{\partial}{\partial r}(r\cdot\frac{\partial T}{\partial r})+\frac{\partial}{\partial z}(r\cdot\frac{\partial T}{\partial z})=0. \tag{5.11}$$

Discretizing the above equation at grid point (i,j) gives

$$\frac{1}{\Delta r}\cdot[r_{i+1/2,j}\cdot(\frac{\partial T}{\partial r})_{i+1/2,j}-r_{i-1/2,j}\cdot(\frac{\partial T}{\partial r})_{i-1/2,j}]+$$

$$\frac{1}{\Delta z}\cdot[r_{i+1/2,j}\cdot(\frac{\partial T}{\partial z})_{i+1/2,j}-r_{i-1/2,j}\cdot(\frac{\partial T}{\partial z})_{i-1/2,j}]=0. \tag{5.12}$$

As such, we have

$$[\frac{r_{i,j}+r_{i+1,j}}{2}\cdot(\frac{\partial T}{\partial r})_{i+1/2,j}-\frac{r_{i-1,j}+r_{i,j}}{2}\cdot(\frac{\partial T}{\partial r})_{i-1/2,j}]+$$
$$\frac{\Delta r}{\Delta z}\cdot[\frac{r_{i,j}+r_{i,j+1}}{2}\cdot(\frac{\partial T}{\partial z})_{i,j+1/2}-\frac{r_{i,j-1}+r_{i,j}}{2}\cdot(\frac{\partial T}{\partial z})_{i,j-1/2}]=0. \tag{5.13}$$

Let

$$c_{14}=r_{i,j}+r_{i+1,j}$$

$$c_{15}=r_{i-1,j}+r_{i,j}$$

$$c_{16}=\frac{\Delta r}{\Delta z}\cdot(r_{i,j}+r_{i,j+1})$$

$$c_{17}=\frac{\Delta r}{\Delta z}\cdot(r_{i,j-1}+r_{i,j})$$

and

$$(\frac{\partial T}{\partial r})_{i+1/2,j}=\frac{T_{i+1}+T_i}{2\Delta r}$$

$$(\frac{\partial T}{\partial r})_{i-1/2,j}=\frac{T_{i-1}+T_i}{2\Delta r}$$

$$(\frac{\partial T}{\partial z})_{i,j+1/2}=\frac{T_{i,j+1}+T_{i,j}}{2\Delta z}$$

$$(\frac{\partial T}{\partial z})_{i,j-1/2}=\frac{T_{i,j-1}+T_{i,j}}{2\Delta z}.$$

Equation (5.13) is rewritten as

$$c_{14}\cdot\frac{T_{i+1,j}-T_{i,j}}{\Delta r}-c_{15}\cdot\frac{T_{i,j}-T_{i-1,j}}{\Delta r}+c_{16}\cdot\frac{T_{i,j+1}-T_{i,j}}{\Delta z}-c_{17}\cdot\frac{T_{i,j}-T_{i,j-1}}{\Delta z}=0. \tag{5.14}$$

Equation (5.14) gives

$$c_{18}T_{i-1,j} + c_{19}T_{i+1,j} + T_{i,j} + c_{20}T_{i,j+1} + c_{21}T_{i,j-1} = 0\ , \tag{5.15}$$

where

$$c_{18} = \frac{c_{15}}{c_{22}}$$

$$c_{19} = \frac{c_{14}}{c_{22}}$$

$$c_{20} = \frac{c_{16}}{c_{22}}\frac{\Delta r}{\Delta z}$$

$$c_{21} = \frac{c_{17}}{c_{22}}\frac{\Delta r}{\Delta z}$$

$$c_{22} = c_{14} - c_{15} + (c_{16} - c_{17})\frac{\Delta r}{\Delta z}$$

Equation (5.15) is the discrete equation for solving the temperature distribution in the gas-phase reaction domain.

The gas temperature at the inner boundary is equal to the surface temperature of the rod,

$$T_{i,0} = T_{s_{i,0}} \tag{5.16}$$

$$T_{0,j} = T_{s_{0,j}} \tag{5.17}$$

At the outer boundary, boundary conditions, Equations (4.33) and (4.34), are discretized to give

$$T_{0,j} = T_{1,j} \qquad j = 1,...,N-1 \tag{5.18a}$$

$$T_{M,j} = T_{M-1,j} \qquad j = 1,...,N-1 \tag{5.18b}$$

$$T_{i,0} = T_{i,1} \qquad i = 1, ..., M-1 \tag{5.18c}$$

$$T_{i,N} = T_{i,N-1} \quad i = 1,...,M-1 \tag{5.18d}$$

5.5 Discretization of the Gas-Phase Mass Transport Equations

The gas-phase mass transport equations describe the molar ratio distribution in the gas-phase domain. Equation (4.40) is dicretized in Section 5.5.1. The inner and outer boundary conditions are discretized in Sections 5.5.2 and 5.5.3, respectively. The inner boundary condition of the molar ratio is complex and cannot be specified explicitly but it can be solved implicitly.

5.5.1 Discrete Scheme of the Molar Ratio Equation

Equation (4.40) describes the molar ratio distribution in the gas-phase reaction domain and can be rewritten as

$$\frac{\partial}{\partial r}\{r\cdot[\frac{-\frac{N_\infty \cdot T_\infty}{T_G}\cdot D_{AB}\cdot[\frac{T_G}{T_\infty}]^n\cdot(\frac{\partial X_{AB}}{\partial r}+\alpha_T\cdot X_{AB}\cdot(1-X_{AB})\cdot\frac{\partial}{\partial r}\cdot\ln T_G)}{1+(\mu-1)\cdot X_{AB}}]\}$$

$$+\frac{\partial}{\partial z}\{r\cdot[\frac{-\frac{N_\infty \cdot T_\infty}{T_G}\cdot D_{AB}\cdot[\frac{T_G}{T_\infty}]^n\cdot(\frac{\partial X_{AB}}{\partial z}+\alpha_T\cdot X_{AB}\cdot(1-X_{AB})\cdot\frac{\partial}{\partial z}\cdot\ln T_G)}{1+(\mu-1)\cdot X_{AB}}]\}=0 \tag{5.19}$$

Distretizing Equation (5.19), and using X to denote X_{AB} and T to denote T_G for simplicity, we have

$$\frac{1}{\Delta r}\{r_{i+1/2,j}\cdot\frac{N_\infty\cdot T_\infty}{T_{i+1/2,j}}\cdot D_\infty\cdot(\frac{T_{i+1/2,j}}{T_\infty})^n\cdot[(\frac{\partial X}{\partial r})_{i+1/2,j}$$

$$+\alpha_T\cdot X_{i+1/2,j}\cdot(1-X_{i+1/2,j})\cdot(\frac{\partial \ln T}{\partial r})_{i+1/2,j}]$$

$$-r_{i-1/2,j}\cdot\frac{N_\infty\cdot T_\infty}{T_{i-1/2,j}}\cdot D_\infty\cdot(\frac{T_{i-1/2,j}}{T_\infty})^n\cdot[(\frac{\partial X}{\partial r})_{i-1/2,j}$$

$$+\alpha_T\cdot X_{i-1/2,j}\cdot(1-X_{i-1/2,j})\cdot(\frac{\partial \ln T}{\partial r})_{i-1/2,j}]\}$$

$$+\frac{1}{\Delta z}\{r_{i+1/2,j}\cdot\frac{N_\infty\cdot T_\infty}{T_{i+1/2,j}}\cdot D_\infty\cdot(\frac{T_{i+1/2,j}}{T_\infty})^n\cdot[(\frac{\partial X}{\partial z})_{i+1/2,j}$$

$$+\alpha_T\cdot X_{i+1/2,j}\cdot(1-X_{i+1/2,j})\cdot(\frac{\partial \ln T}{\partial z})_{i+1/2,j}]$$

$$-r_{i-1/2,j}\cdot\frac{N_\infty\cdot T_\infty}{T_{i-1/2,j}}\cdot D_\infty\cdot(\frac{T_{i-1/2,j}}{T_\infty})^n\cdot[(\frac{\partial X}{\partial z})_{i-1/2,j}$$

$$+\alpha_T\cdot X_{i-1/2,j}\cdot(1-X_{i-1/2,j})\cdot(\frac{\partial \ln T}{\partial z})_{i-1/2,j}]\}=0 \quad (5.20)$$

Since

$$X_{i+1/2,j}=\frac{X_{i,j}+X_{i+1,j}}{2}$$

$$X_{i-1/2,j}=\frac{X_{i-1,j}+X_{i,j}}{2}$$

$$X_{i,j+1/2}=\frac{X_{i,j}+X_{i,j+1}}{2}$$

$$X_{i,j-1/2}=\frac{X_{i,j-1}+X_{i,j}}{2}$$

$$T_{i+1/2,j}=\frac{T_{i,j}+T_{i+1,j}}{2}$$

$$T_{i-1/2,j}=\frac{T_{i-1,j}+T_{i,j}}{2}$$

$$T_{i,j+1/2}=\frac{T_{i,j}+T_{i,j+1}}{2}$$

$$T_{i,j-1/2} = \frac{T_{i,j-1} + T_{i,j}}{2}$$

$$r_{i+1/2,j} = \frac{r_{i,j} + r_{i+1,j}}{2}$$

$$r_{i-1/2,j} = \frac{r_{i-1,j} + r_{i,j}}{2}$$

$$r_{i,j+1/2} = \frac{r_{i,j} + r_{i,j+1}}{2}$$

$$r_{i,j-1/2} = \frac{r_{i,j-1} + r_{i,j}}{2}$$

$b=\mu-1$,

we have

$$c_1 \cdot [(\frac{\partial X}{\partial r})_{i+1/2,j} + c_5 \cdot (\frac{\partial \ln T}{\partial r})_{i+1/2,j}] - c_2 \cdot [(\frac{\partial X}{\partial r})_{i-1/2,j} + c_6 \cdot (\frac{\partial \ln T}{\partial r})_{i-1/2,j}]$$

$$+c_3 \cdot [(\frac{\partial X}{\partial r})_{i,j+1/2} + c_7 \cdot (\frac{\partial \ln T}{\partial r})_{i,j+1/2}] - c_4 \cdot [(\frac{\partial X}{\partial r})_{i,j-1/2} + c_8 \cdot (\frac{\partial \ln T}{\partial r})_{i,j-1/2}] = 0, \quad (5.21)$$

where

$$c_1 = \frac{N_\infty \cdot D_\infty \cdot (r_{i,j} + r_{i+1,j}) \cdot (T_{i,j} + T_{i+1,j})^n}{2^n \cdot b \cdot T_\infty^{n-1} \cdot (X_{i,j} + X_{i+1,j})},$$

$$c_2 = \frac{N_\infty \cdot D_\infty \cdot (r_{i-1,j} + r_{i,j}) \cdot (T_{i-1,j} + T_{i,j})^n}{2^n \cdot b \cdot T_\infty^{n-1} \cdot (X_{i-1,j} + X_{i,j})},$$

$$c_3 = \frac{N_\infty \cdot D_\infty \cdot (r_{i,j} + r_{i,j+1}) \cdot (T_{i,j} + T_{i,j+1})^n}{2^n \cdot b \cdot T_\infty^{n-1} \cdot (X_{i,j} + X_{i,j+1})} \cdot \frac{\Delta r}{\Delta z},$$

$$c_4 = \frac{N_\infty \cdot D_\infty \cdot (r_{i,j-1} + r_{i,j}) \cdot (T_{i,j-1} + T_{i,j})^n}{2^n \cdot b \cdot T_\infty^{n-1} \cdot (X_{i,j-1} + X_{i,j})} \cdot \frac{\Delta r}{\Delta z},$$

$$c_5 = \frac{\alpha_T \cdot [2(X_{i,j} + X_{i+1,j}) - (X_{i,j} + X_{i+1,j})^2]}{4 + 2b \cdot (X_{i,j} + X_{i+1,j})},$$

$$c_6 = \frac{\alpha_T \cdot [2(X_{i-1,j} + X_{i,j}) - (X_{i-1,j} + X_{i,j})^2]}{4 + 2b \cdot (X_{i-1,j} + X_{i,j})},$$

$$c_7 = \frac{\alpha_T \cdot [2(X_{i,j} + X_{i,j+1}) - (X_{i,j} + X_{i,j+1})^2]}{4 + 2b \cdot (X_{i,j} + X_{i,j+1})},$$

$$c_8 = \frac{\alpha_T \cdot [2(X_{i,j-1} + X_{i,j}) - (X_{i,j-1} + X_{i,j})^2]}{4 + 2b \cdot (X_{i,j-1} + X_{i,j})}.$$

From

$$(\frac{\partial X}{\partial r})_{i+1/2,j} = \frac{X_{i,j} + X_{i+1,j}}{\Delta r},$$

$$(\frac{\partial X}{\partial r})_{i-1/2,j} = \frac{X_{i-1,j} + X_{i,j}}{\Delta r},$$

$$(\frac{\partial X}{\partial r})_{i,j+1/2} = \frac{X_{i,j} + X_{i,j+1}}{\Delta r},$$

$$(\frac{\partial X}{\partial r})_{i,j-1/2} = \frac{X_{i,j-1} + X_{i,j}}{\Delta r},$$

and Equation (5.21), we obtain

$$(c_1 + c_2 + c_3 \cdot \frac{\Delta r}{\Delta z} + c_4 \cdot \frac{\Delta r}{\Delta z}) \cdot X_{i,j}$$

$$= c1 \cdot X_{i+1,j} + c_2 \cdot X_{i-1,j} + c_3 \frac{\Delta r}{\Delta z} \cdot X_{i,j+1} + c_4 \cdot \frac{\Delta r}{\Delta z} \cdot X_{i,j-1}$$

$$+ c_1 \cdot c_5 \cdot (\ln T_{i+1,j} - \ln T_{i,j}) - c_2 \cdot c_6 \cdot (\ln T_{i,j} - \ln T_{i-1,j})$$

$$+c_3 \cdot c_7 \cdot \frac{\Delta r}{\Delta z} \cdot (\ln T_{i,j+1} - \ln T_{i,j}) - c_4 \cdot c_8 \cdot \frac{\Delta r}{\Delta z} \cdot (\ln T_{i,j} - \ln T_{i,j-1}) . \tag{5.22}$$

Rewriting Equation (5.22) gives the following standard five-point finite difference scheme:

$$X_{i,j} = c_9 \cdot X_{i+1,j} + c_{10} \cdot X_{i-1,j} + c_{11} \cdot X_{i,j+1} + c_{12} \cdot X_{i,j-1} + c_{13}$$

$$i = 1, ..., M-1, j = 1, ..., N-1, \tag{5.23}$$

where

$$c_0 = c_1 + c_2 + (c_3 + c_4)\frac{\Delta r}{\Delta z},$$

$$c_9 = \frac{c_1}{c_0},$$

$$c_{10} = \frac{c_2}{c_0},$$

$$c_{11} = \frac{c_3}{c_0}\frac{\Delta r}{\Delta z},$$

$$c_{12} = \frac{c_4}{c_0}\frac{\Delta r}{\Delta z},$$

and

$$c_{13} = \frac{c_1 \cdot c_5 \cdot (\ln T_{i+1,j} - \ln T_{i,j}) - c_2 \cdot c_6 \cdot (\ln T_{i,j} - \ln T_{i-1,j})}{c_0}$$

$$+ \frac{c_3 \cdot c_7 \cdot \frac{\Delta r}{\Delta z} \cdot (\ln T_{i,j+1} - \ln T_{i,j}) - c_4 \cdot c_8 \cdot \frac{\Delta r}{\Delta z} \cdot (\ln T_{i,j} - \ln T_{i,j-1})}{c_0}.$$

Equation (5.23) and the corresponding boundary conditions described in the next section are applied to all grid points in the computational domain to form a linear system. The linear system can be solved using traditional iterative techniques, such as the Jacobi, Gauss-Seidel, or the Successive Over-Relaxation (SOR) method [Burden 1997].

5.5.2 Inner Boundary

Equation (4.12) specifies the inner boundary condition of the molar ratio calculation. With r_s denoting inner boundary and from $k_T = \alpha_T \cdot X_{AB} \cdot (1 - X_{AB})$, Equation (4.12) is rewritten as

$$(\mu - 1) \cdot K_{r_s} \cdot (X_{AB})_{r_s}^{\ 2} \cdot + K_{r_s} \cdot (X_{AB})_{r_s}$$

$$-D_{\Omega_2} \cdot \left(\frac{\partial X_{AB}}{\partial \vec{n}}\bigg|_{r_s} + \alpha_T \cdot X_{AB} \cdot (1 - X_{AB}) \cdot \frac{\partial \ln T}{\partial \vec{n}}\bigg|_{r_s}\right) = 0. \tag{5.23}$$

One can obtain the discrete equation on the z direction as

$$-\left(\frac{b \cdot K_{r_s} \cdot \Delta r}{D_{\Omega_2}} + \alpha_T \cdot \frac{\partial \ln T_{r_s}}{\partial r} \cdot \Delta r\right) \cdot X_{0,j}^2$$

$$+\left(-\frac{K_{r_s} \cdot \Delta r}{D_{\Omega_2}} - 1 + \alpha_T \cdot \frac{\partial \ln T_{r_s}}{\partial r} \cdot \Delta r\right) \cdot X_{0,j} + X_{1,j} = 0, \tag{5.24}$$

where K_{r_s} is the reaction rate, $X_{0,j}$ the molar ratio at the inner boundary r_s and $X_{1,j}$ the molar ratio at the grid point next to the boundary grid point within the gas-phase reaction domain. In an iterative algorithm, $X_{1,j}$ is known from the previous iteration and $X_{0,j}$ is the unknown in the current iteration. Thus, the boundary condition $X_{0,j}$ can be calculated from Equation (5.24).

Letting

$$\varepsilon_r = \frac{K_{r_s} \cdot \Delta r}{D_s} \text{ and}$$

$$\beta_r = \alpha_T \cdot \frac{\partial \ln T}{\partial r} \cdot \Delta r = \alpha_T \cdot \ln\left(\frac{T_{1,j}}{T_{0,j}}\right),$$

one has

$$(b \cdot \varepsilon_r + \beta_r) \cdot X_{0,j}^2 + (\varepsilon_r + 1 - \beta_r) \cdot X_{0,j} - X_{1,j} = 0. \tag{5.25}$$

Rewriting Equation (5.25) gives

$$A_r \cdot X_{0,j}^2 + B_r \cdot X_{0,j} + C_r = 0, \tag{5.26}$$

where

$$A_r = b \cdot \varepsilon_r + \beta_r,$$

$$B_r = 1 + \varepsilon_r - \beta_r,$$

and

$$C_r = -X_{1,j}.$$

The solution of Equation (5.26) can be easily obtained and is given as follows:

$$X_{0,j} = \frac{-B_r \pm \sqrt{B_r^2 - 4 \cdot A_r \cdot C_r}}{2 \cdot A_r}, \tag{5.27}$$

where $B_r^2 - 4 \cdot A_r \cdot C_r \geq 0$ and $X_{0,j} \geq 0$. Note that the molar ratio cannot be negative so its range should be $X \in [0,1]$.

Similarly, one can obtain the molar ratio X at the inner boundary in the r direction, which gives

$$X_{i,0} = \frac{-B_z \pm \sqrt{B_z^2 - 4 \cdot A_z \cdot C_z}}{2 \cdot A_z}, \tag{5.28}$$

where

$$B_z^2 - 4 \cdot A_z \cdot C_z \geq 0,$$

$$X_{i,0} \geq 0,$$

$$A_z = b \cdot \varepsilon_z + \beta_z,$$

$$B_z = 1 + \varepsilon_z - \beta_z,$$

$$C_z = -X_{i,1},$$

$$\varepsilon_z = \frac{K_{z_s} \cdot \Delta z}{D_s},$$

and

$$\beta_z = \alpha_T \cdot \frac{\partial \ln T}{\partial z} \cdot \Delta z = \alpha_T \cdot \ln(\frac{T_{i,1}}{T_{i,0}}).$$

Equations (5.27) and (5.28) specify the inner boundary conditions for computing the molar ratio in the gas-phase reaction domain, in which N_s and D_s are given in Equation (4.40), and K_{z_s} is the reaction rate.

5.5.3 Outer Boundary

From Equations (4.31) and (4.32), the discrete outer boundary conditions are given below

$$X_{0,j} = X_{1,j} \qquad j = 1,...,N-1, \tag{5.29a}$$

$$X_{M,j} = X_{M-1,j} \qquad j = 1,...,N-1, \tag{5.29b}$$

$$X_{i,0} = X_{i,1} \qquad i = 1, ..., M-1, \tag{5.29c}$$

and

$$X_{i,N} = X_{i,N-1} \qquad i = 1,...,M-1, \tag{5.29d}$$

where subscript 0 represent a boundary grid point and i an interior grid point next to the boundary grid point. Both i and j are indices in the r and z directions, depending on the indices of the boundary grid points.

If the outer boundary is far away from the reaction point (or zone) and there is no carry gas in the reaction, the following boundary condition can be applied.

$$X_{0,j} = 1 \qquad j = 1,...,N-1, \tag{5.30a}$$

$$X_{M,j} = 1 \qquad j = 1,...,N-1, \tag{5.30b}$$

$$X_{i,0} = 1 \qquad i = 1, ..., M-1, \tag{5.30c}$$

and

$$X_{i,N} = 1 \qquad i = 1,...,M-1. \tag{5.30d}$$

5.6 Discretization of the Rod Growth

We may calculate the new growth of the rod in a small time increment Δt once the temperature T_i^D is known. There are two cases here: (i) for those grid point whose temperature is lower than the given threshold temperature, Equations (4.41) and (4.43) are used for predict the kinetically limited local deposit growth; (ii) for those grid points whose the temperature is higher than the threshold temperature, Equations (4.42) and (4.43) are employed to calculate the mass transport limited deposit growth. Their discrete respective equations are given below.

For kinetically limited growth,

$$z_{N+1} \leftarrow z_{N+1} + K_0 e^{-E_a / R(T^D)_{N+1}} \Delta t \tag{5.31a}$$

$$r_{N+1} = r_{N+1} \tag{5.31b}$$

$$z_1 \leftarrow z_1 + K_0 e^{-E_a / R(T^D)_1} \Delta t \tag{5.32a}$$

$$r_1 = r_1 \tag{5.32b}$$

$$z_i \leftarrow z_i + K_0 e^{-E_a / R(T^D)_i} \Delta t \frac{1}{\psi_i} \left(\frac{r_{i+1} - r_{i-1}}{2h} \right) \qquad i = 2,\ldots\ldots,N \qquad (5.33a)$$

$$r_i \leftarrow r_i + K_0 e^{-E_a / R(T^D)_i} \Delta t \frac{1}{\psi_i} \qquad i = 2,\ldots\ldots,N \qquad (5.33b)$$

Here, in each step we ignore the time it takes to reach the steady temperature. This assumption is based on the fact that the system reaches the steady state quickly [Maxwell 1996].

For mass transport limited growth,

$$z_i \leftarrow z_i + K_0 e^{-E_a / R(T^D)_i} PX \Delta t \frac{1}{\psi_i} \left(\frac{r_{i+1} - r_{i-1}}{2h} \right) \qquad i = 2,\ldots\ldots,N \qquad (5.34a)$$

$$r_i \leftarrow r_i + K_0 e^{-E_a / R(T^D)_i} PX \Delta t \frac{1}{\psi_i} \qquad i = 2,\ldots\ldots,N \qquad (5.34b)$$

$$z_{N+1} \leftarrow z_{N+1} + K_0 e^{-E_a / R(T^D)_{N+1}} PX \Delta t \qquad (5.35a)$$

$$r_{N+1} = r_{N+1} \qquad (5.35b)$$

where P is the pressure, X the molar ratio calculated in Section 5.5. ψ_i is defined in Section 3.3.3.

Usually, mass transport limited growth occurs at the top of the rod on which the laser beam is focused. For the lower part of the rod, the temperature is in the range where kinetically limited growth occurs.

5.7 Implementation of Numerical Methods and Algorithms

The numerical methods and sequential algorithms are implemented using Visual C++ with approximately 3000 lines of code. The structure of the program is determined by each component given in Figure 4.3 and its data flow. The computation in the gas-phase domain is to predict the molar ratio and to update the growth rate. As such, it is encapsulated in a C++ class *RodGas*. The molar ratio, solid domain and mesh size are data in the class. Several methods (or functions) are written to calculate the temperature distribution and the molar ratio and save the results to a file for post-processing. In the main program, a *RodGas* object is created through which the corresponding methods are called to pass the parameters, perform the gas-phase computation, and obtain the updated growth rate. A flag variable in the main program controls whether the integrated model or the kinetic model is used to perform computations.

The code is executed on a PC (Pentium 4 processor, 1.0G RAM) with Windows XP. It takes less than 2 minutes to run the kinetic model and less than 20 minutes to run the integrated model with 100 iterations. The code can also be executed on other operating systems such as Unix and Linux. The corresponding parallel computing algorithms and implementation are given in Chapter 6. With a user interface, this implementation may be extended and developed into a software package to model both the kinetically limited and mass-transport limited rod growth.

CHAPTER 6

PARALLEL ALGORITHMS AND IMPLEMENTATION

The strategy behind parallel computing is that a given problem is partitioned into multiple independent tasks with appropriate grain size, and these tasks are scheduled over multiprocessors for execution to achieve high performance. Parallel computing has made a tremendous impact on a variety of areas ranging from computational simulations for scientific and engineering applications to commercial applications in data mining and transaction processing. However, most application developers and users have witnessed and experienced both the promise and the pain of the implementation of high performance. First, most application developers and users focus on the application domains and may not have expertise in networking and underlying high performance computing (HPC) technologies, so the implementation is time and effort intensive, and the application is error-prone or has low throughput. Many software or middleware tools have been developed to facilitate the application development using HPC technology, but these tools are usually application-dependent and may not be used for other scientific applications. Generally, the performance of a parallel computing application depends on many aspects such as application partition method, parallel algorithm design, platforms, network connection, development environment and implementation. A full coverage of

these topics is beyond the scope of this study. Instead, we focus our study on application domain, parallel algorithm design, and implementation.

The integrated model proposed in Chapters 3, 4, and 5 has been implemented sequentially. The serial computational results show that computations in the substrate and the gas-phase domains, such as the heat and mass transfers, are the most computationally intensive parts in the entire integrated model. The computations in these two domains may be performed in parallel to improve the performance. With the similar governing equations and numerical schemes, the parallel computations in these two domains are also similar. For simplicity, only the parallel computation in the substrate is used as an example to describe the domain partitioning technique, parallel algorithm design and implementation, as given in Sections 6.1, 6.2 and 6.3. The development environment and performance analysis are presented in Section 6.4 and 6.5, respectively.

6.1 Domain Decomposition

To develop a parallel computing application, the researchers must partition a given problem into a number of tasks, and these tasks are assigned to multiple processors for executions. Decomposition method determines how to design parallel algorithms and how to map the tasks onto the multiple processing elements efficiently. One powerful and widely used decomposition method is data decomposition which consists of two steps. In the first step, the data on which the computations are performed is partitioned, and in the second step, the data partitioning is used to induce a partitioning of the computations into tasks [Grama 2003]. The operations that these tasks perform on different data partitions are usually similar and the corresponding parallel algorithms are relatively easy to implement. In the integrated model, the temperature distribution of the substrate must be

simulated first to predict the initial rod growth on the surface of the substrate. The substrate is decomposed into a mesh with m rows and n columns, as shown Figure 6.1.

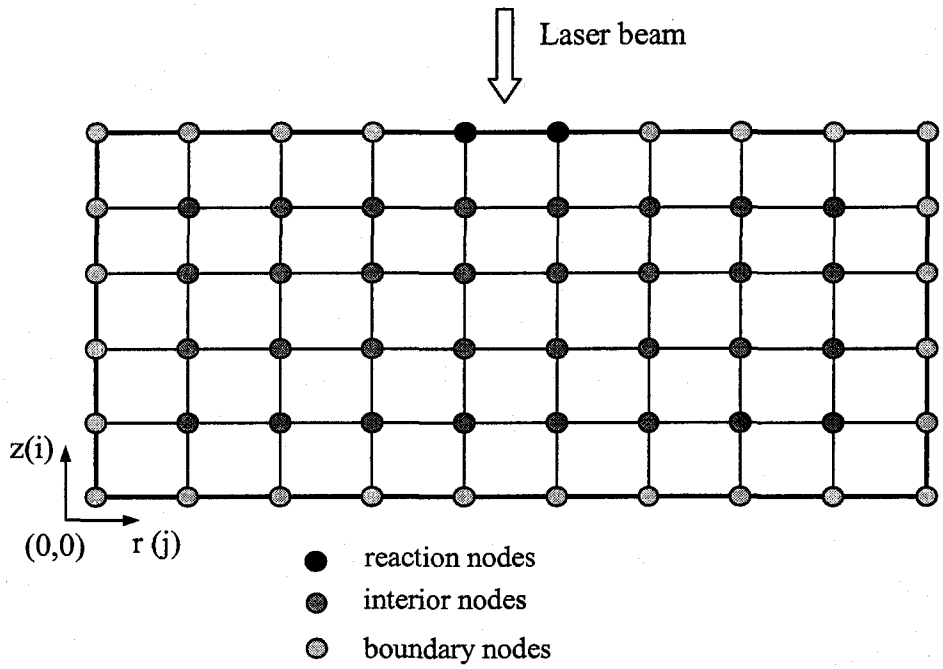

Figure 6.1 Mesh of the substrate

The heat transfer equations and its finite difference scheme are given in Eqs. (4.37) and (5.6), respectively. From Eq. (5.6), a linear system can be obtained and rewritten as a matrix-vector format, as shown in Eq. (6.1).

$$Ax = b \tag{6.1}$$

where A is the coefficient matrix, x the temperature vector, and b the vector consisting of boundary conditions. A direct method, e.g., parallel Gaussian elimination method, can be used to solve the linear system. However, for a two dimensional problem with mesh of m rows and n columns, the matrix A is a large sparse matrix with a size of $m \times n$ and its parallel implementation is expensive. Thus, iterative methods are chosen to predict the temperature distribution in the substrate.

The Eq. (5.6) can be solved iteratively using Jacobi's method [Freeman 1992]. For convenience of notation, we use T to denote T^S. After making an initial guess of temperature distribution, T^0, the method generates a sequence of approximations $T^{(k)}, k = 1,2,3,\ldots$, to the solution. The approximation, $T^{(k+1)}$, at the $(k+1)$ iteration is computed using the results $T^{(k)}$ obtained in the kth iteration:

$$T_{i,j}^{(k+1)} = (C_1 T_{i,j-1}^{(k)} + C_2 T_{i,j+1}^{(k)} + C_3 T_{i-1,j}^{(k)} + C_3 T_{i+1,j}^{(k)}) / C_4 \tag{6.2}$$

where C_1, C_2, C_3, and C_4 are defined in Eq. (5.6). The convergence condition is determined by

$$\left\| T^{(k+1)} - T^{(k)} \right\|_2 \le \varepsilon \tag{6.3}$$

where ε is a given tolerance, e.g. 10^{-4}. Eq. (6.2) shows that $T_{i,j}^{(k+1)}$ at node (i,j) relies on the values of the four neighboring nodes $(i-1,j)$, $(i+1,j)$, $(i,j-1)$ and $(i,j+1)$ obtained at the previous iteration k, as shown in Figure 6.2.

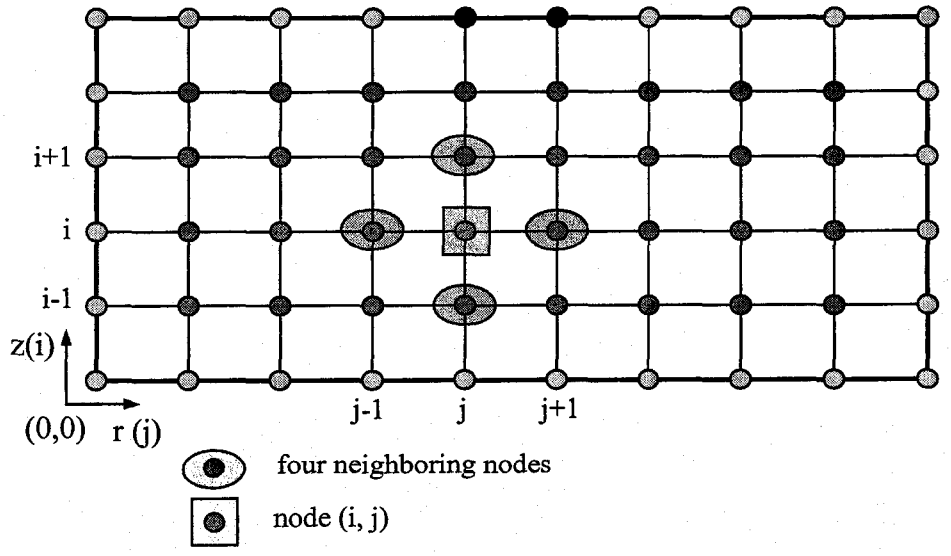

Figure 6.2 Jacobi's method for computing temperature distribution

Since the Jacobi's method is applied for all nodes in the domain, an intuitive way to implement it in parallel is to divide the nodes into a number of subsets and each process performs the computation on one subset of nodes. This approach results in a domain decomposition. A rectangular computational domain can be partitioned into a number of subdomains using either row block partition or checkerboard partition, as illustrated in Figure 6.3 with four processes.

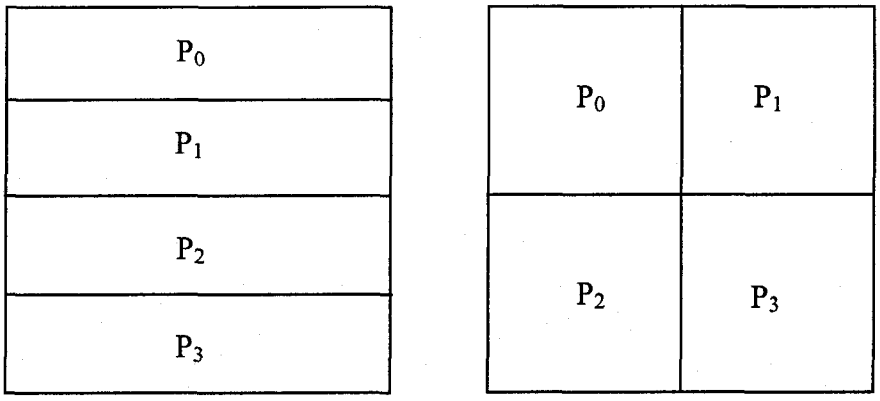

(a) row block partition (b) checkerboard partition

Figure 6.3 Row block partition and checkerboard partition

In the checkerboard partition, each process needs to communicate with several adjacent processes and leads to more communication cost. In the row block partition, each process communicates with at most two processes and the communication pattern is simple as we will see in the next section. Thus, a row block domain decomposition method is employed in this study. Without loss of generality, the n rows of the mesh are divided evenly into p consecutive blocks, where p is the number of processes used. The entire computation of the substrate is partitioned into p tasks, each of which is assigned onto one process for execution, as illustrated in Figure 6.4 with three processes. There are a total of mn/p nodes in each subdomain. The two adjacent processes must exchange the

data of their local boundary nodes. Since the temperature distribution can be represented by a $m \times n$ dense matrix T, the above physical domain decomposition is equivalent to the virtual row block partition of the matrix T. Each entry $T_{i,j}$ is computed using Eq. (6.2), which is described in the next section in detail.

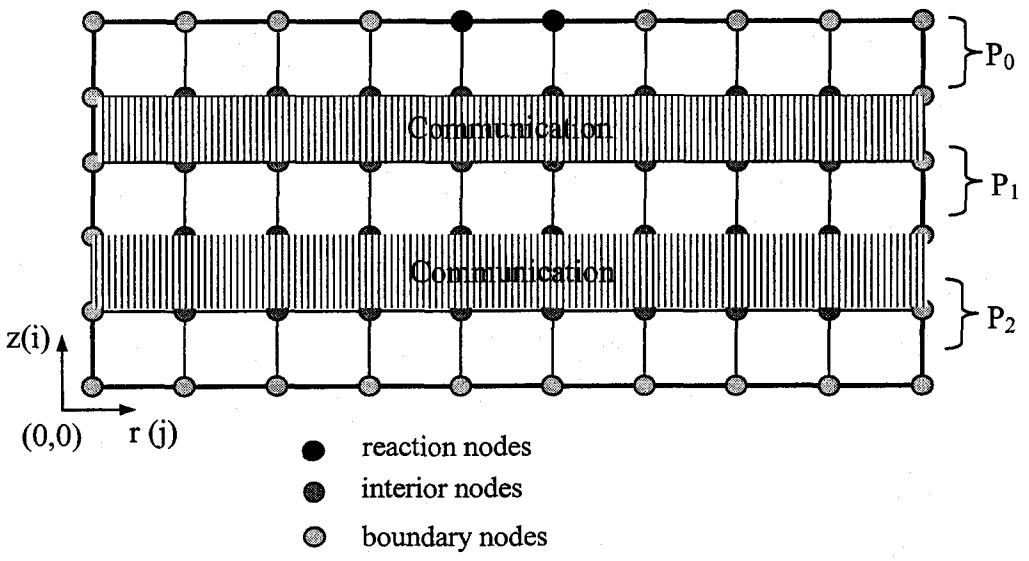

Figure 6.4 Row block decomposition of the substrate

6.2 Parallel Jacobi's Method

To design an efficient parallel algorithm, we need to consider not only the computation cost, but also the memory space of the platform. For a distributed memory platform, the global matrix T is scattered onto multiple processes and each process only stores data that belongs to its corresponding block. We make an assumption that there are p processes and the n rows of the matrix T are divided evenly into p row blocks. Each block consists of n/p rows and m columns of nodes. For each block, we define the local temperature matrix *T_local*, local row number *n_local* and local column number *m_local*, where *n_local* = n/p and *m_local* = m. This implementation requires less memory for

each process. The communication between two adjacent processes is illustrated by Figure 6.5. In the iterative Jacobi's method, the computation of *Tnew* at node *(i,j)* performed by process P_q requires values *Told* at four nodes *(i,j-1)*, *(i,j+1)*, *(i-1,j)* and *(i-1,j)*. However, *Told(i-1,j)* is not available on process P_q. The process P_{q+1} must send its local data *Told(i-1,j)* to the process P_q. Similarly, the process P_{q+1} must receive the local data *Told(i,j)* from P_q to compute *Tnew(i-1,j)*.

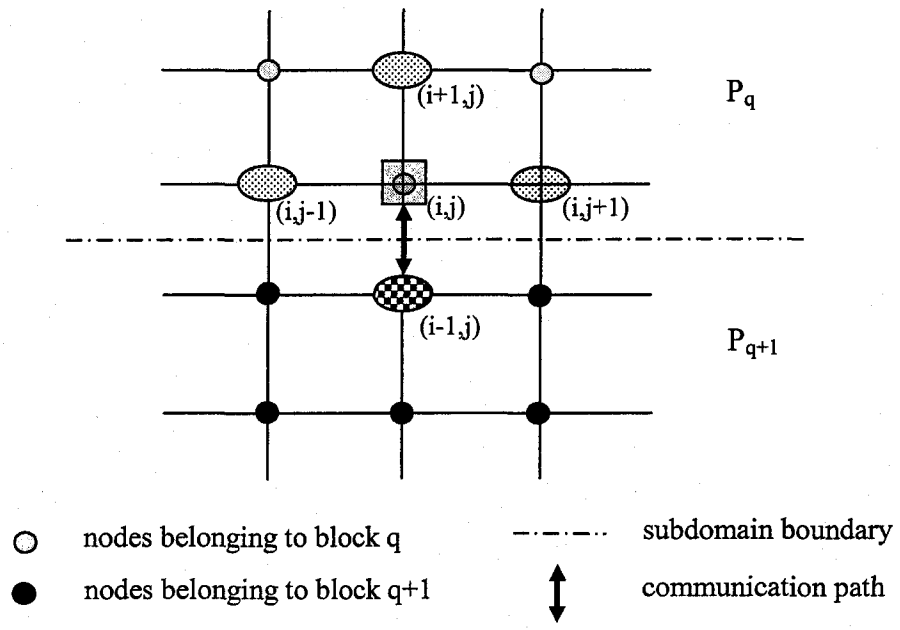

Figure 6.5 Communication between two adjacent processes

Based on the row block domain decomposition and the communication pattern, the C++ style pseudocode of the parallel Jacobi's method for process q on distributed memory platforms is given in Figure 6.6.

Algorithm 1: Parallel Jacobi's algorithm for distributed memory platforms

Scatter the initial guess of Tnew onto all processes and each stores Tnew_local

Process q:

```
convergent = false
do {
    for each node (i, j) located in block q {
        for each local interior nodes of block q
            Tnew_local[i,j] = (C1*Told_local[i,j-1]+ C2*Told_local[i,j+1]+
            C3*Told_local[i-1,j]+ C3*Told_local[i+1,j])/ C4    // Eq. (6.2)
        for each global interior node located in the block q
            compute the Tnew_local[i,j]
                //based on exchanged local boundary values
        for each global boundary node located in the block q
            compute Tnew_local[i,j] according to the boundary condition
        send its local boundary data to adjacent processes
        receive the local boundary data from adjacent processes
        swap Tnew_local and Told_local
        if convergent {
            convergent = true
        }
    } // end for
} while (k < maximum_iteration and not_convergent)
send local results to the master process
```

Figure 6.6 Parallel algorithm of Jacobi's method for distributed memory platforms

For a shared memory platform, we may broadcast the global matrix T and other parameters to all processes. At each iteration, each process performs the computation task corresponding to its own block and obtains the local matrix *Tnew_local*. The local matrices on all processes can be gathered efficiently and stored on the global matrix *Tnew* which is available for all processes. At the next iteration, *Tnew* and *Told* are swapped. The same procedure is repeated until the convergent condition is satisfied. At the end of the procedure, the results of *Tnew_local* on all processes are gathered for computing the

initial growth. This approach simplifies the communications among the processes and can be implemented using the functions provided by the parallel computing package such as MPI, as introduced in Section 6.4. The C++ style pseudocode of the parallel Jacobi's method for process q on a shared memory platform is given in Figure 6.7.

Algorithm 2: Parallel Jacobi's algorithm for shared memory platforms

```
Scatter the initial guess of Tnew onto all processes and each stores Tnew_local
Process q:
convergent = false
do {
    for each node (i, j) located in block q {
        for each local interior nodes of block q
            Tnew_local[i,j] = (C1*Told[i,j-1]+ C2*Told[i,j+1]+ C3*Told[i-1,j]+
            C3*Told[i+1,j])/ C4    // Eq. (6.2)
        for each global interior node located in the block q
            compute the Tnew_local[i,j] based on global matrix Told
        for each global boundary node located in the block q
            compute the Tnew_local[i,j] according to the boundary condition
        gather Tnew_local data from all processes and store them to Tnew
        swap Tnew and Told
        if convergent {
            convergent = true
        }
    } // end for
} while (k < maximum_iteration and NOT convergent)
gather local results from all processes and store them to global matrix Tnew
```

Figure 6.7 Parallel algorithm of Jacobi's method for shared memory platforms

Algorithm 2 differs from Algorithm 1, in terms of memory, computation and communication, in that: (1) in Algorithm 2, each process has global matrices *Tnew* and *Told* while, in Algorithm 1, each process only compute local matrices *Tnew_local* and *Told_local* which need less memory; (2) Algorithm 2 computes *Tnew_local* using the

global matrix *Told* while Algorithm 1 computes *Tnew_local* using the local matrix *Told_local*; and (3) in Algorithm 2, *Tnew_local* data from all processes are gathered and broadcast to all processes while, in Algorithm 1, only the local boundary data is sent to or received from the adjacent processes.

6.3 Parallel Gauss-Seidel and SOR Methods

The parallel Jacobi's method described in Section 6.2 is relatively easy to implement, but its convergence rate is too slow. This situation can be improved by using Gauss-Seidel (GS) method or successive overrelaxation (SOR) method. For any $\omega \neq 0$, Eq. (5.6) can be rewritten as

$$T_{i,j} = T_{i,j} + \frac{\omega}{C_4}(C_1 T_{i,j-1} + C_2 T_{i,j+1} + C_3 T_{i-1,j} + C_3 T_{i+1,j} - 4T_{i,j}) \tag{6.4}$$

If we update the $T_{i,j}$ according to increasing values of subscripts i and j, Eq. (6.4) suggests the iterative scheme

$$T_{i,j}^{(k+1)} = T_{i,j}^{(k)} + \frac{\omega}{C_4}(C_1 T_{i,j-1}^{(k+1)} + C_2 T_{i,j+1}^{(k)} + C_3 T_{i-1,j}^{(k+1)} + C_3 T_{i+1,j}^{(k)} - 4T_{i,j}^{(k)}) \tag{6.5}$$

in which most recently computed values $T_{i-1,j}^{(k+1)}$ and $T_{i,j-1}^{(k+1)}$ are used as soon as they are available. The optimal value of ω lies in (0, 2). The choice of $\omega = 1$ corresponds to the Gauss-Seidel iteration.

Eq. (6.5) can be implemented in parallel using the red-black ordering technique. The node (i,j) is denoted red or black according to whether $i+j$ is odd or even. If $i+j$ is odd, the node (i, j) is marked red and if $i+j$ is even, the node (i, j) is marked black. The

red-black ordering is illustrated in Figure 6.8. The evaluation of each $T_{i,j}^{(k+1)}$ corresponding to red nodes involves the values of black nodes only, and vice versa.

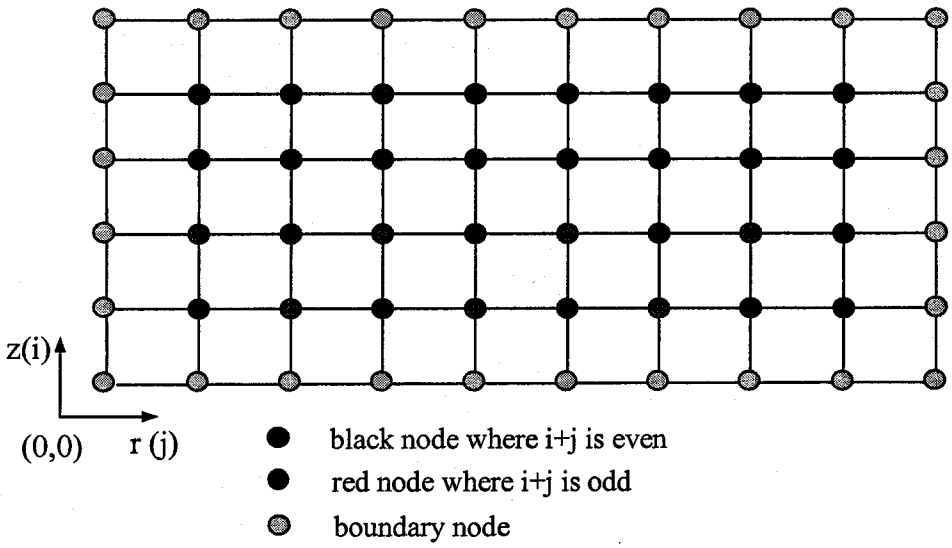

Figure 6.8 Red-black ordering technique

Based on the red-black ordering technique, the approximation $T_{i,j}^{(k+1)}$ can be updated in a different order suggested by Eq. (6.5). Each iteration of this method consists of two phases: (1) updating all the red values first and then (2) updating all the black values. The two phases are illustrated by Figure 6.9 and Figure 6.10, respectively.

For red nodes where $i+j$ is odd, we have

$$T_{i,j}^{(k+1)} = T_{i,j}^{(k)} + \frac{\omega}{C_4}(C_1 T_{i,j-1}^{(k)} + C_2 T_{i,j+1}^{(k)} + C_3 T_{i-1,j}^{(k)} + C_3 T_{i+1,j}^{(k)} - 4T_{i,j}^{(k)}) \tag{6.6}$$

For black nodes where $i+j$ is even,

$$T_{i,j}^{(k+1)} = T_{i,j}^{(k)} + \frac{\omega}{C_4}(C_1 T_{i,j-1}^{(k+1)} + C_2 T_{i,j+1}^{(k+1)} + C_3 T_{i-1,j}^{(k+1)} + C_3 T_{i+1,j}^{(k+1)} - 4T_{i,j}^{(k)}) \tag{6.7}$$

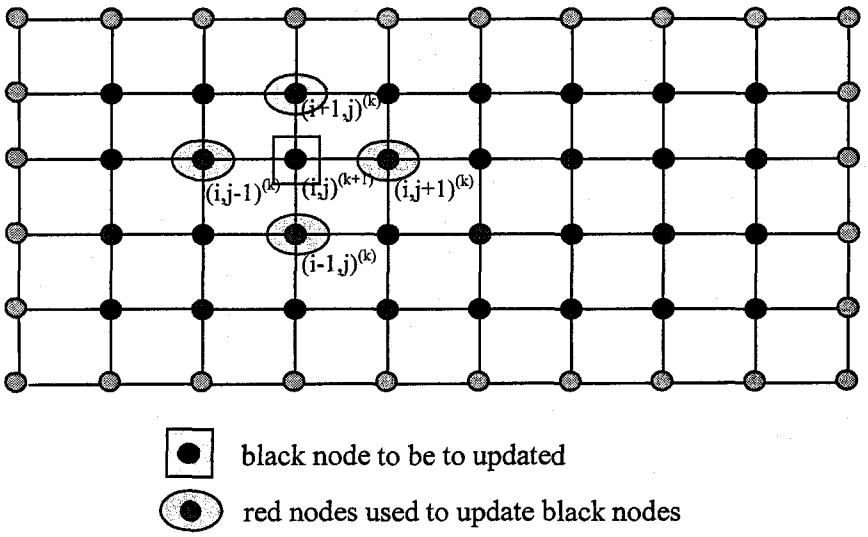

Figure 6.9 Phase 1: updating the values of the black nodes using Eq. (6.6)

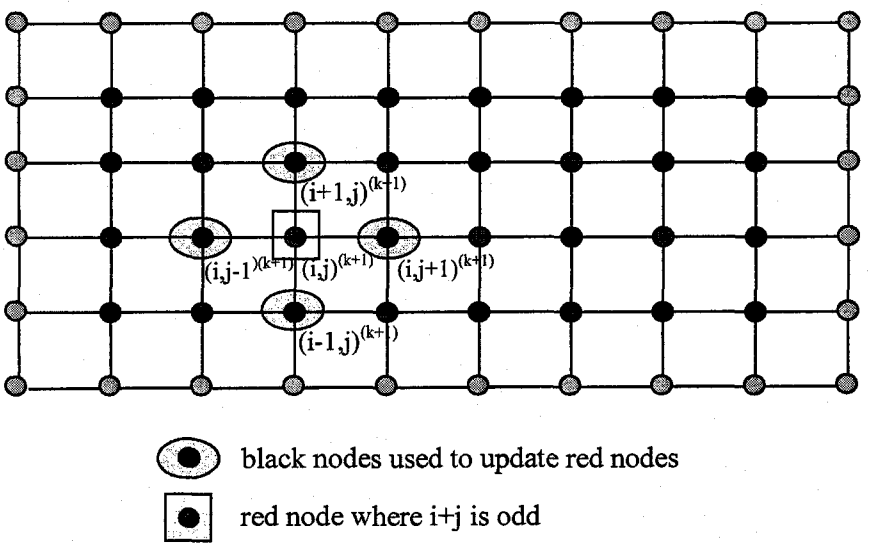

Figure 6.10 Phase 2: updating the values of the black nodes using Eq. (6.7)

As with the Jacobi's iteration, it is necessary to synchronize at the end of each phase so that the data can be passed across the subdomain boundaries. The subdomain in Gauss-Seidel or SOR method is also a row block consisting of red and black nodes. All

values at red nodes or black nodes can be computed concurrently. The parallel algorithm is given in Figure 6.11.

Algorithm 3: Parallel Gauss-Seidel and SOR algorithm for shared memory platforms

Scatter the initial guess of Tnew onto all processes and each stores Tnew_local
process 0 reads and broadcasts constant ω

```
Process q:
convergent = false
do {
    // Phase 1: update red nodes, if i+j is odd
    for each red node (i, j) located in block q {
        for each local interior nodes of block q
            update Tnew_local[i,j] ,   // using Eq. (6.6)
        for each global interior node located in the block q
            compute the Tnew_local[i,j]   // using black values
        for each global boundary node located in the block q
            compute the Tnew_local[i,j] according to the boundary condition
        // synchronization
        gather Tnew_local data from all processes and store them to Tnew
    }
    // Phase 2: update black nodes, if i+j is even
    for each black node (i, j) located in block q {
        for each local interior nodes of block q
            update Tnew_local[i,j] ,   // using Eq. (6.7)
        for each global interior node located in the block q
            compute the Tnew_local[i,j]   // using red values
        for each global boundary node located in the block q
            compute the Tnew_local[i,j] according to the boundary condition
        // synchronization
        gather Tnew_local data from all processes and store them to Tnew
    }
        if Convergent {
            convergent = true;
        }
    } // end for
} while (k < maximum_iteration and NOT convergent)
gather local results from all processes and store them to global matrix Tnew
```

Figure 6.11 Parallel algorithm of Gauss-Seidel and SOR method for shared memory platforms

Algorithm3 differs from Algorithm 2 in that (1) it needs two phases (red and black phases) for each iteration; and (2) both black and red values are stored in the same matrix Tnew and it simplifies the updating procedure. Algorithm3 can be implemented in a similar way to Algorithm 2.

6.4 Development Environment and Implementation

Many programming languages and libraries have been developed for explicit parallel programming. These differ in the view of the address space, degree of synchronization and multiplicity of programs. The message passing interface (MPI) [Pacheco 1997], released in 1994, is a standard for writing message passing programs. MPI was originally targeted for distributed memory systems, such as a cluster of PCs, but it is supported on virtually all high performance computing (HPC) platforms, including shared memory platforms, e.g., SGI Origin. We choose MPI for developing parallel computing applications because of its standardization, portability, performance, functionality and availability. The subroutines and functions in MPI can be called from Fortran, C or C++ [Karniadakis 2003]. The standard C++ supports object-oriented programming and it is very suitable for the component-based model described in previous chapters. In addition, the integrated model described in previous chapters was originally implemented sequentially in C++, so it is straightforward to modify the serial codes for parallel computing. The development environment is summarized as follows:

- Platforms: SGI Origin supercomputer and PC clusters
- Operating systems: Unix and Windows XP
- Languages and libraries: Standard C++, MPI and MPICH implementation
- Compilers: mpic++ on Unix and Visual C++ 6.0 compiler on Windows XP

For most iterative scientific computing applications, when data decomposition technique is employed, all processes execute the same code but perform on different data sets. This is the single program and multiple data (SPMD) paradigm used for implementing Algorithms 2 and 3. Parallelism in MPI is explicit so developers need to consider how different processes perform their task and communicate with each other in the parallel algorithm design. In this study, the computations in the substrate and gas domains are the most expensive tasks which require parallel computing. The computational task in the rod domain is insignificant and is not implemented in parallel. There are more than 3000 lines of C++ code in the parallel program. The structure of the program is given in Figure 6.12.

```
#include "mpi.h"    // include MPI library
...
int main(int argc, char** argv)
{
    ...
    // Start parallel computing using MPI //
    MPI_Init(&argc, &argv);
    MPI_Comm_size(MPI_COMM_WORLD, &total_p);   // number of processes
    MPI_Comm_rank(MPI_COMM_WORLD, &my_rank);   // rank of process
    ...
    // compute substrate temperature in parallel
    SubTempPara(300, imax, n_bar, drs, dxs, rs, xs, ts_local, total_p, my_rank);
    ...
    // compute gas temperature and molar ratio in parallel
    ...
    // compute rod growth sequentially
    MPI_Finalize();
    return 0;
}
```

Figure 6.12 Structure of parallel computing program

MPI provides different ways for passing messages among the processes. The two basic communication functions are MPI_Send and MPI_Recv that a message is sent to a destination process or received from a source process. Several functions are used for more efficient message passing, including MPI_Bcast, MPI_Scatter, MPI_Allgather, MPI_Barrier and MPI_Wtime, as shown in the following code segment. For more details about these functions, see the MPI specifications.

```
//P0 send a double array xs with size jmax to all other processes
MPI_Bcast(xs, jmax, MPI_DOUBLE, 0, MPI_COMM_WORLD);
// P0 send row blocks to all other processes based on their ranks.
MPI_Scatter(ts, n_bar*imax, MPI_DOUBLE, ts_local,
        n_bar*imax, MPI_DOUBLE, 0, MPI_COMM_WORLD);
//gather Tnew_local from all processes and store in Tnew available by all
MPI_Allgather(ts_local, xmax_local*rmax_local, MPI_DOUBLE, tsnew,
        xmax_local*rmax_local, MPI_DOUBLE, MPI_COMM_WORLD);
MPI_Barrier(MPI_COMM_WORLD); //enforce synchronization
double start = MPI_Wtime(); // to compute the elapse time
```

Figure 6.13 Message passing functions used

6.5 Parallel Computing Performance

It is important to examine the benefits from the parallelism. In this section, we are interested in knowing how much performance gain is achieved by parallelizing a given application over a sequential implementation. Speedup S is a measure that estimates the relative benefits of solving a problem in parallel. S is defined as the ratio of the serial runtime of a sequential algorithm for solving a problem to the time taken by the parallel algorithm to solve the same problem on a parallel computer with p identical processing elements. The serial runtime and parallel runtime are denoted by T_s and T_p, respectively. Thus, we have

$$S = \frac{T_s}{T_p} \tag{6.7}$$

Only an ideal parallel system containing p processing elements can achieve a speedup equal to p. If $p = 1$, the parallel system uses more computing resources but there is no performance gain. Usually, the range of S is

$$1 \le S \le p \tag{6.8}$$

In practice, ideal behaviour is not achieved because the processing elements cannot devote 100% of their CPU time to the computations of the algorithms. This is determined by the serial portion of a parallel algorithm or the computational load unbalance. Efficiency E is a measure of fraction of time for which processing elements are usefully employed. Efficiency E is defined as the ratio of speedup to the number of processing elements, given by Eq. (6.8). In practice, speedup is less than p and efficiency is between zero and one.

$$E = \frac{S}{p} \tag{6.9}$$

The parallel performance of the entire integrated model, given in Chapters 3, 4 and 5, depends not only on the computational tasks, but also on their complex task dependency and implementation, which makes the theoretical parallel performance analysis difficult or even impossible. Instead, we only examine the performance gains of parallel Jacobi's algorithm, Gauss-Seidel algorithm, and SOR algorithms. The elapsed time of the algorithms can be obtained using the following code:

```
Double start, end, elapsedtime          // variable declaration

MPI_Barrier(MPI_COMM_WORLD);  // synchronization
start = MPI_Wtime();                    // return the time (in seconds)

// parallel computing for substrate
SubTempPara(3000, imax, n_bar, drs, dxs, rs, xs, ts_local, total_p, my_rank);

MPI_Barrier(MPI_COMM_WORLD);  // synchronization
end = MPI_Wtime();                      // return the time (in seconds)
elapsedtime  = end - start;             // compute parallel runtime
```

Figure 6.14 Compute elapsed time

The serial elapsed time depends on the hardware, but with the same initial guess, the total numbers of iterations for each of the Jacobi, GS and SOR method are the same for different platforms. If $\varepsilon = 0.0001$, the total iteration numbers corresponding to Jacobi, GS and SOR are about 15000, 8000 and 300, respectively. We found that the SOR method converges very fast if $\omega = 1.9$.

The different testing cases are performed on a SGI Origin machine with 8 processors. The actual speedup and efficiency for p = 2, 4, 8 are given in Figs 6.15 and 6.16, respectively. With an increase in the number of processing elements, the speedups increase but are less than the ideal speedup because of the extra work and communication cost during parallel computation. The speedup of the Jacobi algorithm is slightly larger than that of the Gauss-Seidel or the SOR algorithm. With an increase in the number of processing elements, the efficiencies of these algorithms decrease, caused by the fact that the more processing elements are employed, the more communications are needed among these processing elements. The speedups and efficiencies of the Gauss-Seidel or the SOR algorithms are very close because their implementations are the same except for the values of the constant ω.

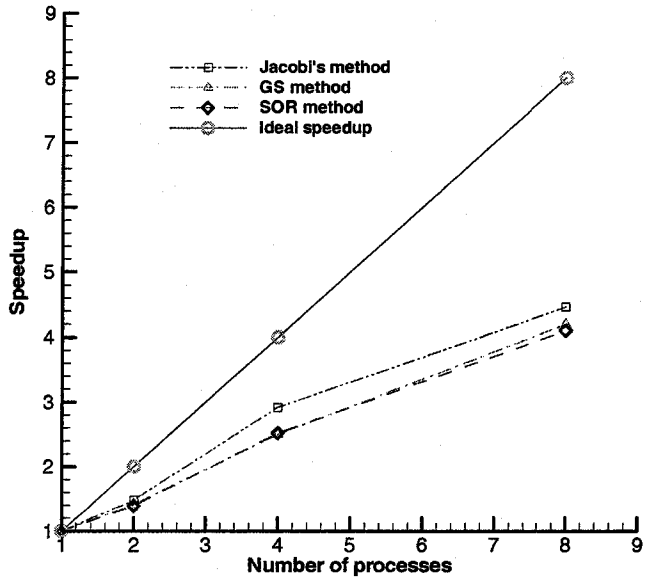

Figure 6.15 Actual speedups for p = 2, 4, 8

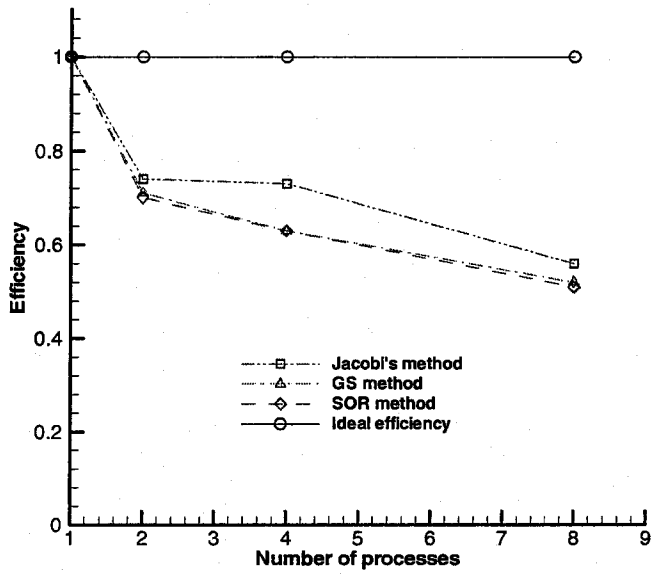

Figure 6.16 Actual efficiencies for p = 2, 4, 8

It is noted that the integrated model proposed in this study was originally implemented on Windows operating system using Visual C++, and then implemented in

parallel using standard C++ and MPI. The results of the parallel implementation are the same as those obtained by serial implementation, which shows the correctness of the parallel algorithm and its implementation. This parallel application is portable and can be executed on both Unix/Linux and Windows XP. The elapsed time may change on different platforms because of different hardware, network connection and compiler. The actual speedup and efficiency can be obtained and analyzed similarly.

CHAPTER 7

MODELING OF AN AXISYMMETRIC ROD WITH GAS-PHASE HEATING

Hybrid mathematical models, numerical methods, and corresponding algorithms have been developed in Chapters 3, 4, and 5. In this chapter, we consider the common reaction of silicon from silane, as described in Equation (4.1), and simulate the growth of the rod and investigate the affects of the gas-phase reaction on the deposition rate. The results for different parameters will be presented and analyzed.

7.1 Description of a Typical Rod Growth

Most microfabrication processes are three dimensional. Here, it is assumed that the rod is axisymmetric so the three-dimensional rod deposition problem can be reduced to a simpler two dimensional problem. The rod deposition process consists of three domains: (a) substrate, (b) rod, and (c) gas-phase reaction region. There is an interface between the rod and substrate at which the boundary conditions are the same for both the rod and substrate domains. The surface on the top part of the rod is the interface between the rod and the gas phase domains, and at the interface, the temperature and species flux boundary conditions are the same. Except for the boundary, each domain forms an independent system. This property motivates us to use a separate coordinate system for

each domain, and use boundary conditions to combine them together to form an integrated model which considers both kinetically limited and mass transport limited deposit growth. The advantage of this separation makes it convenient to use different meshes and coordinate systems for different domains. The substrate domain is a cylinder with radius R_s and height Z_s . The domain is evenly divided into an ImaxS × JmaxS mesh with mesh size Δz_s and Δr_s, as shown in Figure 7.1, where ImaxS and JmaxS are the maximum number of grids in the r and z directions, respectively. The rod is grown layer by layer, as described in Chapter 4. At each step, the rod grows Δz_d, where Δz_d = 0.005. The gas-phase domain is also a cylinder with radius R_g and height Z_g. The numbers of grids in the r and z directions are ImaxG and JmaxG, respectively. The mesh sizes in the r and z directions are Δr_g and Δz_g, respectively.

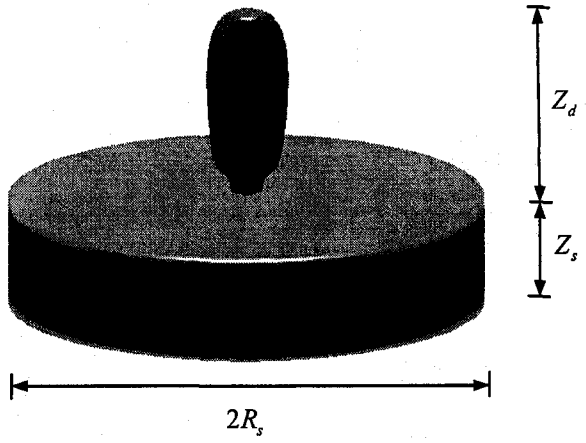

Figure 7.1 Rod grown on the substrate

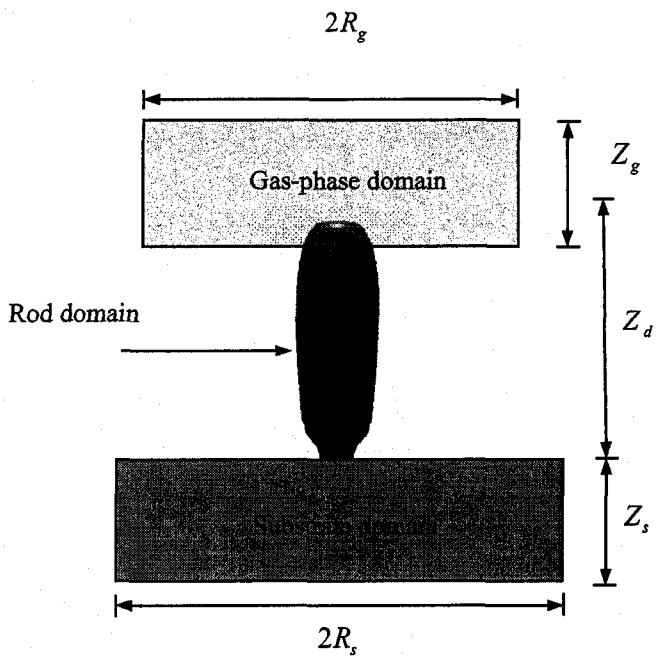

Figure 7.2 Substrate, deposit, and gas-phase domains

7.2 Model Parameters

The geometry parameters in the integrated model described in chapter 4 and 5 are summarized in Table 7.1. In addition to the geometry parameters of the model, the physical properties of the substrate, deposit, and LCVD precursor determine the outcome of the LCVD process. The LCVD deposition rate is a function of many variables, such as the temperature distribution induced by the laser power, vapor pressure of the precursors, thermal conductivities, and molar ratio in the gas-phase. The parameters that ultimately limit and control the process lie within the realm of thermal physics and continuum mechanics. Among these physical parameters, the laser power is the process parameter

that most influences the rod growth. The physical properties of the substrate, rod, and gas used in the model, described in Chapter 4 and 5, are given in Table 7.2

Table 7.1. Geometry parameters

Domains	Parameters	Values
Substrate	Diameter R_s (mm)	0.15
	Height H_s (mm)	0.15
	ImaxS	100
	JmaxS	100
	Grid size Δr_s (mm)	0.0015
	Grid size Δz_s (mm)	0.0015
Rod	Grid size Δz_d (mm)	0.005
Gas-Phase	Diameter R_g (mm)	0.075
	Height H_g (mm)	0.04
	ImaxG	150
	JmaxG	80
	Grid size Δr_g (mm)	0.0005
	Grid size Δz_g (mm)	0.0005

Table 7.2. Physical parameters

Parameters	Values
E_a	$1.82\times10^5(J/mol)$
R	$8.314(J/mol\cdot K)$
K_0	$8.0\times10^4(mm/\sec)$
T_∞	$300(K)$
P_0	$0.03(W)$
σ	$0.0005(mm)$
k_s	$0.0017(W/m\cdot k)$
k_D	$0.0619(W/m\cdot k)$
D_{AB}	$10.0\ (mm\cdot mm/s)$
$T_m(K)$	$1680\ (K)$

7.3 Substrate Temperature and Initial Growth

When a laser beam is focused on the surface of a substrate, the substrate absorbs the laser power. In a local reaction zone, the temperature is high enough for pyrolytic laser-induced chemical deposition to take place. In the kinetically-limited rod growth model, it is assumed that the rod is divided into a number of layers. For each layer, we calculate the temperature distribution and predict growth in the r and z directions on the surface of the rod. One question is how to specify the initial rod growth. Since the subsequent rod growth is sensitive to the initial guess, as discussed in Section 7.6, an inaccurate initial rod growth may result in an incorrect result.

In this section, a substrate component is added to the model to predict the temperature distribution in the substrate and hence simulate the initial growth. The substrate is a cylinder with a diameter of 3.0mm and a height of 1.5mm. Because it is symmetric along the z axes, one only needs to consider the z and r direction. A 3D substrate domain can be reduced to a 2D rectangular domain in order to simplify the calculation. The rectangular substrate domain is decomposed into a mesh with a mesh size of 0.0015 by 0.0015. There are 200 and 100 grids in the r and z directions, respectively as shown in Figure 7.4. The laser beam is focused at the center of the surface of the substrate. The laser power is absorbed by the substrate and heat flow in the substrate is described by Equation (3.31) which is discretized in Equation (5.6). The laser-induced temperature distribution in the substrate is given in Figure 7.5. Near the center of the substrate at which the laser beam is focused, the temperature is higher and the temperature drops down with increased distance from the center.

Once the temperature distribution on the surface of the substrate is available, growth rate can be calculated at each grid point on the surface of the substrate using Equation (3.33). Note that at the initial stage, the deposit grows only along the z direction because a normal growth rule is assumed. The higher the temperature, the larger the growth rate. It is assumed that maximum rod growth at the origin is 0.0005mm. The initial growth distribution of the rod is predicted based on the growth rate at each grid point on the substrate surface and the maximum growth at the origin, as given in Figure 7.3(a). How initial rod growth affects the rod geometry will be discussed in Section 7.6.

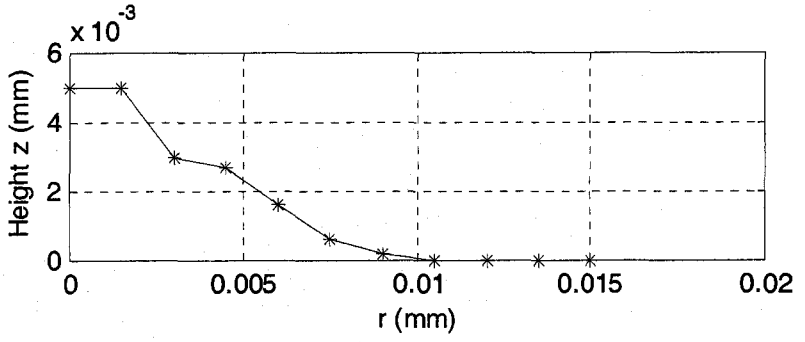

(a) Calculated

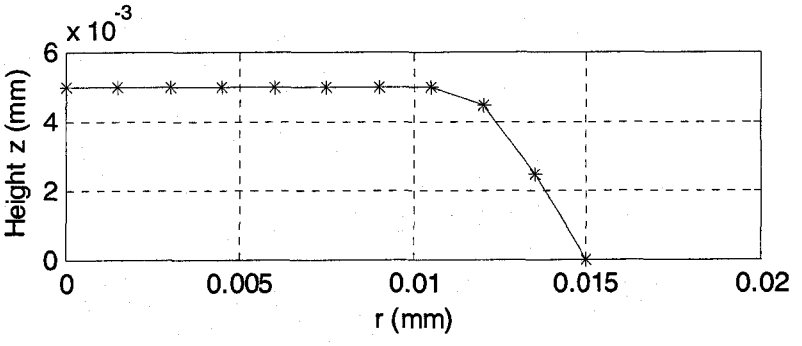

(b) Guessed

Figure 7.3 Initial growth of the rod

7.4 Gas-Phase Heating and Molar Ratio

When a laser beam is focused on the top of the rod, heat from the laser will be absorbed and transported to the surrounding area. This change leads to a temperature distribution in the gas-phase domain which contains the top part of the rod, as shown in Figure 7.2. The size of the gas-phase domain depends on the gas-phase dynamics and the boundary condition. Strictly speaking, the size of the domain should be large enough so that the boundary condition does not affect the temperature and molar ratio distributions. However, our interest is the molar ratio in the local area near the top part of the rod, in which case the size of the domain can be relatively small without significantly affecting the molar ratio and rod growth near the tip of the rod. In the hybrid numerical model, the gas-phase domain is a rectangle with a width of 0.075mm and a height of 0.04mm. The heat transport is described by the diffusion equation, Equation (5.13), and the corresponding boundary conditions, Equations (5.14) and (5.15). To numerically solve the equation, the gas-domain is evenly decomposed into a rectangular mesh with a mesh size of 0.0005mm in both the x and y directions, as shown in Figure 7.22. The shaded part of the gas-phase domain is the top part of the rod, which is not involved in the gas-phase calculation. The surface of the rod is the inner boundary at which the gas-phase temperature is equal to the temperature of the rod surface. It is noted that the gas-phase domain only contains the top part of the rod. After the rod grows to a certain height, the gas-phase domain will move with the growth of the rod. The part of the rod included in the gas-phase domain is determined by the specified temperature threshold value, e.g. 1500K. The advantage of this strategy is that the gas-phase domain has a fixed size even if the rod grows longer and it facilitates domain decomposition and calculations.

The temperature distribution in the gas-phase domain is obtained by solving the diffusion equation, Equation (5.13), using the numerical scheme in Equation (5.15). The gas temperature distributions at iterations 10, 30, 50, 70, 100 are given in Figures 7.7 - 7.11, respectively. It is seen from these figures that the temperature is highest near the rod surface and drops off with distance from the surface. Also, the temperature distributions corresponding to different iterations are not substantially different. This is because the deposit shape and temperature at the top of the rod do not change substantially after the rod grows to a certain height, as shown in the next section.

After the temperature distribution is obtained, the molar ratio in the gas-phase domain can be computed from Equations (5.23), (5.27), (5.28), and (5.30). Molar ratio distributions in the gas-phase domain with respect to iteration 10, 30, 50, 70, and 100 are given in Figures 7.12 - 7.16. It is seen that the molar ratio is 1.0 near the outer boundary and less than 1.0 near the top surface of the grown rod.

7.5 Rod Temperature and Geometry

When the laser beam is focused on the substrate or the top of the rod, the rod absorbs the energy and its temperature goes up. In the meanwhile, part of the heat transports to the lower part of the rod or to the substrate. Convection also leads to heat loss on the surface of the rod surface. The temperature distribution of the rod determines rod growth and its geometry which in turn affects the temperature distribution. If the temperature is higher than a certain threshold, the effect of mass limited transport on the growth rate needs to be considered. This interdependent, dynamic process is described using the mathematical models in Chapters 3 and 4. The rod temperature is calculated from Equations (5.1) and its corresponding boundary conditions. For each layer of the

rod, we assume that the temperature is the same, so we need only to calculate the temperature distribution along the height of the rod, as shown in Figure 7.17. Since the rod absorbs the laser power from where the laser beam is focused, the temperature is higher near the top of the rod and it decreases with a decrease in the height of the rod. During deposition, the laser power and the laser position do not change. For different iterations, the highest temperatures near the top of the rod are given in Figure 7.18. With the increase of the rod height, the highest temperature increases a bit but after iteration 50, there is no significant change. Rod growth is determined by the highest temperature and molar ratio it the top of the rod. If the highest temperature and molar ratio remain constant, the growth rate is a constant. Figure 7.19 shows the time needed to grow 0.0005mm at different iterations. It is seen that after iteration 60, the time does not change and the rod grows at a constant speed.

Near the bottom, the temperature is relatively low and the radius of the rod is small, thus limiting the heat transport to the substrate. If the area of the interface between the rod and the substrate is small, we may ignore the heat loss at the bottom of the rod. After the rod grows to a certain height, the boundary condition of heat transfer at its bottom does not affect rod growth, in which case one does not have to consider the substrate temperature. Hence, we assume that the temperature on the bottom boundary of the rod is T_{∞} after iteration 10. Without loss of accuracy, this assumption can shorten the CPU time.

With the temperature distribution known, one can normally calculate the growth rate. However, at the top part of the rod, one may need to consider the effect of reaction in the gas-phase domain. With a hybrid model, integrating both kinetically limited and

mass transport limited growth, given in Chapter 3 and 4, rod growth is computed using Equations (5.34) and (5.35). The substrate and the rod for iterations 10 to 100 are given in Figures 7.20 – 7.29 in which they are represented as three dimensional plots. It is seen from these figures that the radius of the rod is relatively small near the surface of the substrate because at the beginning, the laser beam is focused on the surface of the substrate, where the heat diffusion coefficient is relatively small and limits heat transport to the surrounding area. Thus, the temperature at the local area is high and leads to a fast initial growth. After the first iteration, both the initial growth and the substrate will determine the shape and rod size at the early deposition stages. The initial growth is analyzed in Section 7.1.

To understand better the deposition process and geometry change with respect to different iterations, the rod shapes at different deposition stages are given in Figure 7.30. After iteration 30, the shape of the rod does not change.

7.6 Influence of Initial Growth

Subsequent rod growth depends on its initial state. To demonstrate how an initial growth guess affects rod growth and its geometry, we compare the two sets of results corresponding to two initial growths. A guessed initial growth of the rod is given in Figure 7.3(b). All other physical and mathematical parameters remain the same as those in Section 7.2.

Rod heights at different iterations are given in Figures 7.31-7.35. The temperature distributions and the rod shapes with respect to different iterations are given in Figures 7.36 and 7.37. Comparing the rod shapes for predicted (Case 1) and guessed initial growths (Case 2) at iteration 100, as shown in Figures 7.30 and 7.37 respectively,

it is seen that the rod shapes change significantly because of the different initial guess. In Case 1, where a predicted initial rod growth is used for simulating subsequent rod growth, the radius of the rod becomes larger at iteration 5, while in Case 2 with a guessed initial rod growth, the radius of the rod increases gradually. This difference can be explained by heat flow in the rod. In Case 1, the diameters of the rod at the first several iterations are small; the areas on the cross sections are also smaller, which limits heat transport down to the substrate. The temperature at the top part of the rod at iteration 5 increases significantly and results in a sudden change of the rod diameter. In case 2, the area of the cross section of the rod is larger. This causes changes in the heat flow and temperature distribution in the rod, which lead to a gradual change in rod shape.

The highest temperatures of the rod tip at different iterations using predicted initial growth and guessed initial growth are given in Figure 7.38. The highest temperatures are lower using predicted initial growth than using guessed initial growth. The growth rates corresponding to the rod temperatures with respect to the predicted initial growth and guessed initial growth are given in Figure 7.39. At each iteration, the maximum growth is 0.005mm, and the growth time at different iterations for two initial growths is shown in Figure 7.40. At the same iteration, the rod requires less time to grow 0.005mm using predicted initial growth because it temperature at the rod tip is higher than that using guessed initial growth.

From the comparison of results obtained from predicted and guessed initial growths, one can see that initial growth does affect the shape of the rod during the entire process of deposition. Thus, a mathematical model component to predict the temperature distribution of the substrate and initial rod growth should be included in the integrated

model, especially in the first several iterations, even if this component may not be involved in the calculation after the rod grows to a certain height.

7.7 Kinetically Limited Rod Deposition

This section presents predicted results such as rod geometry, growth rate, growth time and temperatures, obtained from a kinetically limited model. Also, we demonstrate how gas-phase domain simulation affects rod growth by comparing the hybrid model and the kinetically limited model. The model parameters used in the kinetically limited model are the same as in the hybrid model except for the growth rate computation, e.g. the same initial condition and the same laser power were used. In the kinetic model, the gas phase component is turned off and is not involved in the simulation process. The growth rate is determined only by the temperature on the surface of the rod, as shown in Equation (3.24), without taking into account the effect of mass-transport limited deposition. In order to clearly illustrate how mass transport in the gas phase affects the deposition process, we compare the temperature, growth rate, and growth time between the hybrid and kinetic models, Figures 7.41 - 7.43. In the kinetic model, there is a rise in the rod temperature. In hybrid deposition model, there is a heated reaction zone near the tip of the rod in which the precursor molecule decomposes and any solid reactant is left behind as a deposit on the surface of the rod. Mass transport limited growth becomes effective when the temperature reaches a value higher than a certain threshold. Usually, mass transport limited growth rate is lower than the kinetically limited growth rate, as shown in Figure 7.42, because in the mass transport limited case, the amount of precursor arriving at the surface of the reaction zone is insufficient to support an exponential increase in growth rate caused by an increasing temperature. Hence, the growth process slows down,

depending on the laser power, activation energy, precursor, substrate, and deposit properties. In both mass-transport limited and kinetically limited growth cases, the growth rates slightly increase as the rod grows. However, after the rod grows to a certain height (e.g. 70 iterations), the growth rate remains constant.

The LCVD is an iterative process in which the temperature distribution and molar ratio in the reaction zone determine the growth rate at each point on the surface of the rod, and hence determine the geometry of the rod. The rod shape, in turn, affects the temperature distribution. In the hybrid model, the growth rate is lower than that in kinetic model, especially in the first several iterations, and it changes the rod shape at its early growth stage. The rod geometry influences the temperature distribution. This distribution, at each iteration at the tip of the rod, is given by Figure 7.41 for both mass-transport limited and kinetically limited deposition. In both cases, the temperatures at the tip of the rod increases as the rod grows higher and become constant after the rod grows to a certain height. However, the temperature at the tip of the rod in the hybrid model is slightly higher than that in the kinetic model.

The rods at iteration 50 and 100 obtained from the kinetic models are given in Figures 7.44 and 7.45. Under the given computational conditions, the rod shapes obtained from the kinetic model are quite similar to those (Figures 7.24 and 7.29) predicted from the hybrid model, but its growth rate is higher and it needs less growth time at each iteration. However, this growth time may not be achieved because of the mass transport limitation in the reaction zone when the temperature is higher than the threshold.

7.8 Rod Growth for Different Laser Powers

Laser power is the heat source leading to the temperature distribution and thereafter the deposition of the solid-phase reaction product such as Si. Different laser powers correspond to different temperature distributions, and hence to different rod shapes. In this section, the same model parameters as those in Section 7.2 are used in the simulation (using both the kinetic and hybrid models) with the exception of the laser power. This was done in order to demonstrate the effect of laser power on rod geometry.

With a lower laser power, the heat transferred to the rod during the deposition process is lower. The temperature at the tip of the rod is high, but the temperature at the lower part of the rod is relatively low because of the heat loss resulting from convection. Thus, the rod grows along the z axis with no significant growth in diameter, as shown in Figure 7.46. As the laser power increases, more heat is absorbed by the rod. Because convection is insufficient for dissipating all of the heat, part of the heat is transferred down to the lower part of the rod or substrate, resulting in a high temperature distribution, not only at the tip of the rod but also in the lower part of the rod. The high temperature at the tip of the rod leads to growth along the z axis, while the temperature distribution on the surface below the rod tip causes growth in the diameter. Thus, one may obtain a rod with a larger diameter. Rods, grown with laser powers 0.05W and 0.10W, are given in Figures 7.47 and 7.48, respectively. To better illustrate the effects of laser power on rod geometry, the rod shapes at different iterations with laser powers 0.02W, 0.05W and 0.10W are given in Figures 7.49 – 7.51. From these figures, one can see that for low laser power, one may grow a thin rod with its diameter unchanged. However, for high laser

power, one may obtain a thick rod with a changing diameter. Hence, control of the laser power enables one to grow rods with different shapes.

7.9 Summary

In this chapter, both the hybrid and kinetic models proposed in Chapter 3, 4, and the numerical methods presented in Chapter 5 are applied to simulate the LCVD process and predict rod growth. The temperature distribution in the substrate is predicted and used to determine the initial growth of the rod. Comparison of results from computed and guessed initial growths shows that initial growth is important because it is the starting point of the whole interdependent deposition process. A guessed initial growth may change the shape of the grown rod. In the hybrid model, the gas-phase is simulated and the molar ratio is computed. The molar ratio can affect the growth rate because of the mass-transport limitation in the reaction zone. Under the modeling conditions reported here, there is no significant difference in rod shape between the hybrid model and the kinetic model, but the former slows down the deposition process and needs more growth time at each iteration. Laser power is the direct factor leading to the rise of temperature and to the growth of the rod. With lower laser power, the rod is thin and has a cylindrical shape. With higher laser power, the rod is larger in diameter and its diameter changes over time. Mass-transport limited growth is a very complex process which requires further investigation. Of interest in this regard is to extend the present models in order to deal with chemical reactions in the gas-phase zone or with time-dependent parameters.

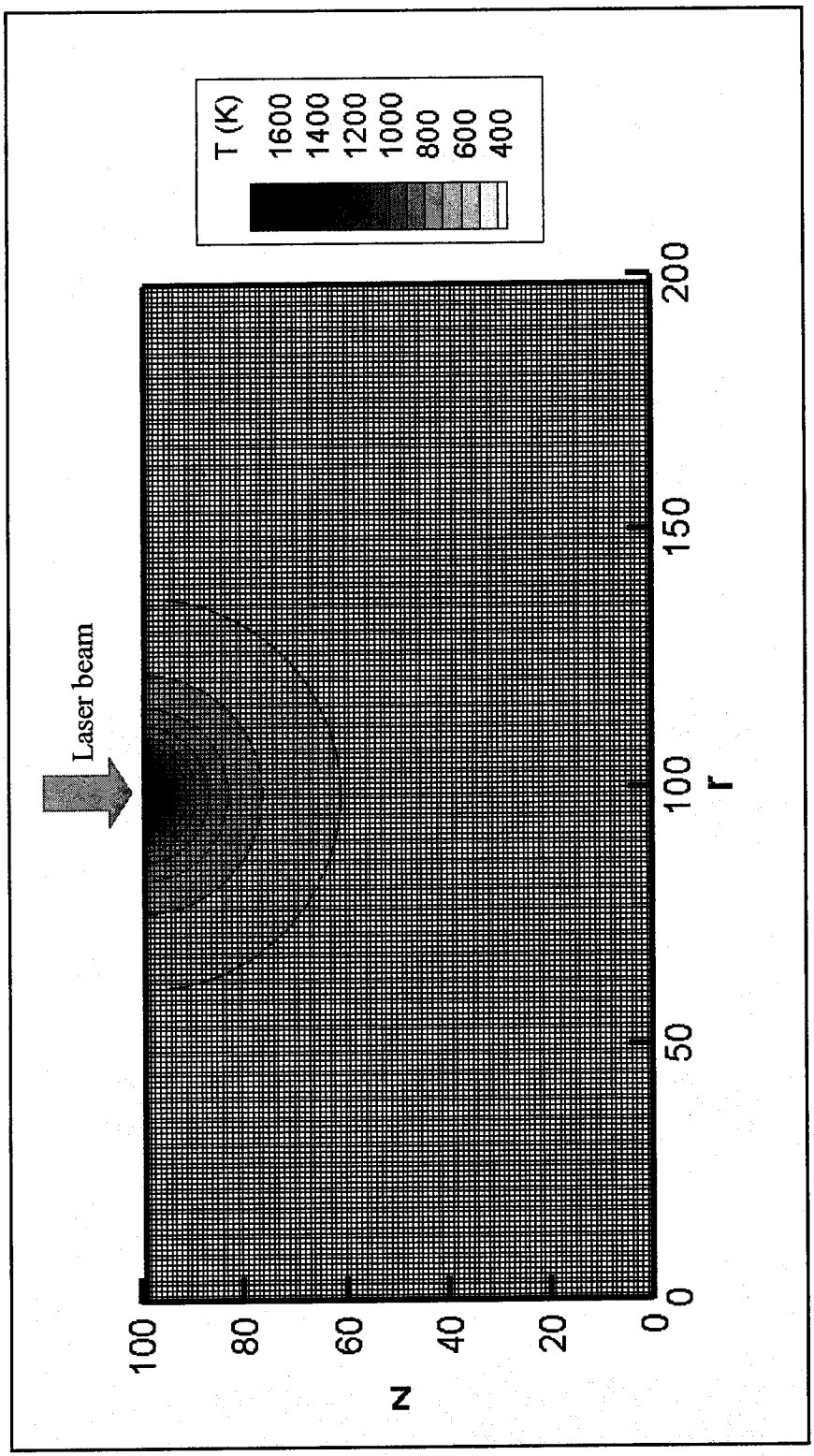

Figure 7.4 Mesh of the substrate

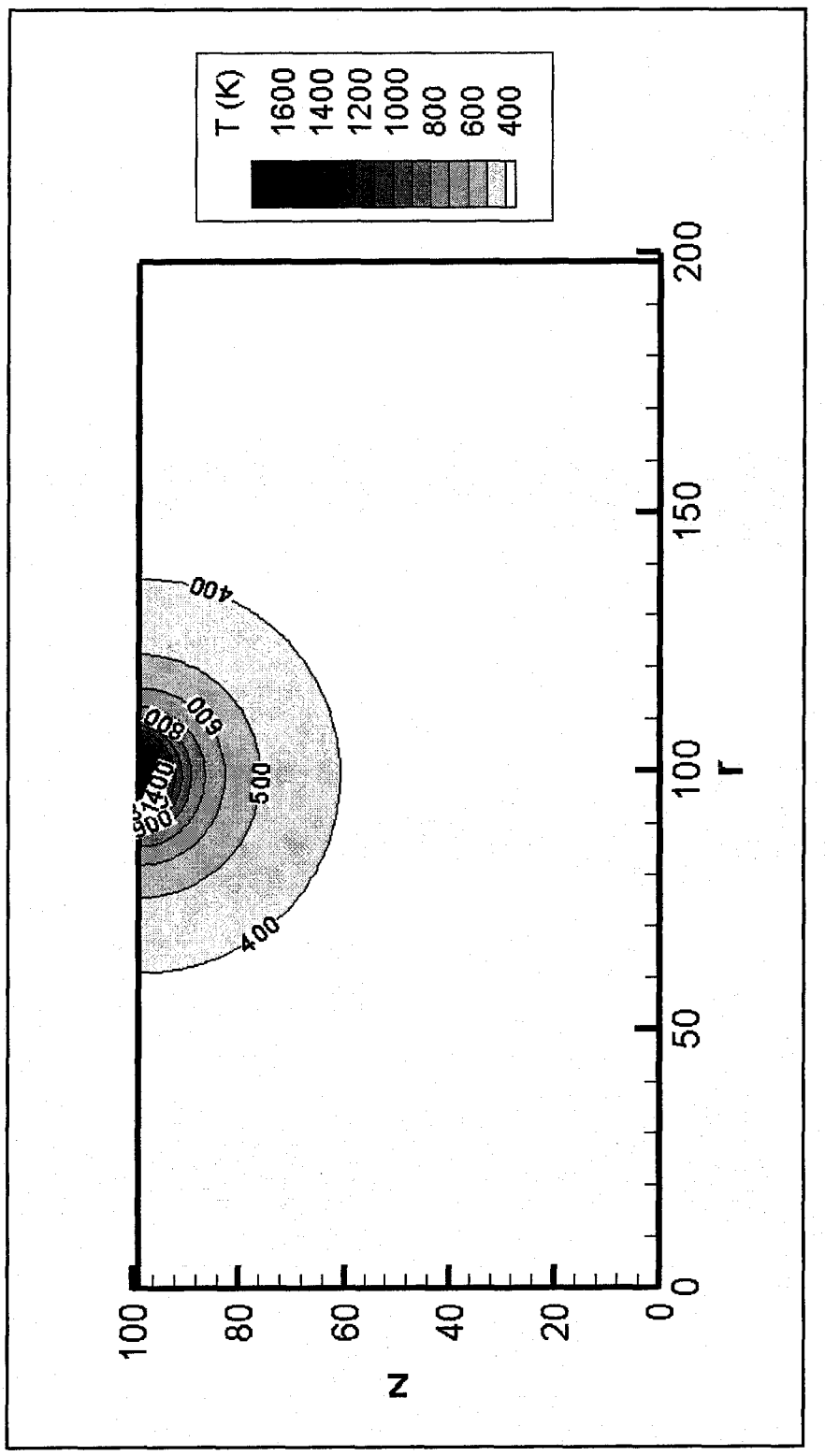

Figure 7.5 Temperature distribution of the substrate

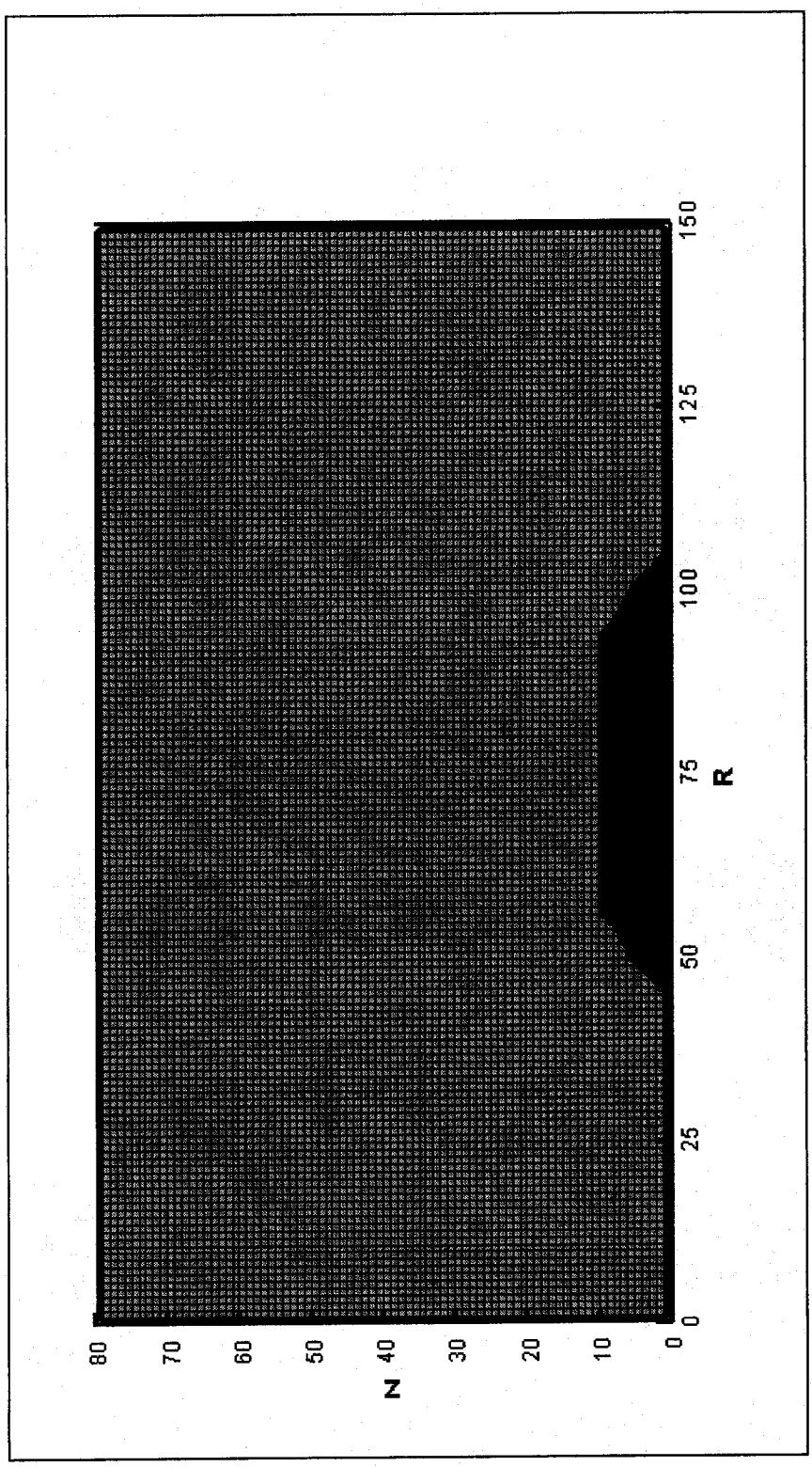

Figure 7.6 Mesh in the gas-phase domain around the top part of the rod

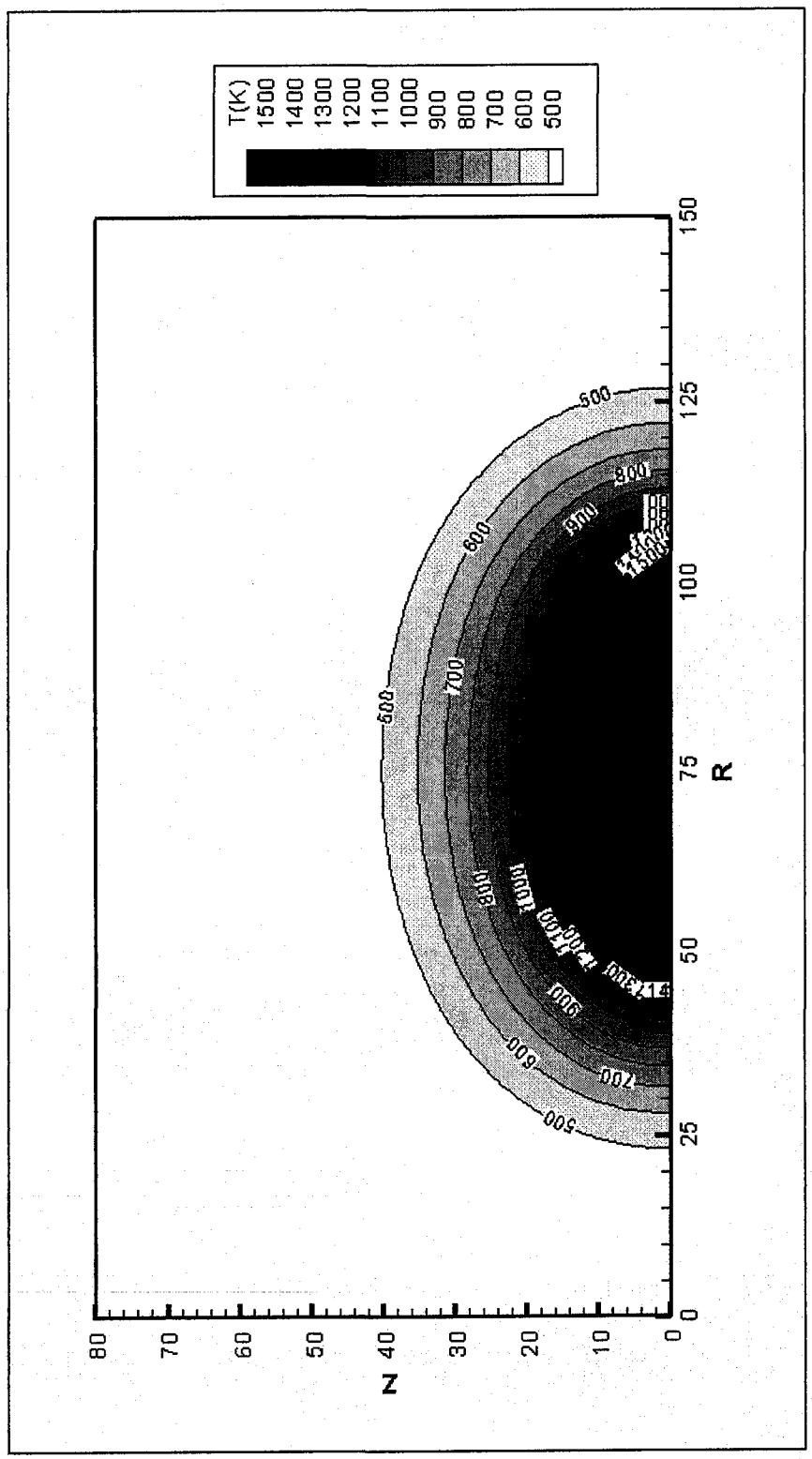

Figure 7.7 Gas temperature distribution (mesh size=0.0005mm, IT=10)

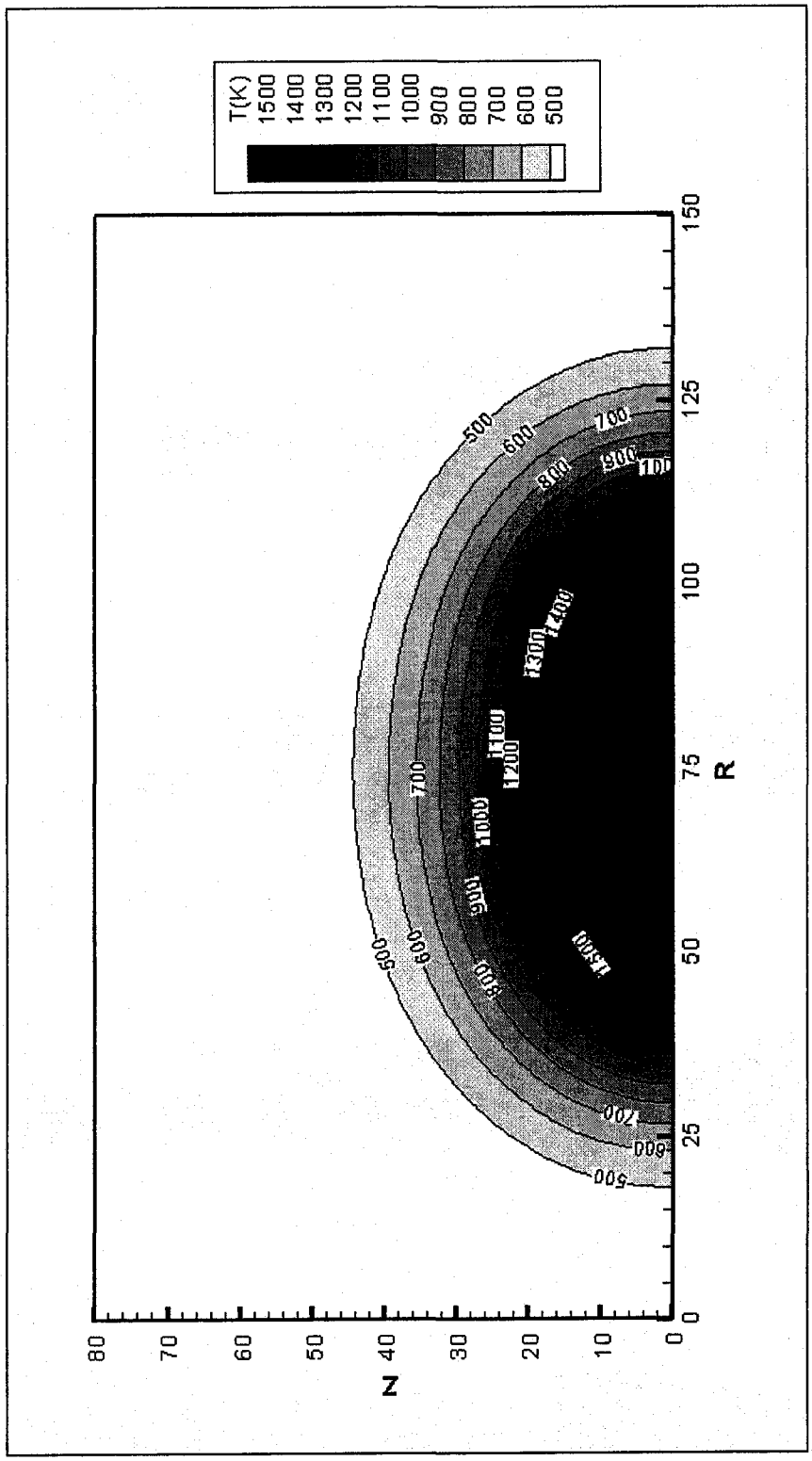

Figure 7.8 Gas temperature distribution (mesh size=0.0005mm, IT=30)

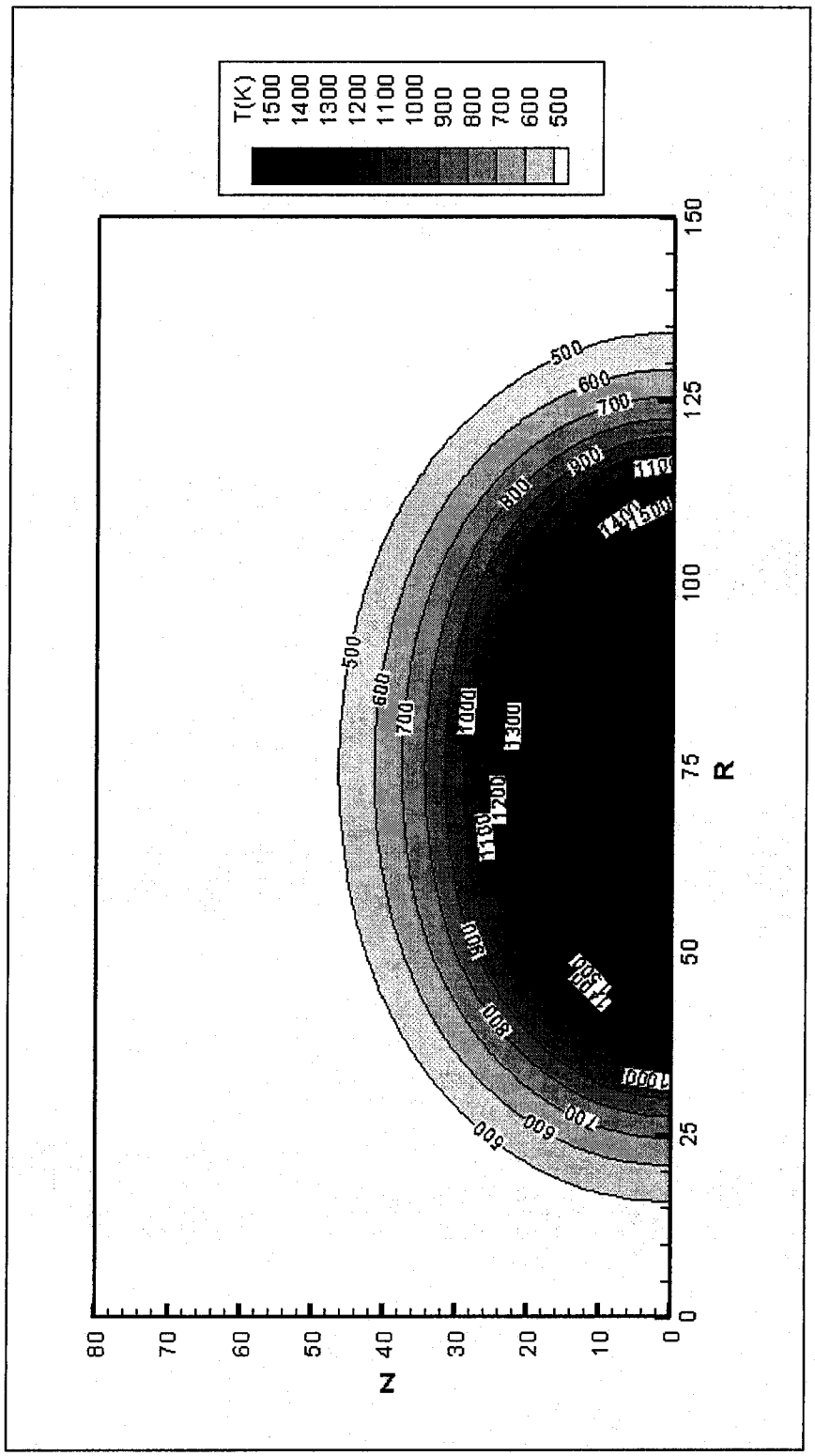

Figure 7.9 Gas temperature distribution (mesh size=0.0005mm, IT=50)

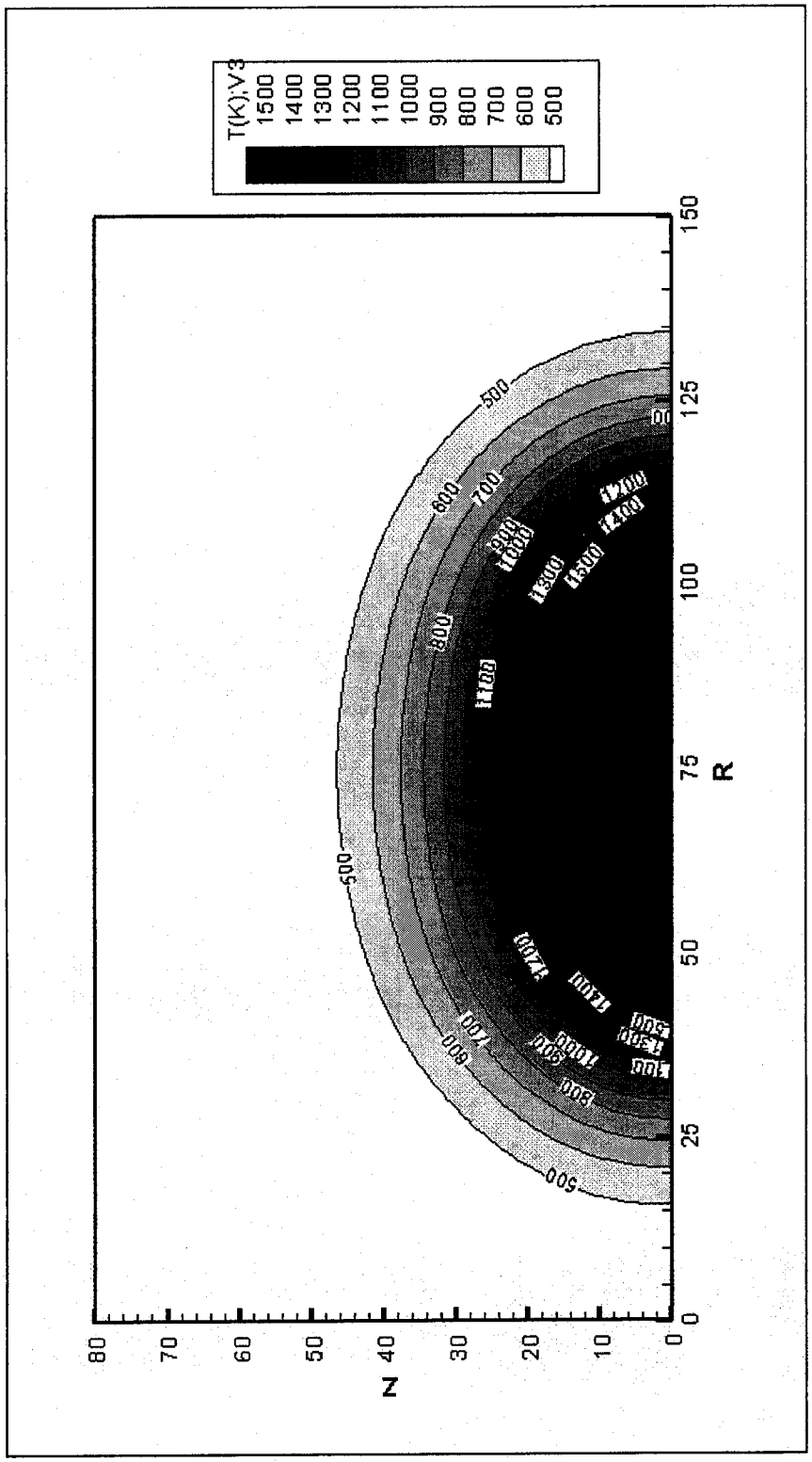

Figure 7.10 Gas temperature distribution (mesh size=0.0005mm, IT=70)

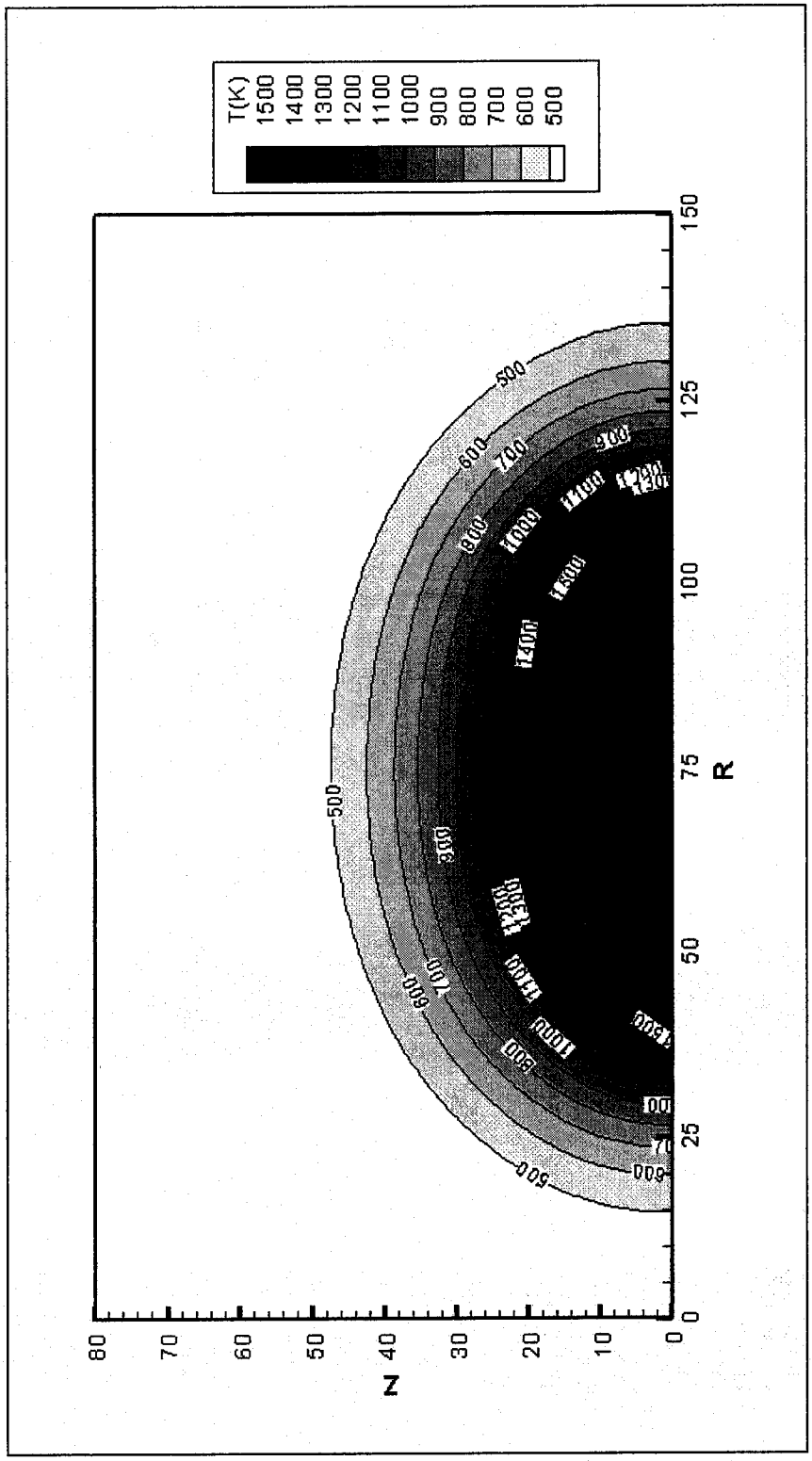

Figure 7.11 Gas temperature distribution mesh size=0.0005mm, IT=100)

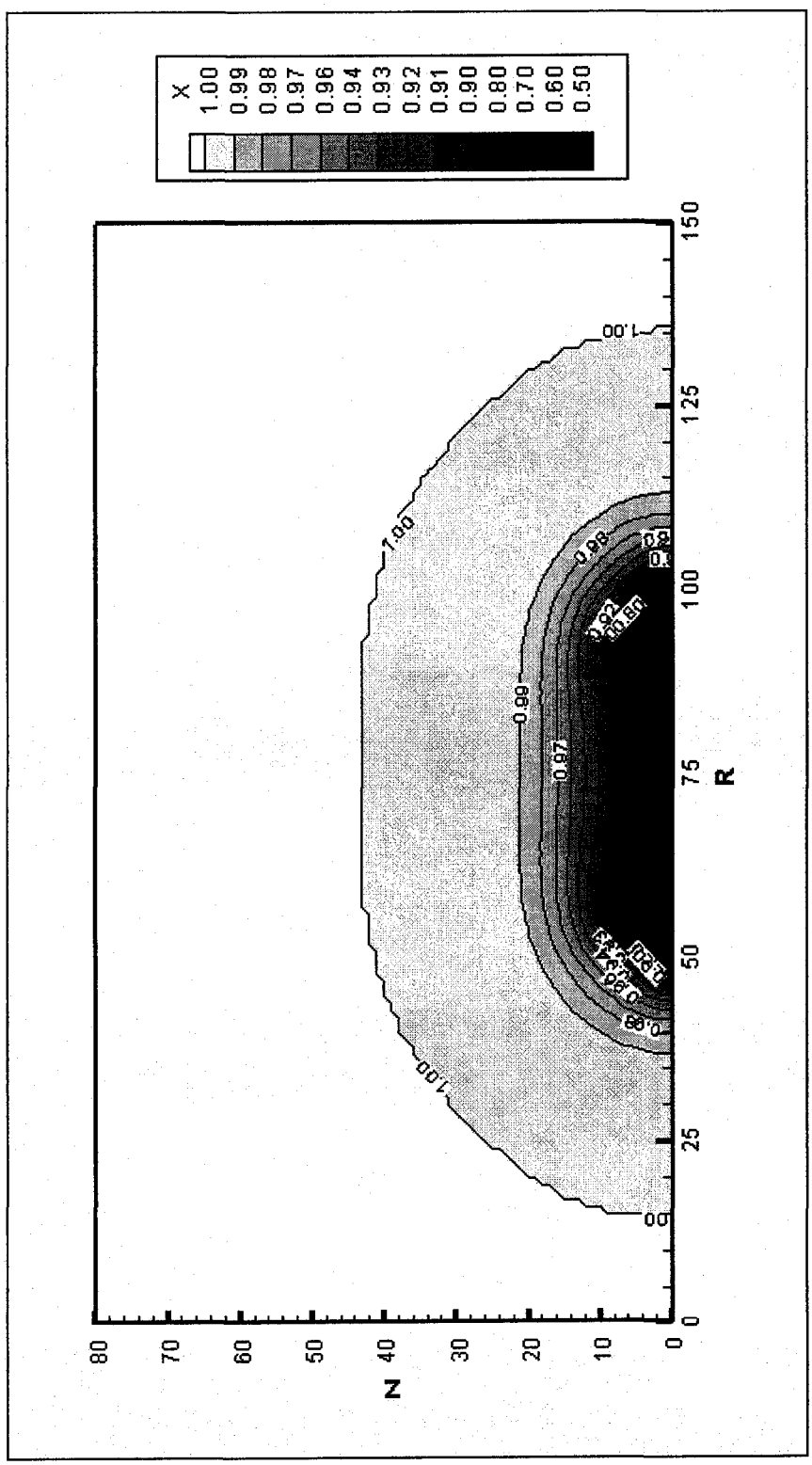

Figure 7.12 Molar ratio X (mesh size=0.0005mm, IT=10)

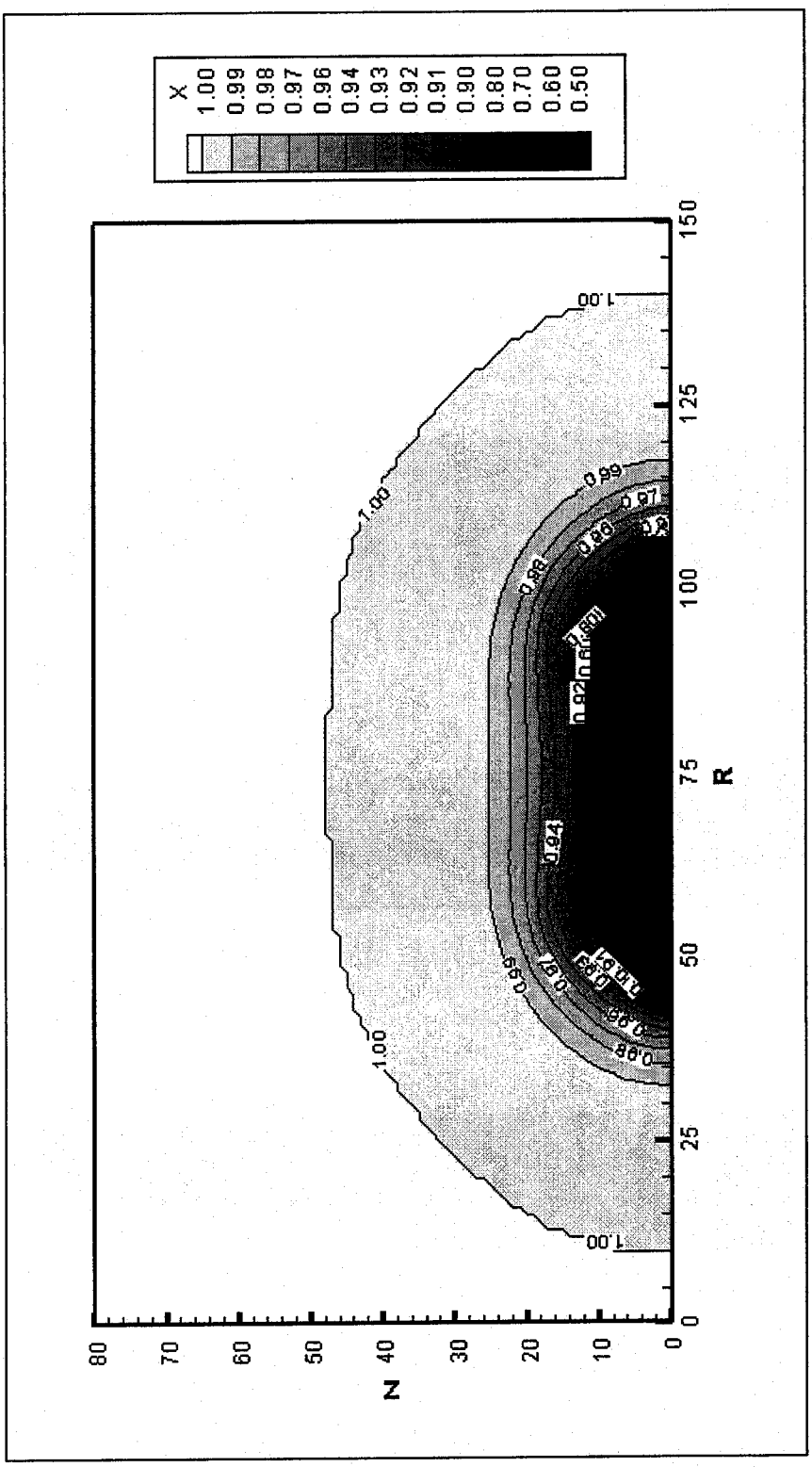

Figure 7.13 Molar ratio X (mesh size=0.0005mm, IT=30)

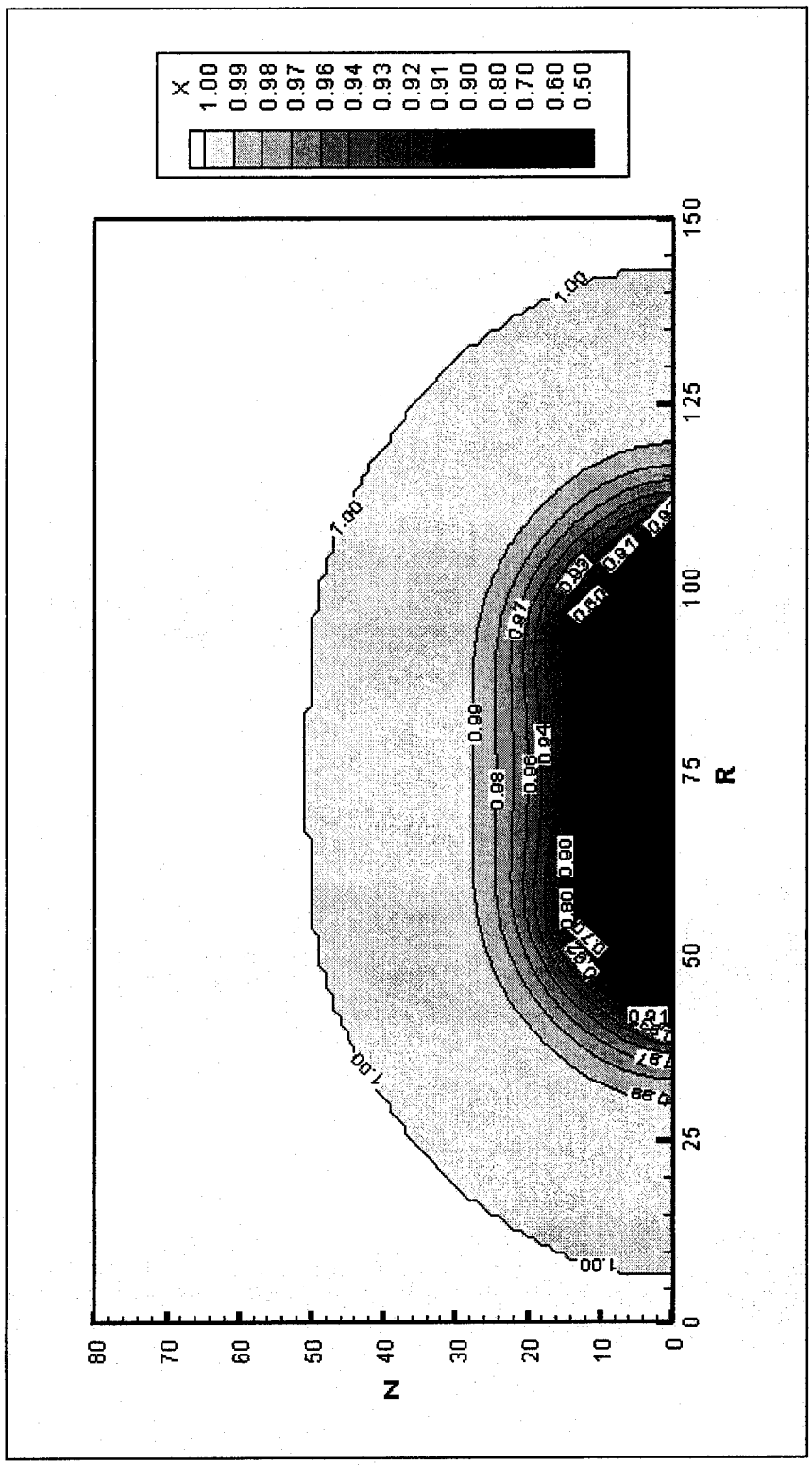

Figure 7.14 Molar ratio X (mesh size=0.0005mm, IT=50)

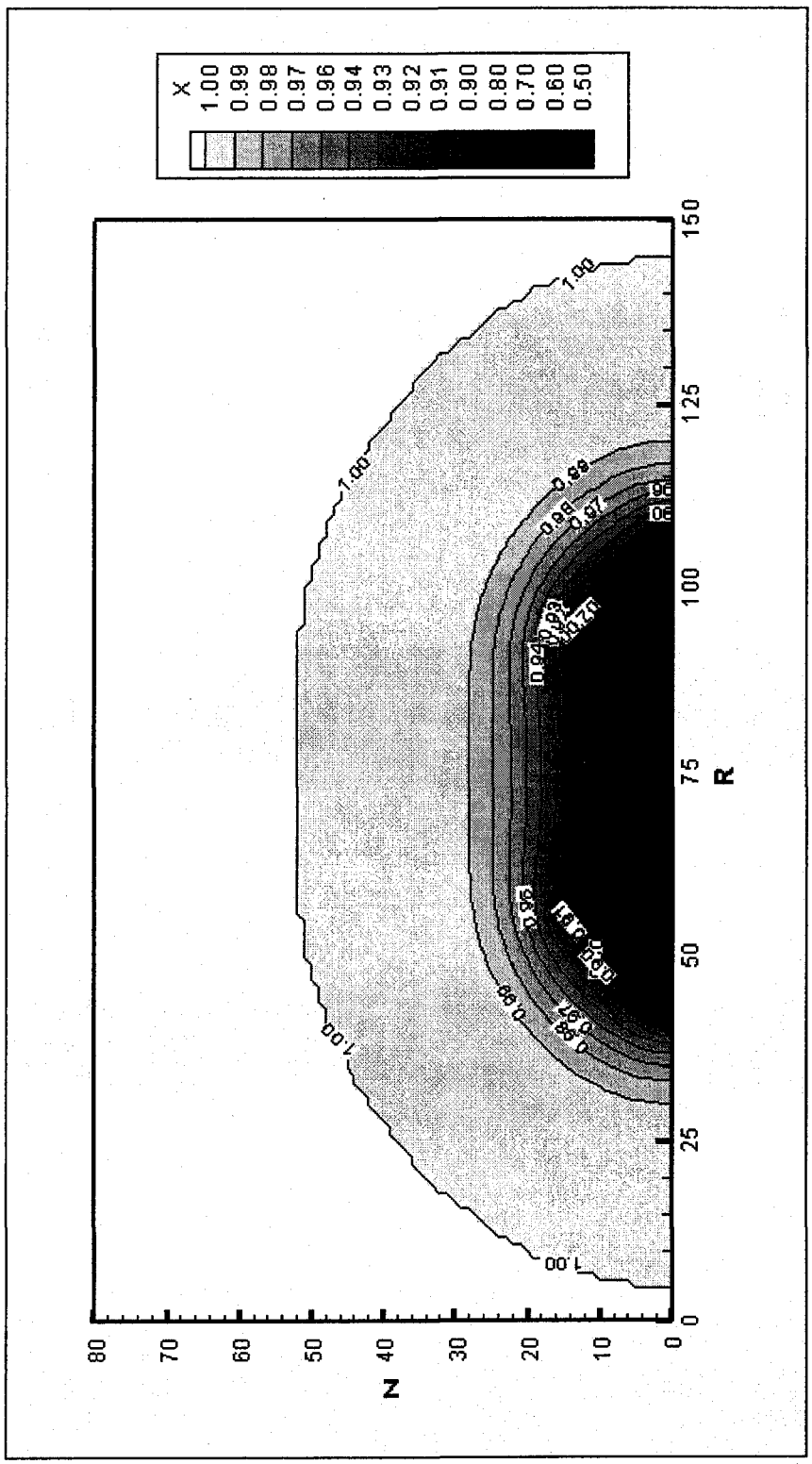

Figure 7.15 Molar ratio X (mesh size=0.0005mm, IT=70)

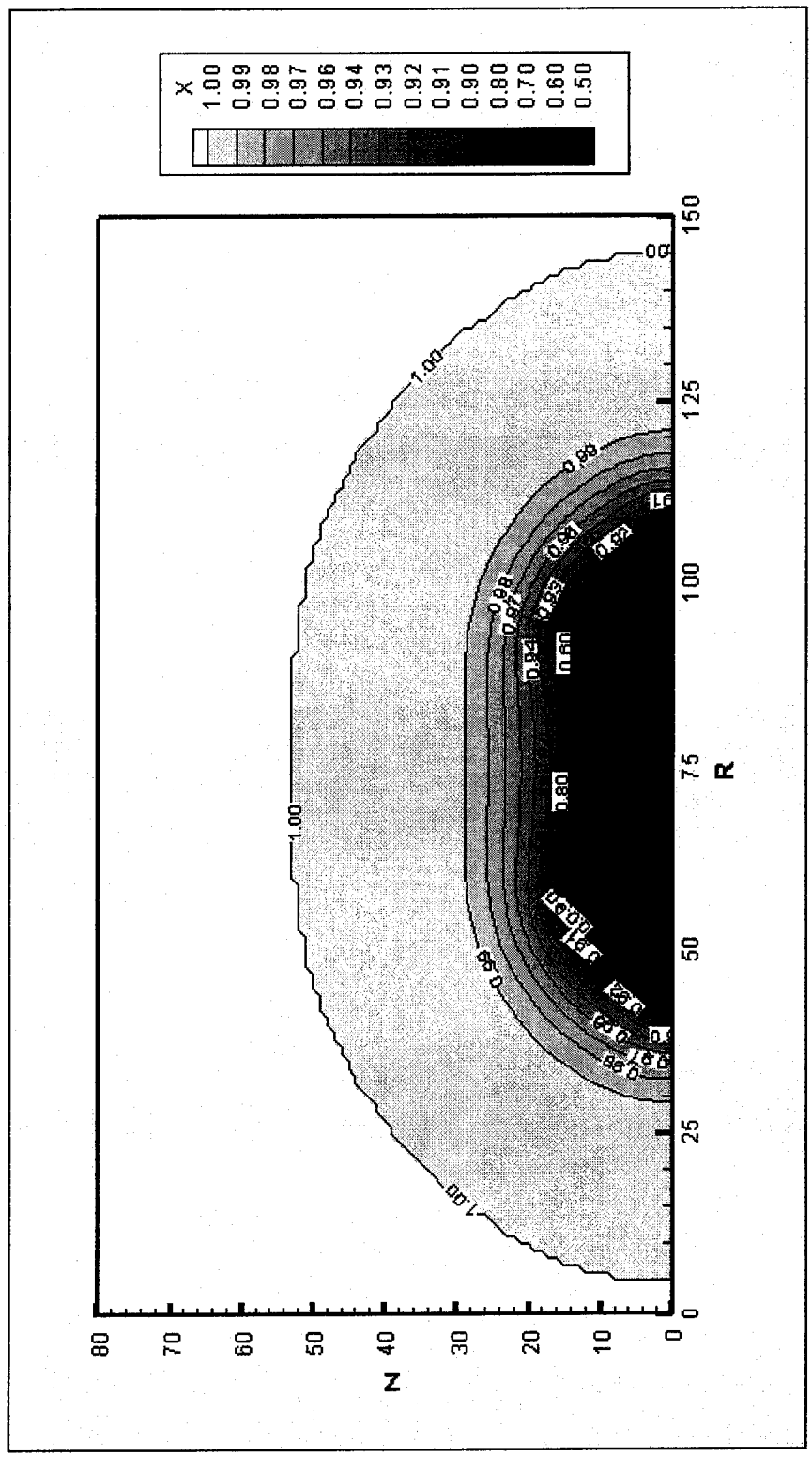

Figure 7.16 Molar ratio X (mesh size=0.0005mm, IT=100)

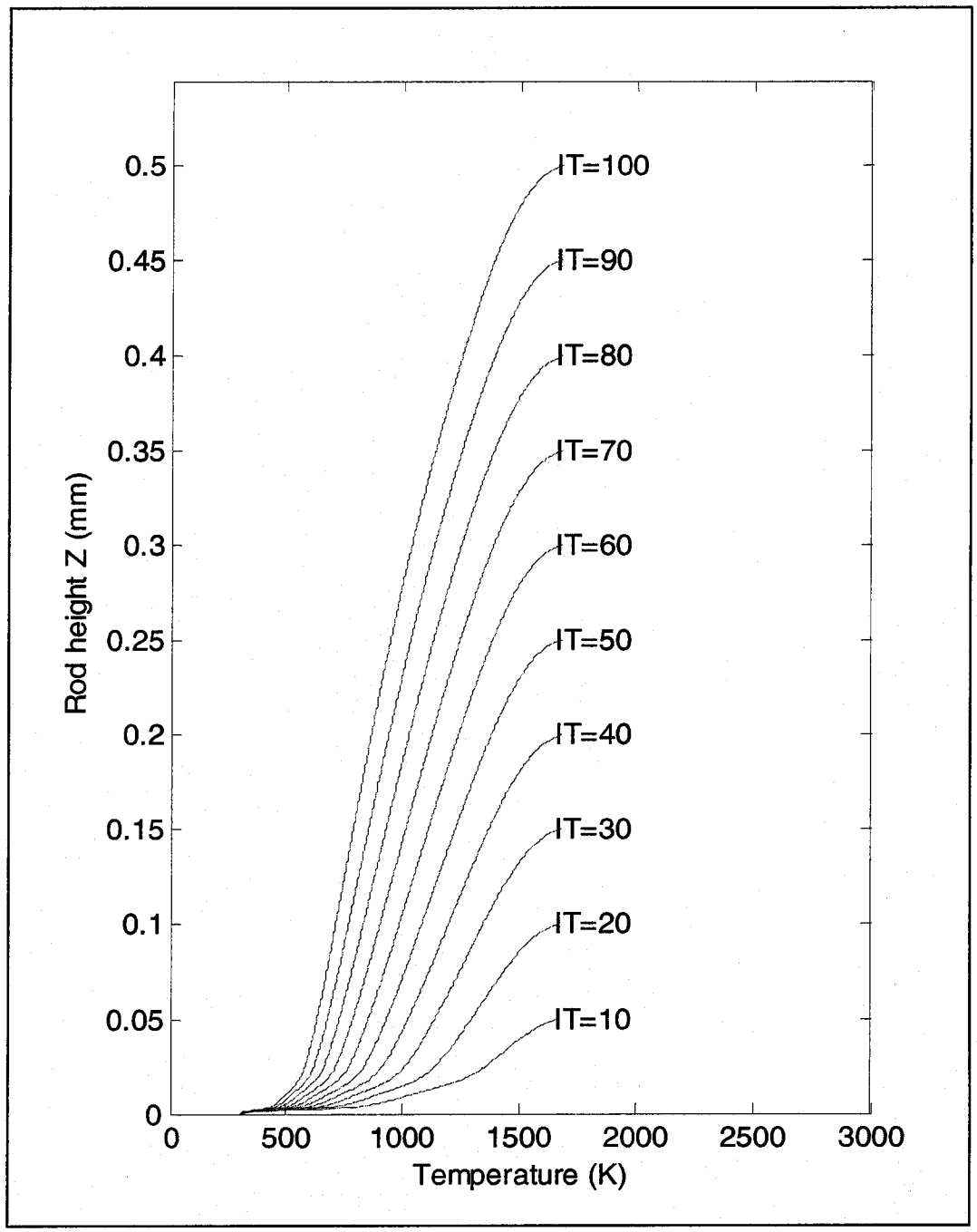

Figure 7.17 Temperature distributions as a function of rod height Z

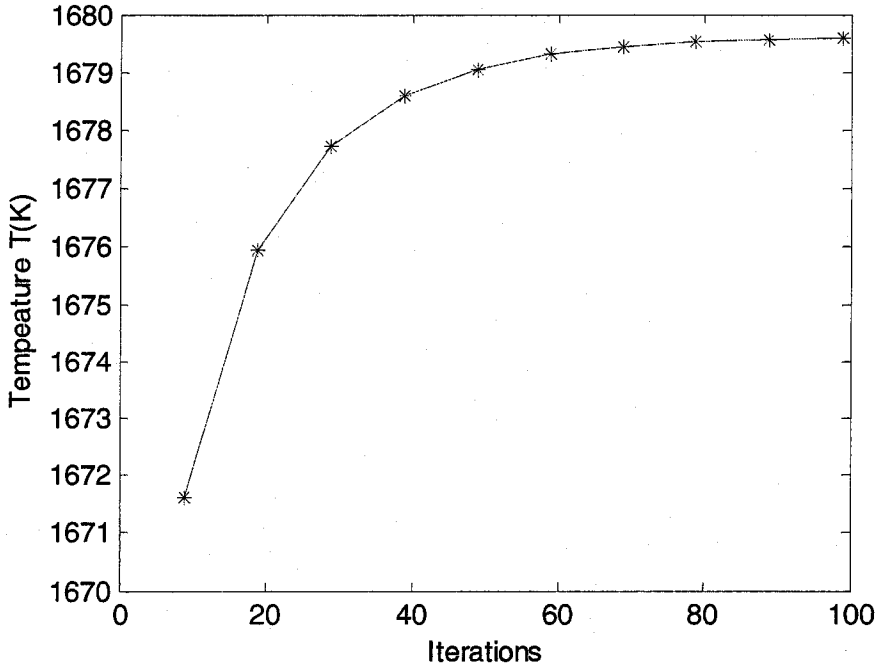

Figure 7.18 Temperature at the tip of the rod corresponding to each iteration

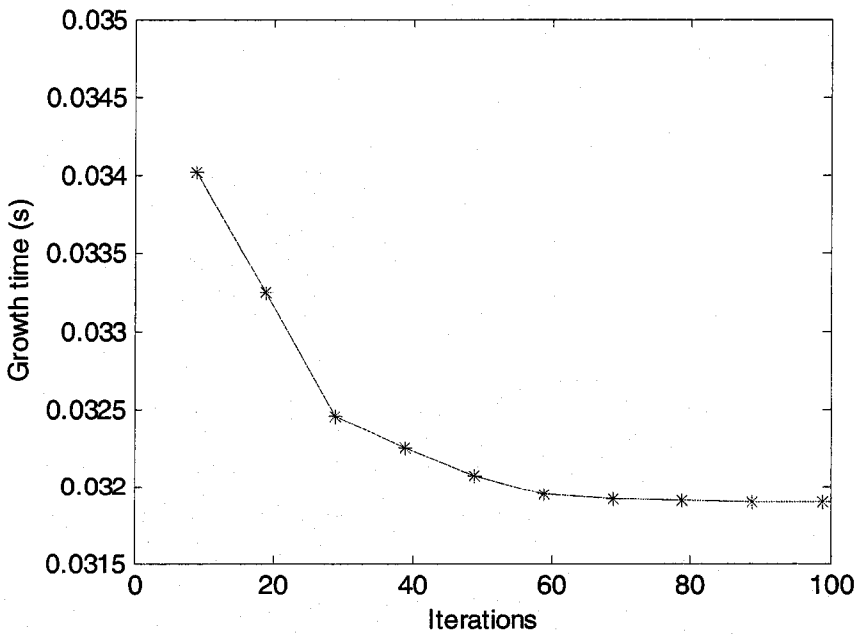

Figure 7.19 Growth time corresponding to each iteration

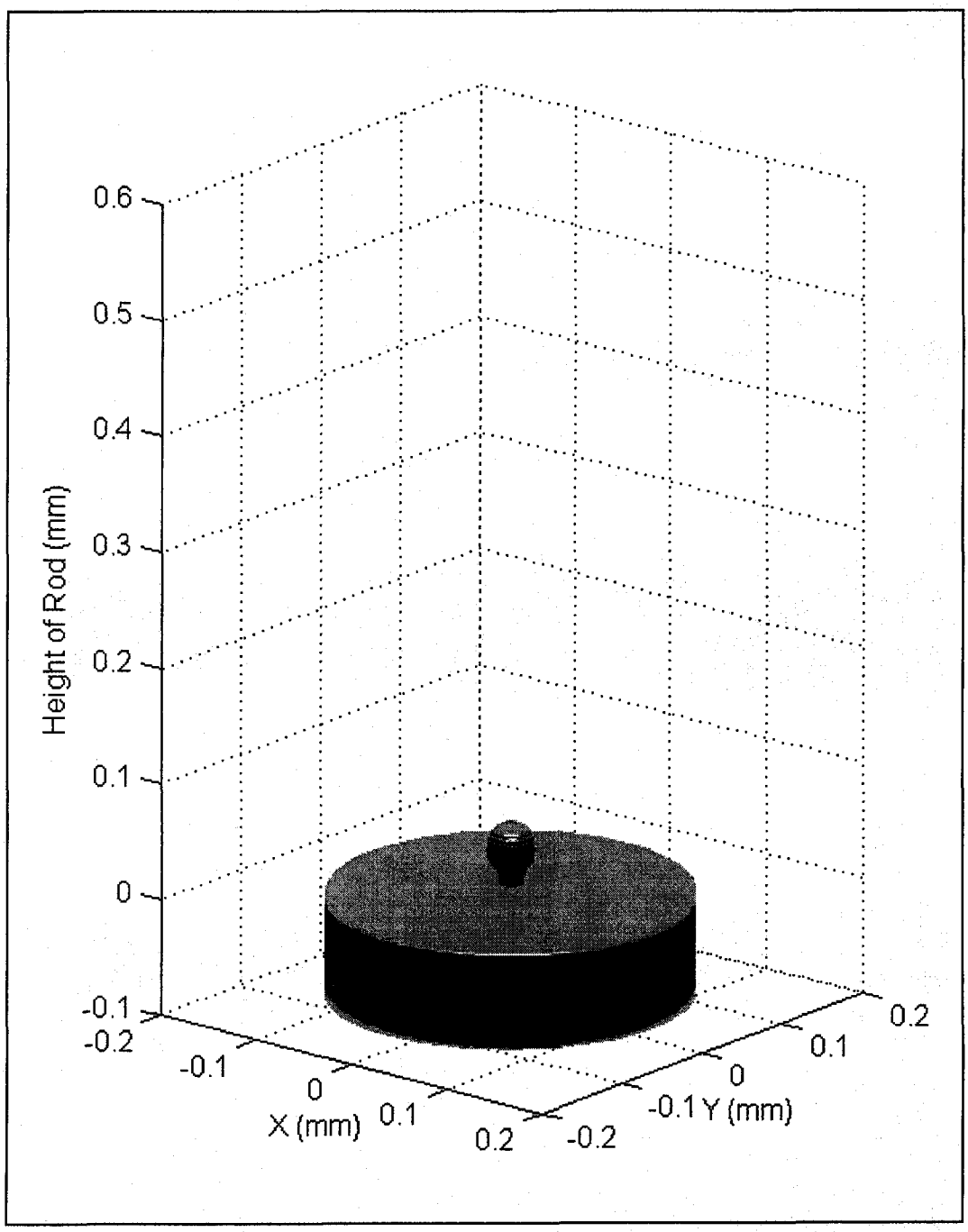

Figure 7.20 Predicted rod growth using the integrated model (Iteration=10)

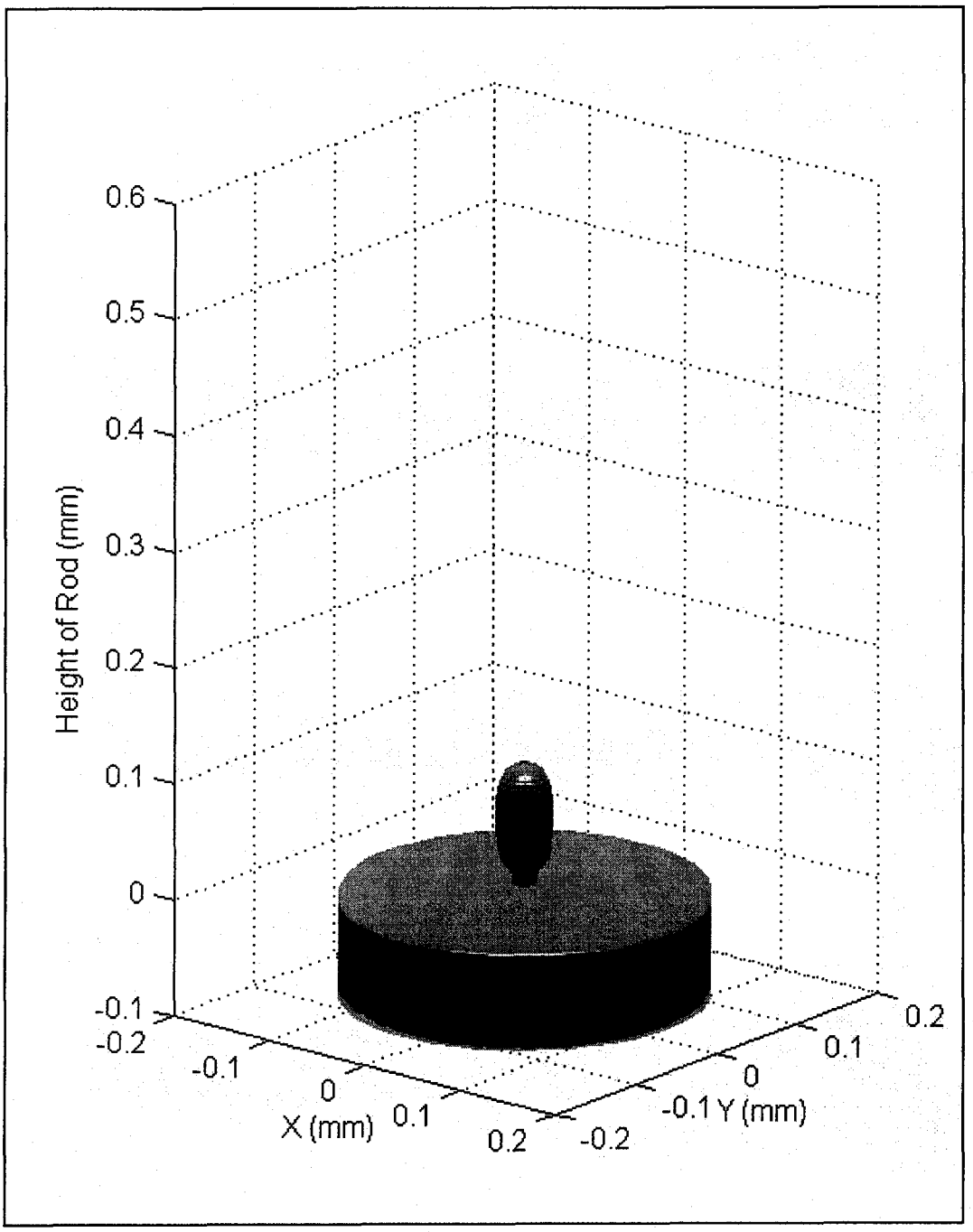

Figure 7.21 Predicted rod growth using the integrated model (Iteration=20)

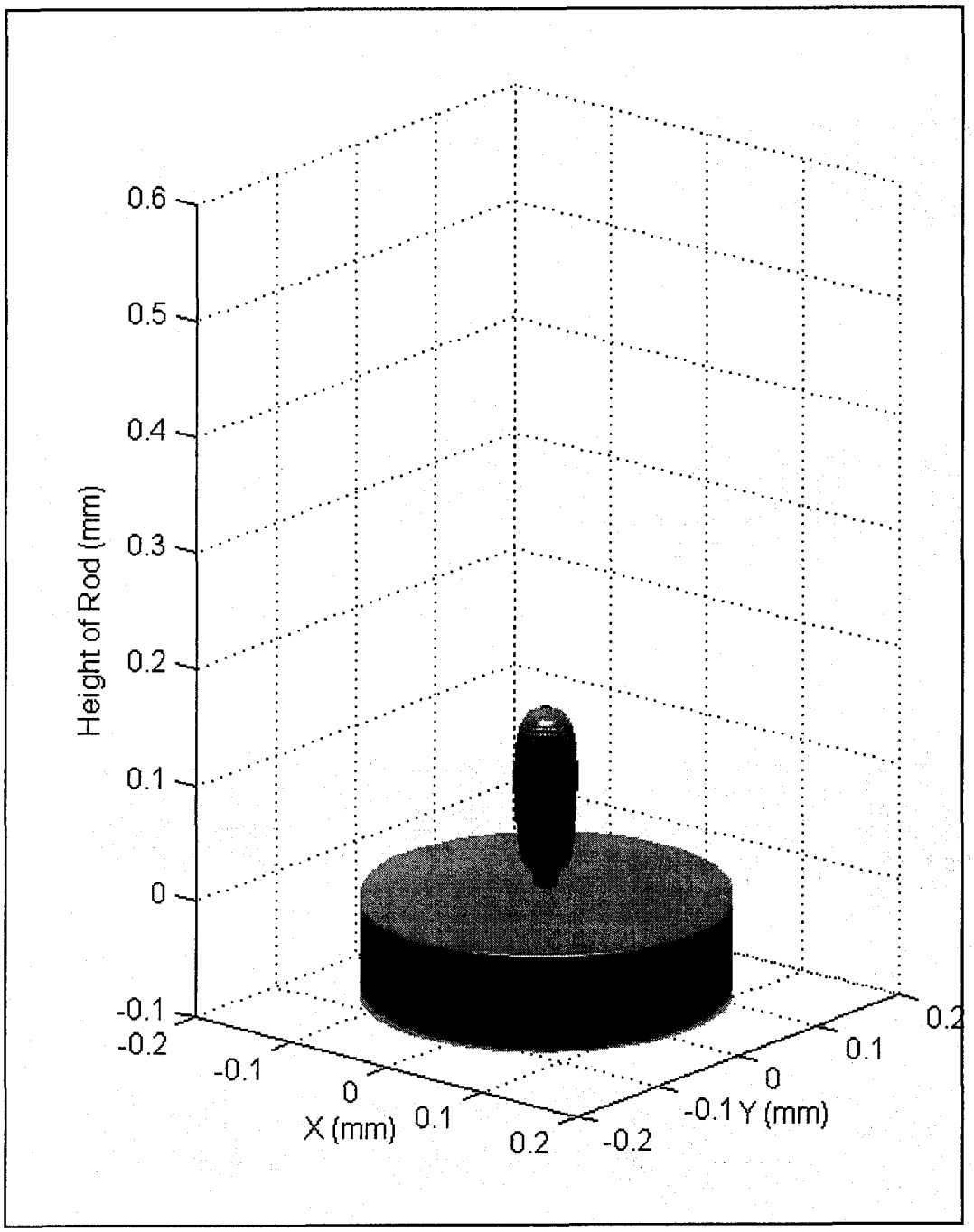

Figure 7.22 Predicted rod growth using the integrated model (Iteration=30)

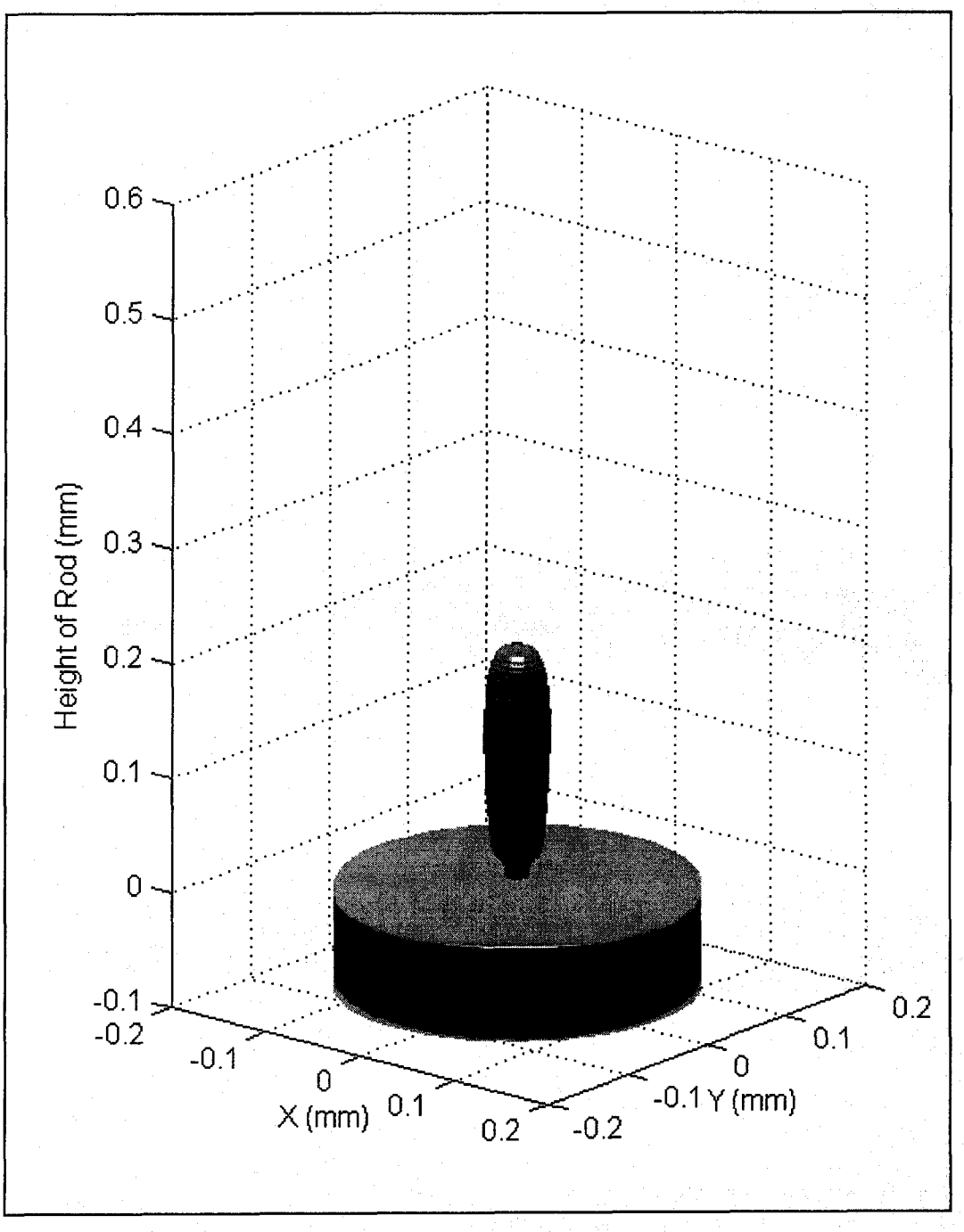

Figure 7.23 Predicted rod growth using the integrated model (Iteration=40)

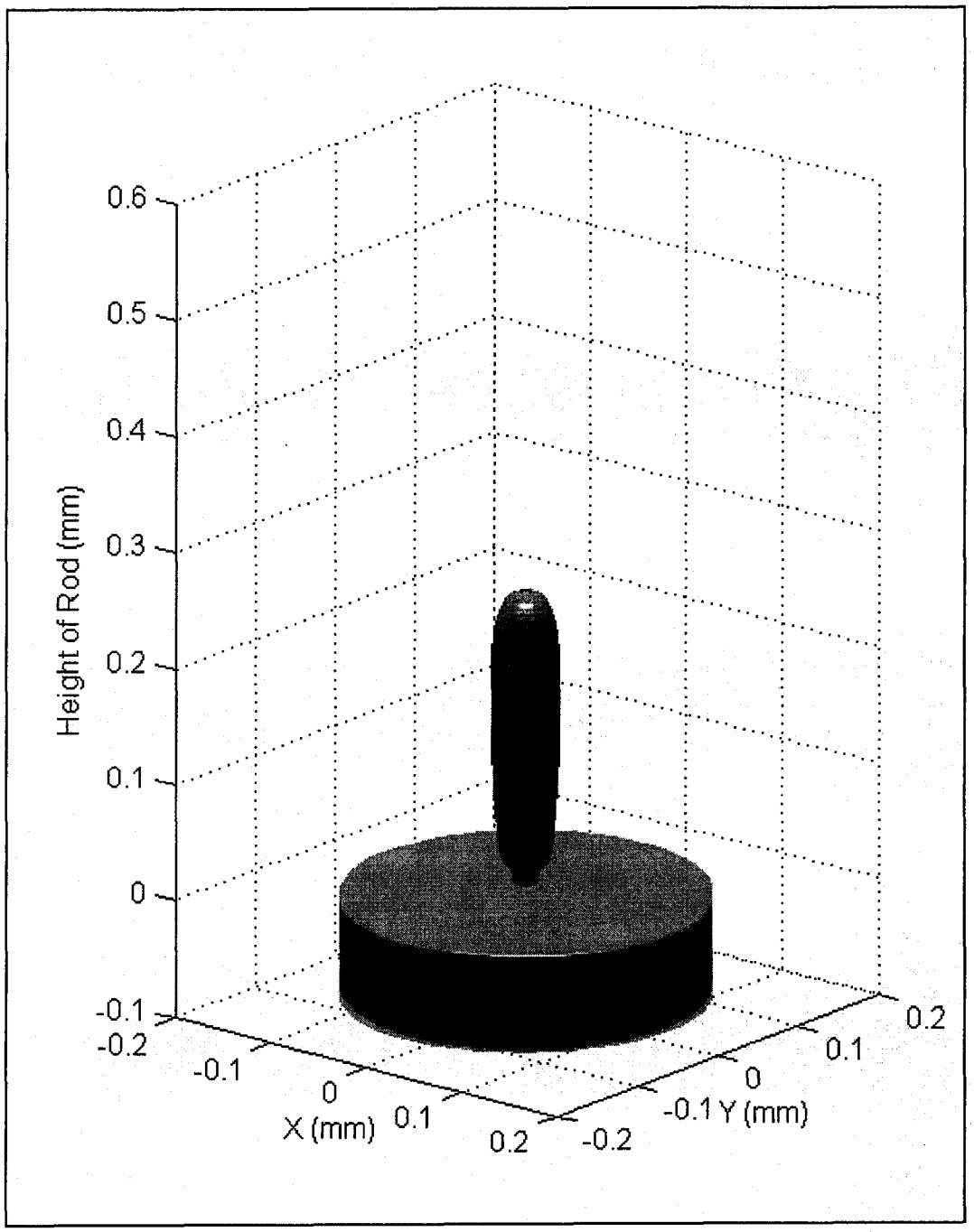

Figure 7.24 Predicted rod growth using the integrated model (Iteration=50)

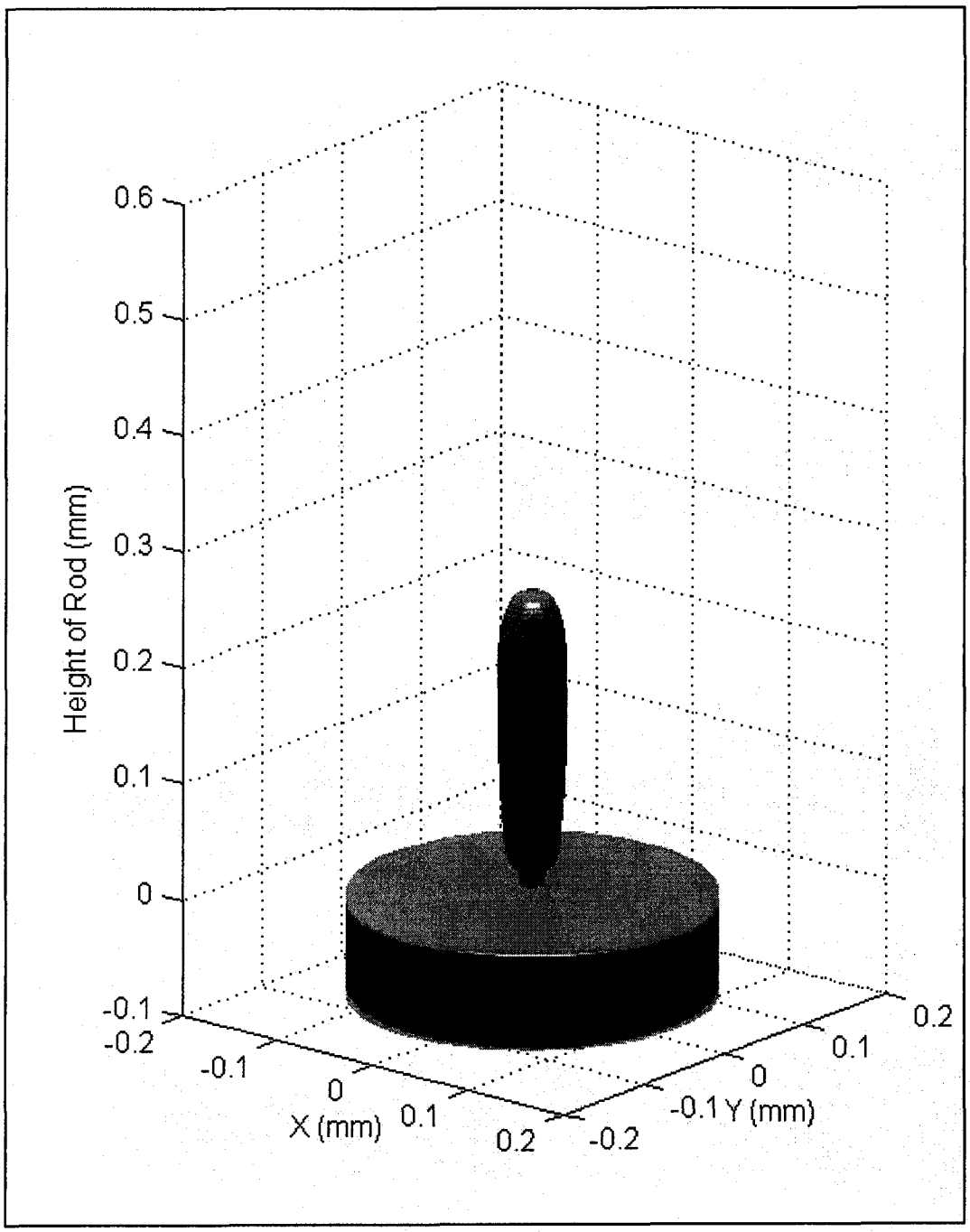

Figure 7.25 Predicted rod growth using the integrated model (Iteration=60)

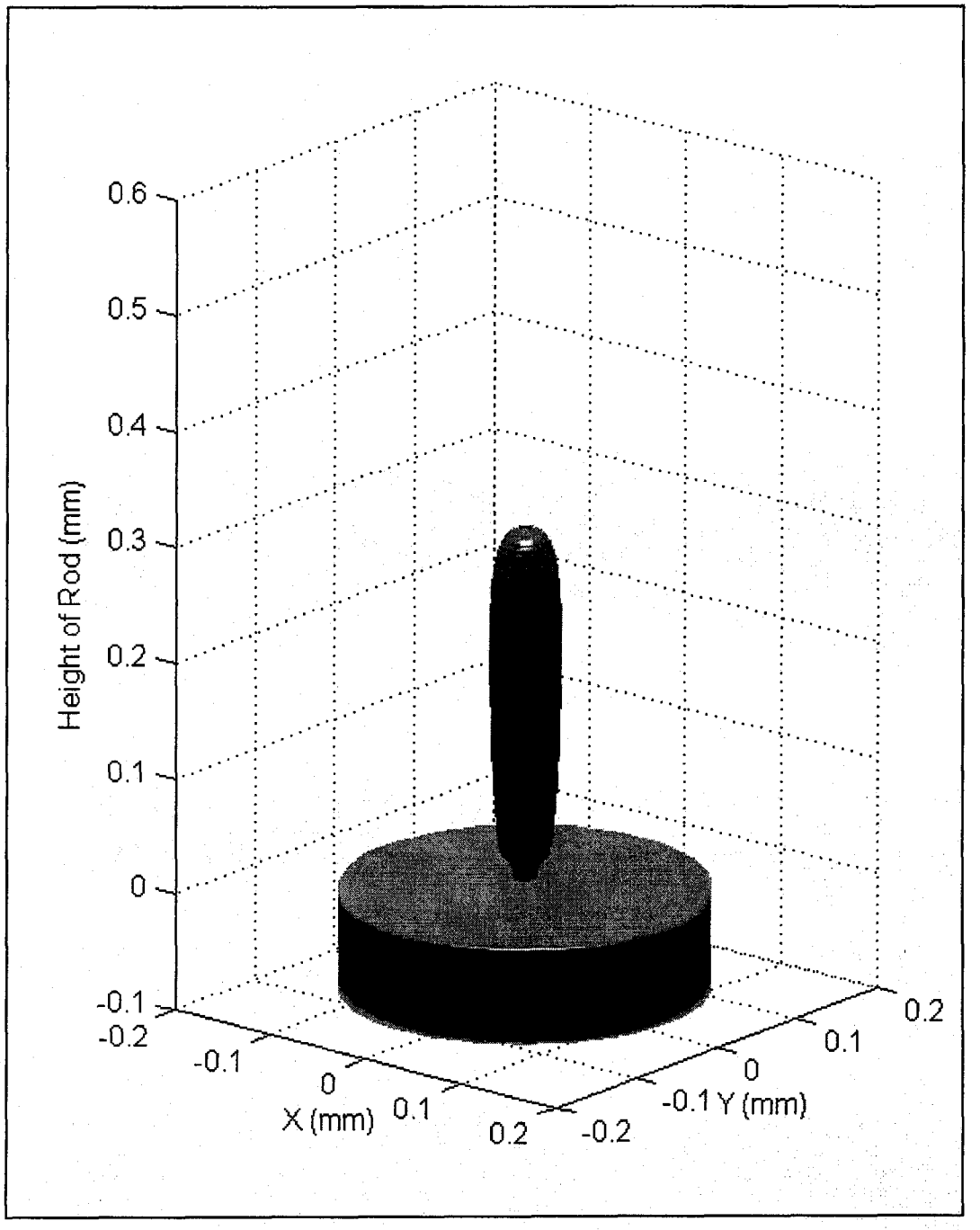

Figure 7.26 Predicted rod growth using the integrated model (Iteration=70)

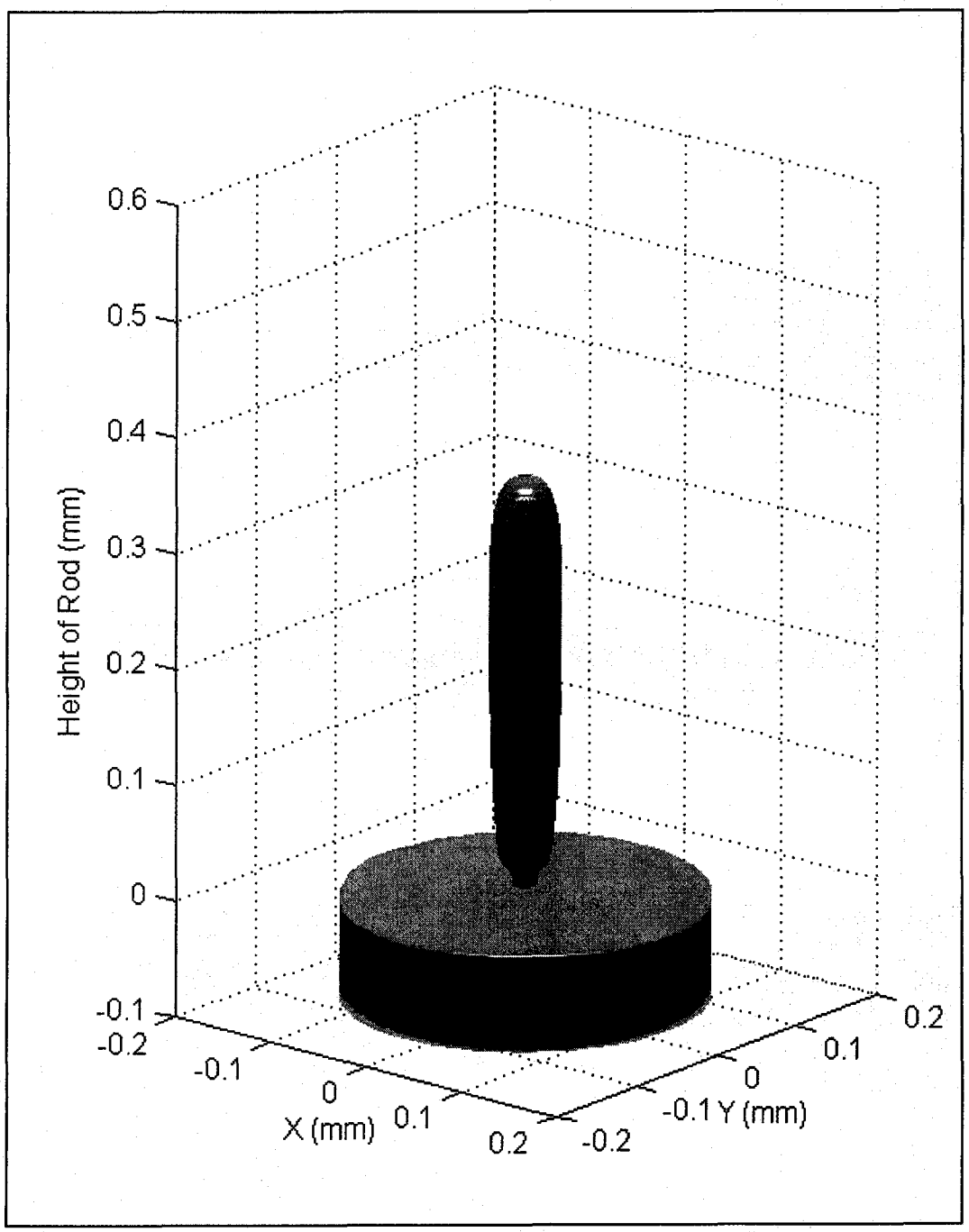

Figure 7.27 Predicted rod growth using the integrated model (Iteration=80)

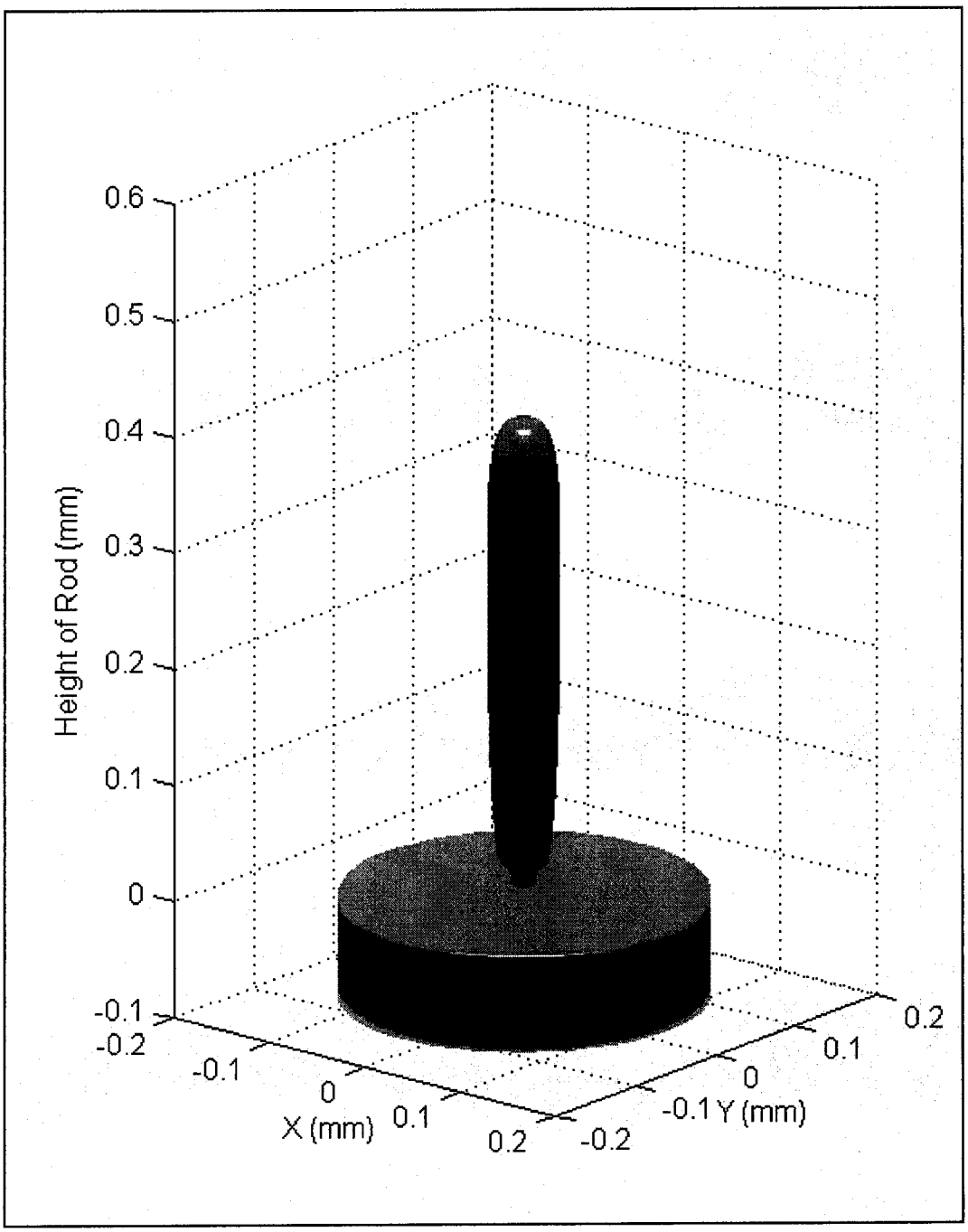

Figure 7.28 Predicted rod growth using the integrated model (Iteration=90)

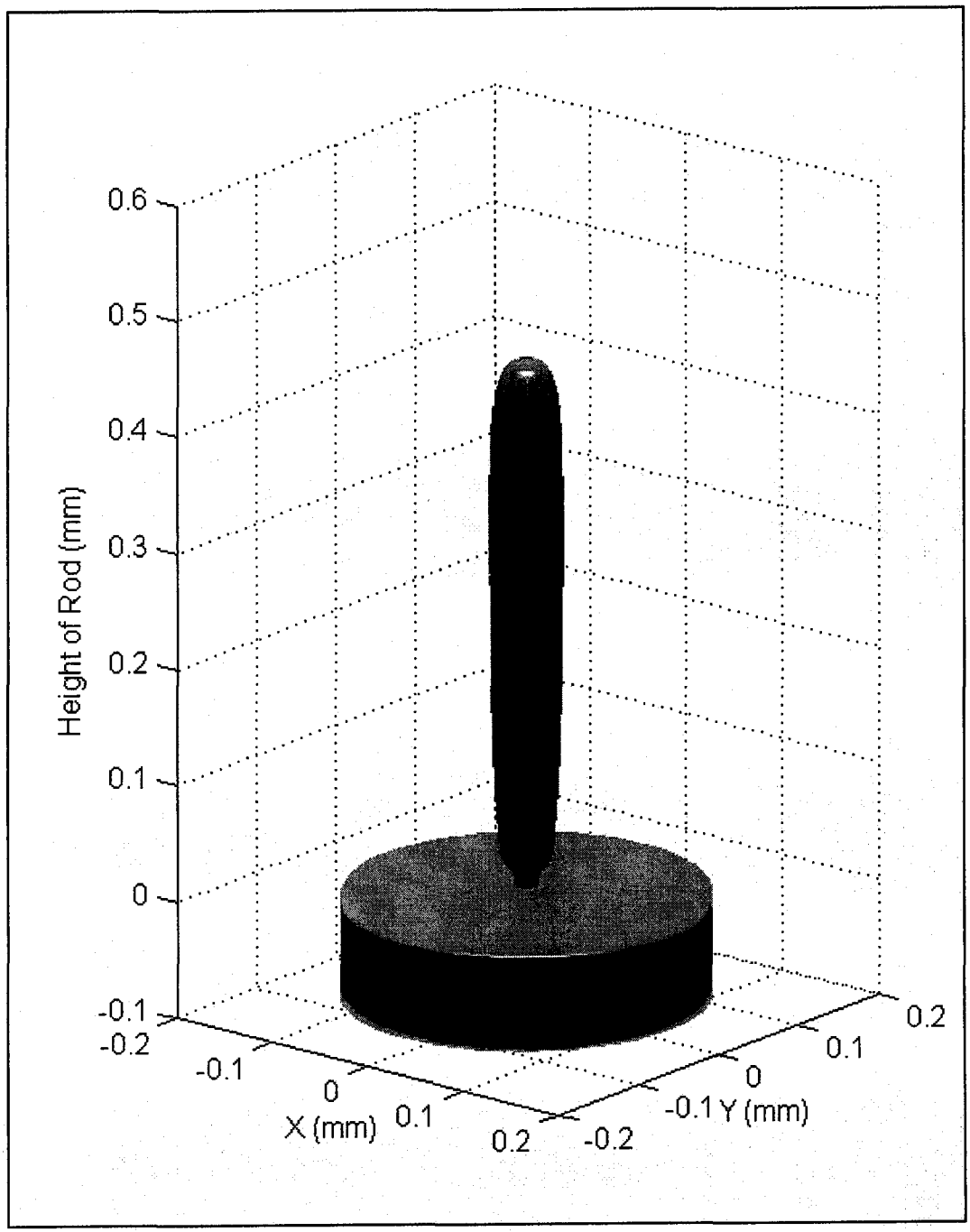

Figure 7.29 Predicted rod growth using the integrated model (Iteration=100)

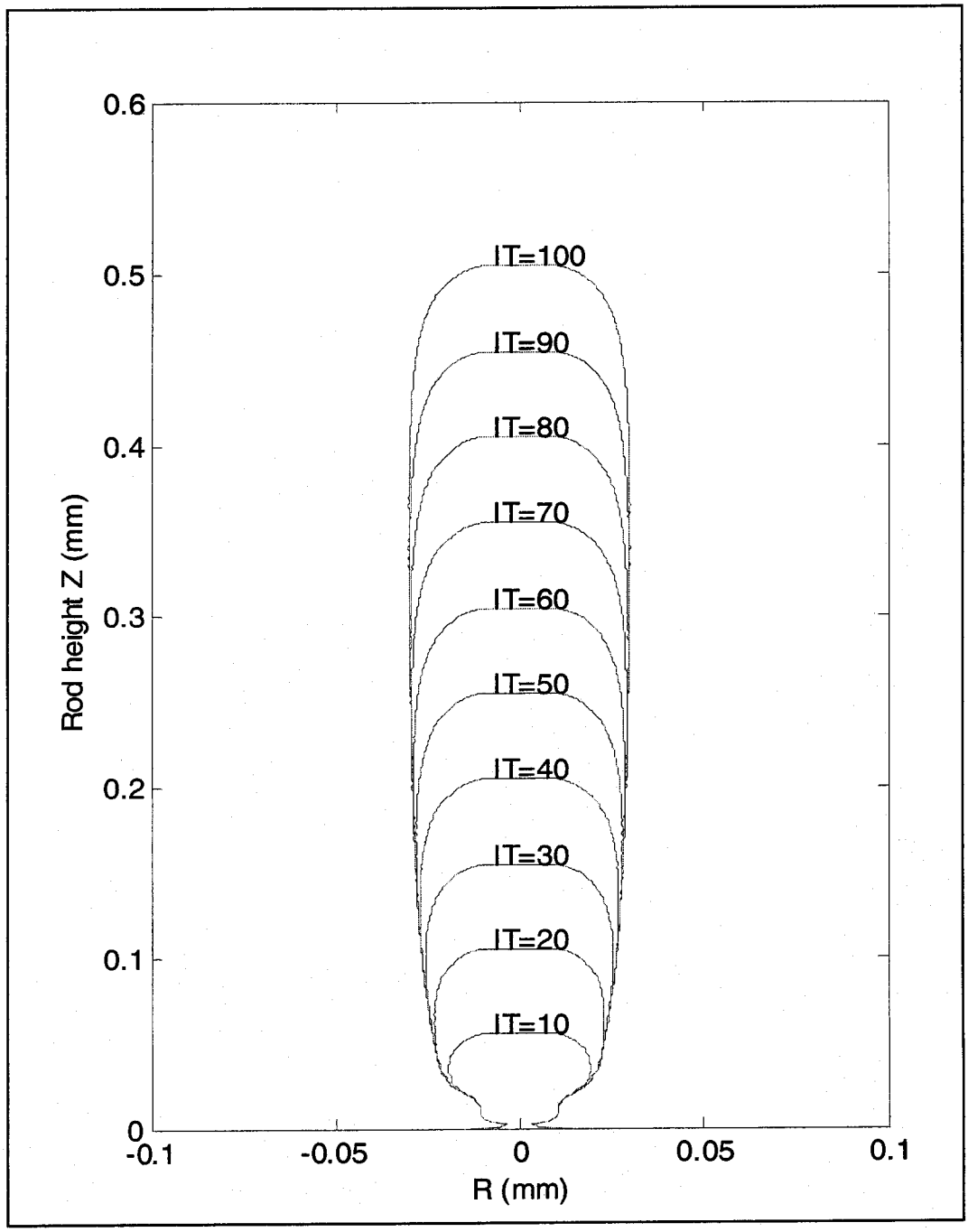

Figure 7.30 Rod shapes with respect to different iterations (IT) or deposition stages

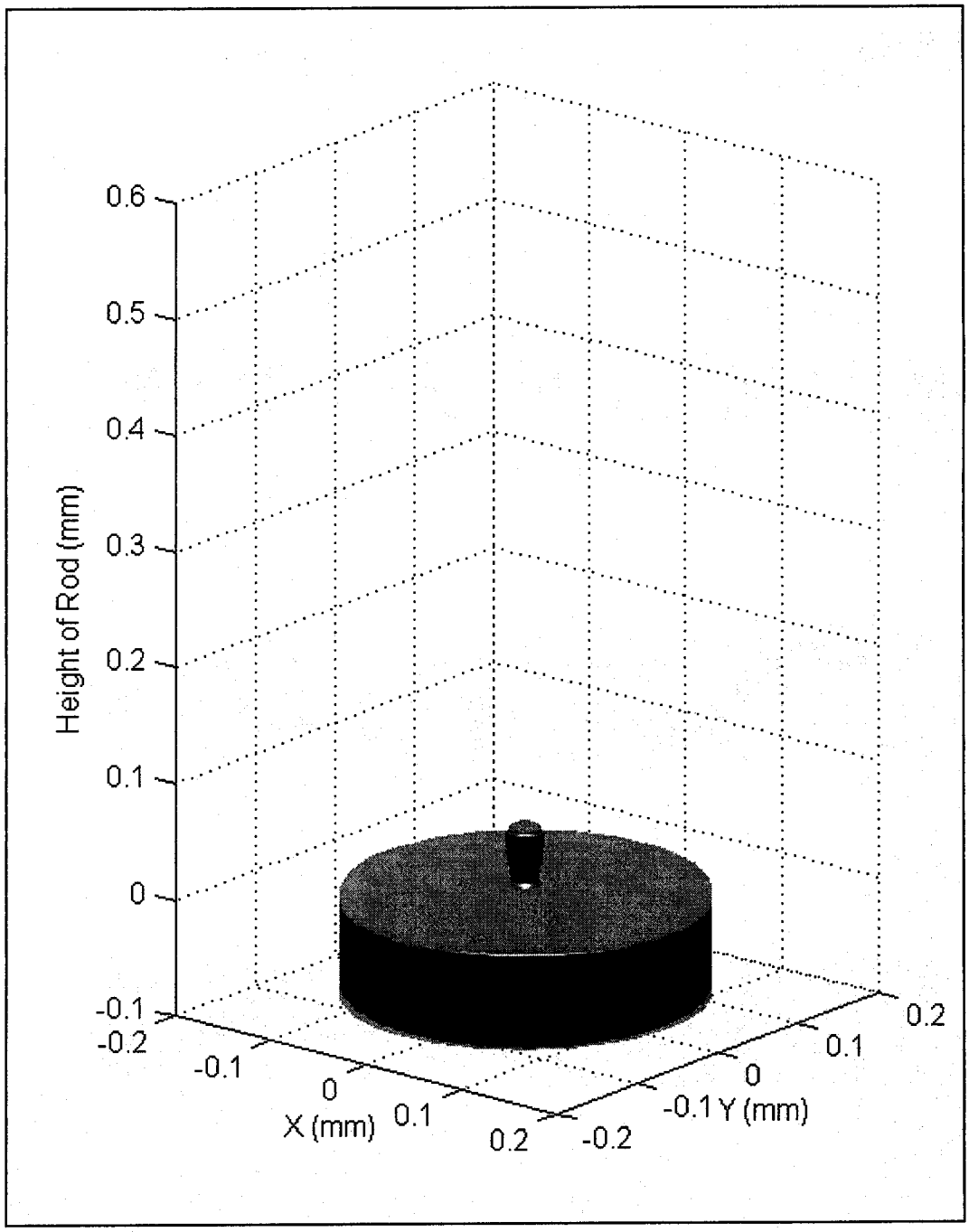

Figure 7.31 Predicted rod growth with guessed initial growth (Iteration=10)

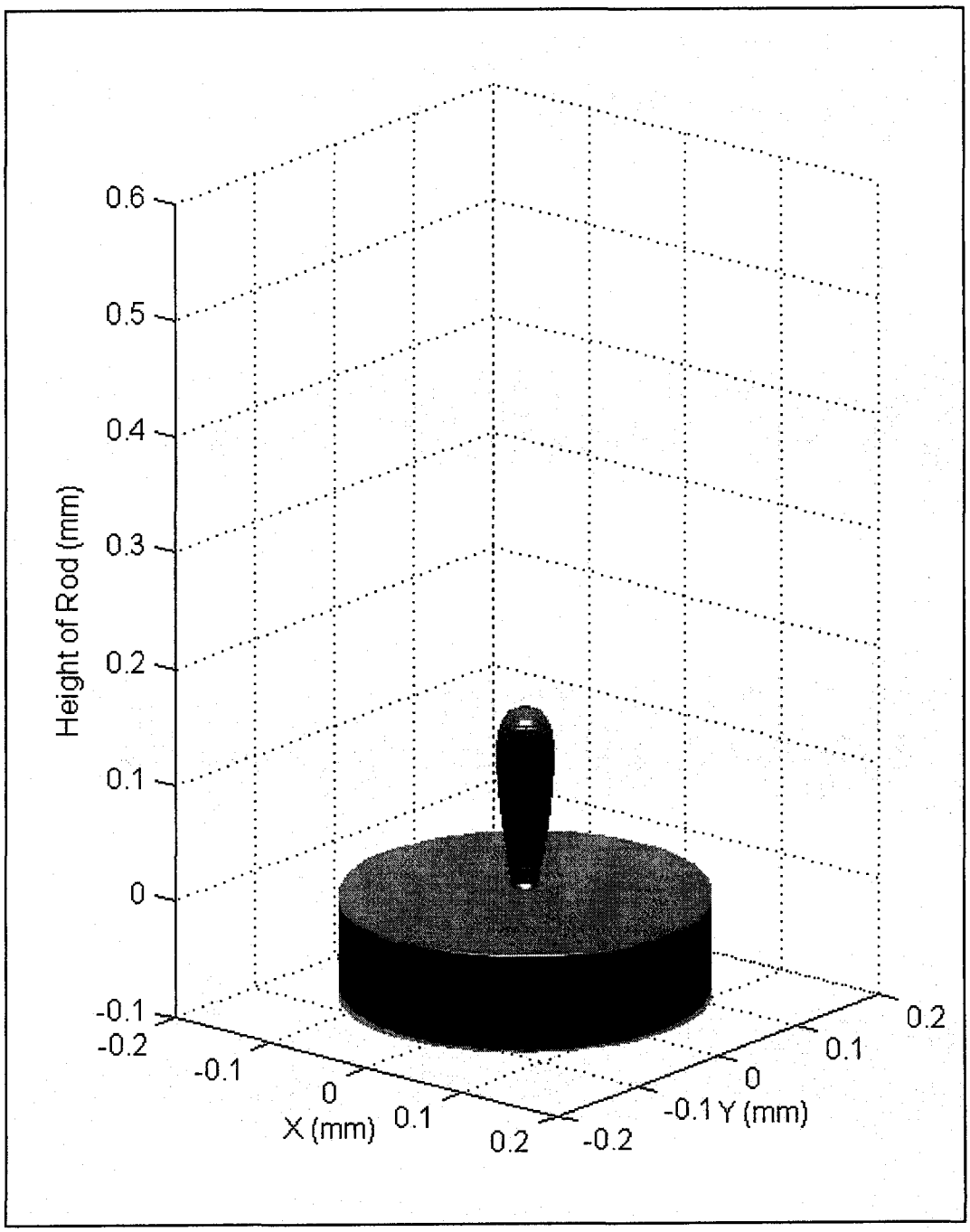

Figure 7.32 Predicted rod growth with guessed initial growth (Iteration=30)

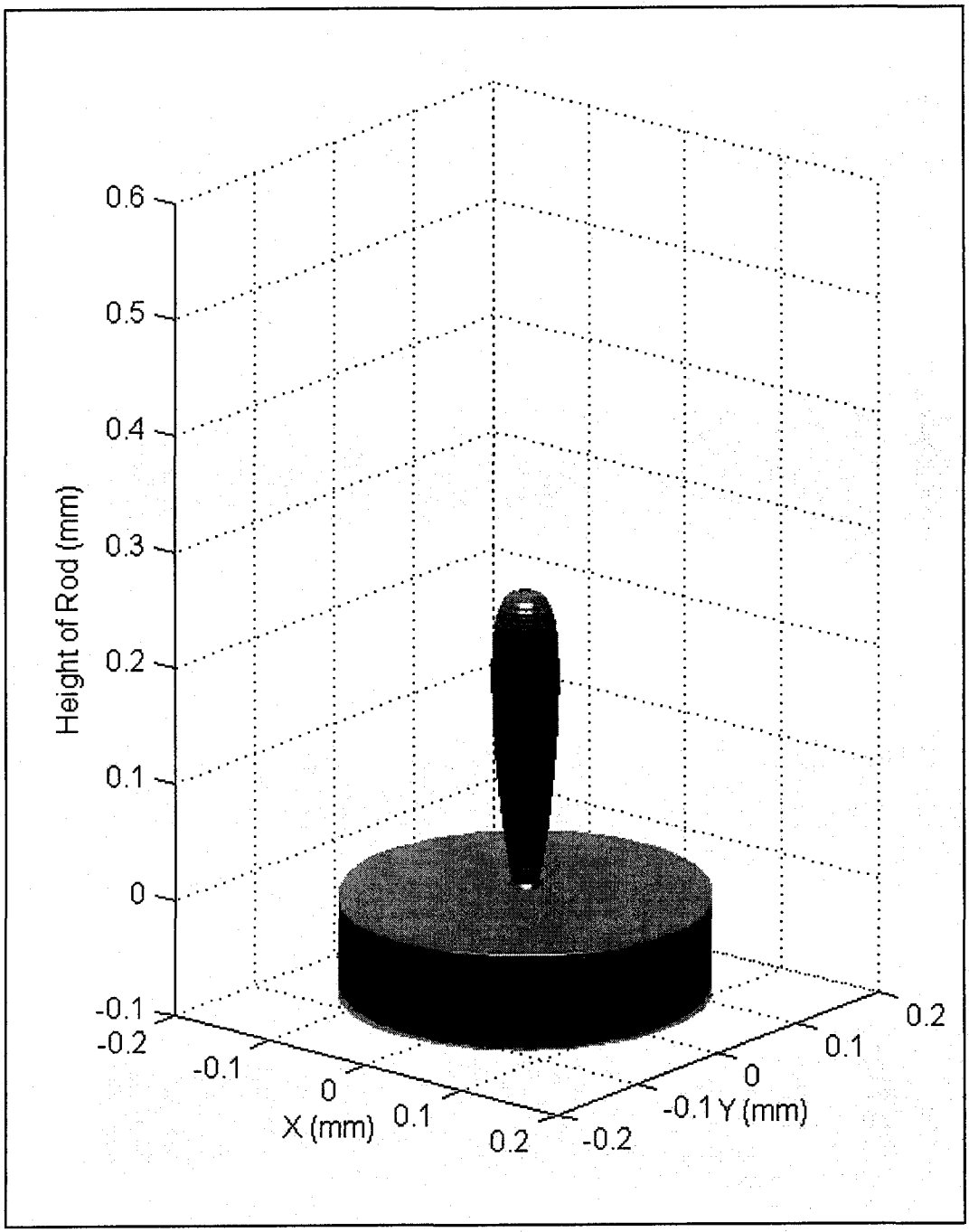

Figure 7.33 Predicted rod growth with guessed initial growth (Iteration=50)

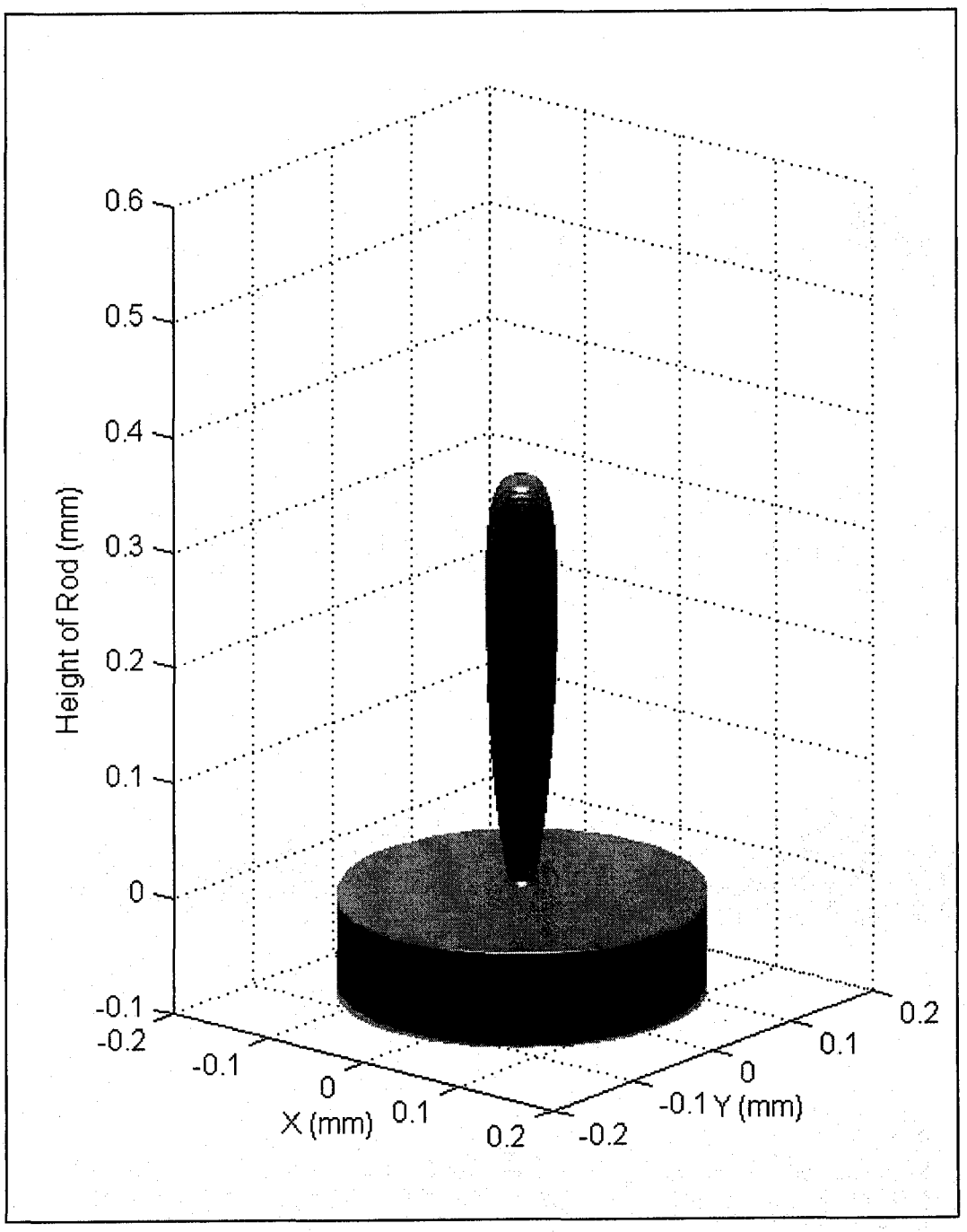

Figure 7.34 Predicted rod growth with guessed initial growth (Iteration=70)

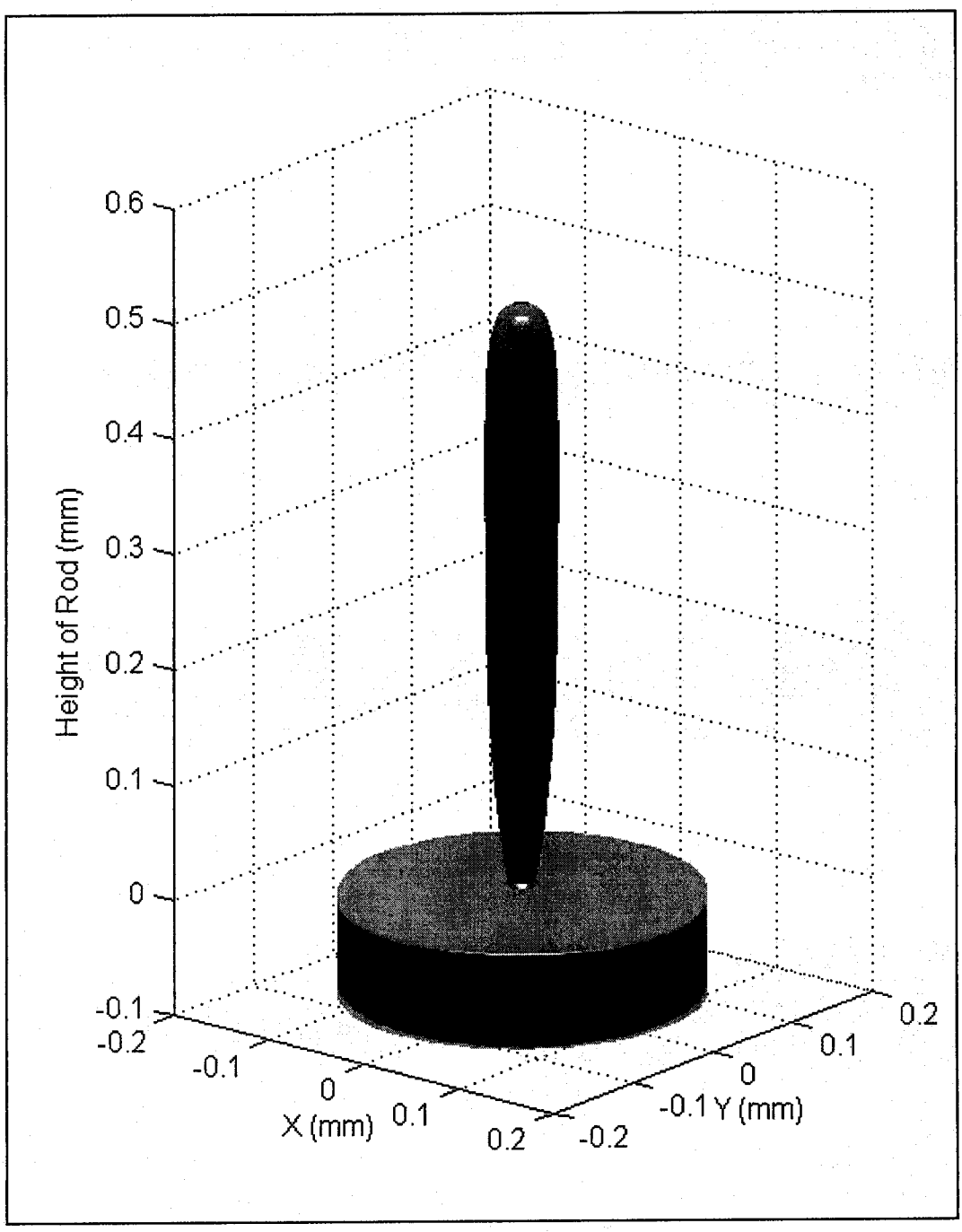

Figure 7.35 Predicted rod growth with guessed initial growth (Iteration=100)

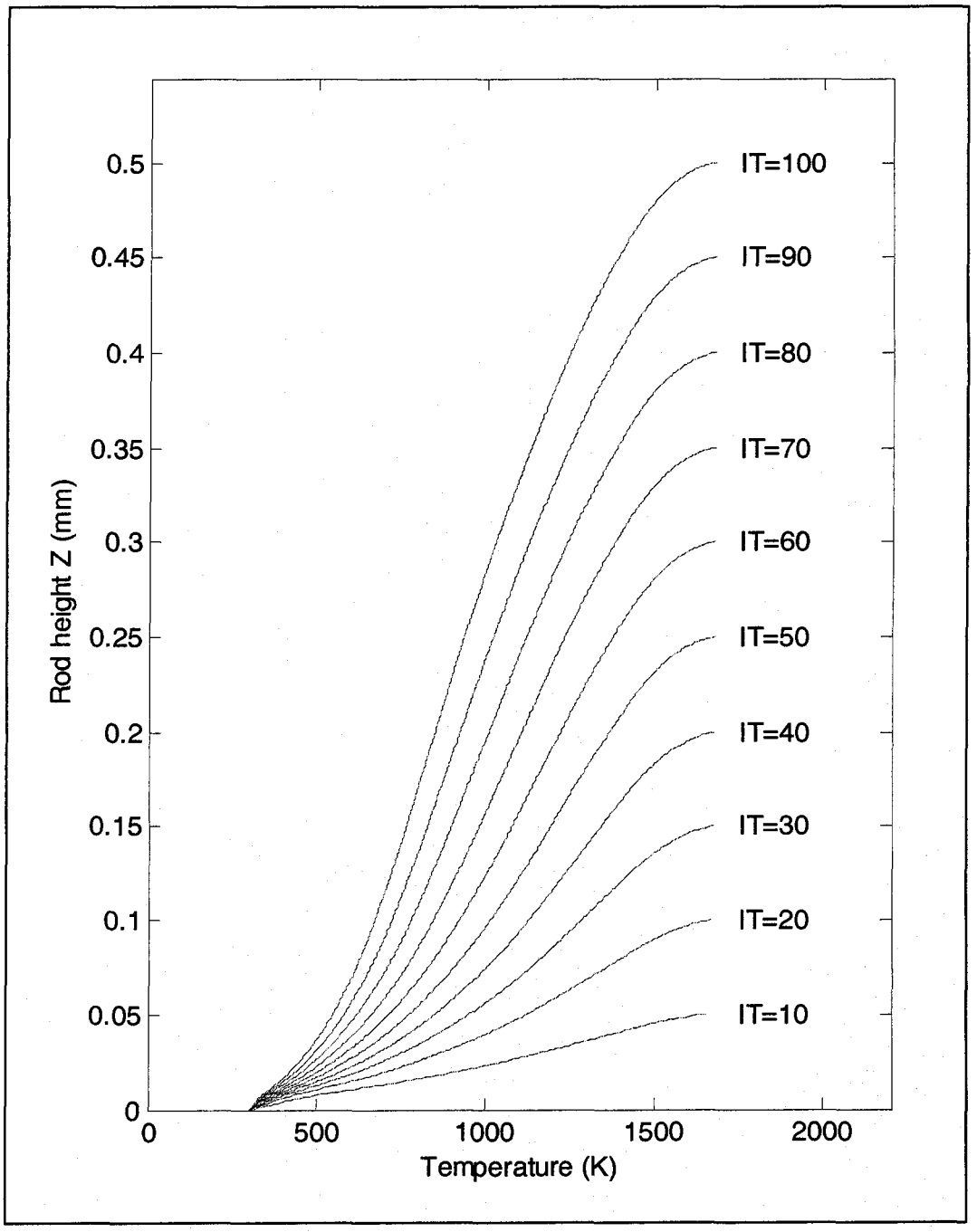

Figure 7.36 Temperature distributions as a function of rod height Z

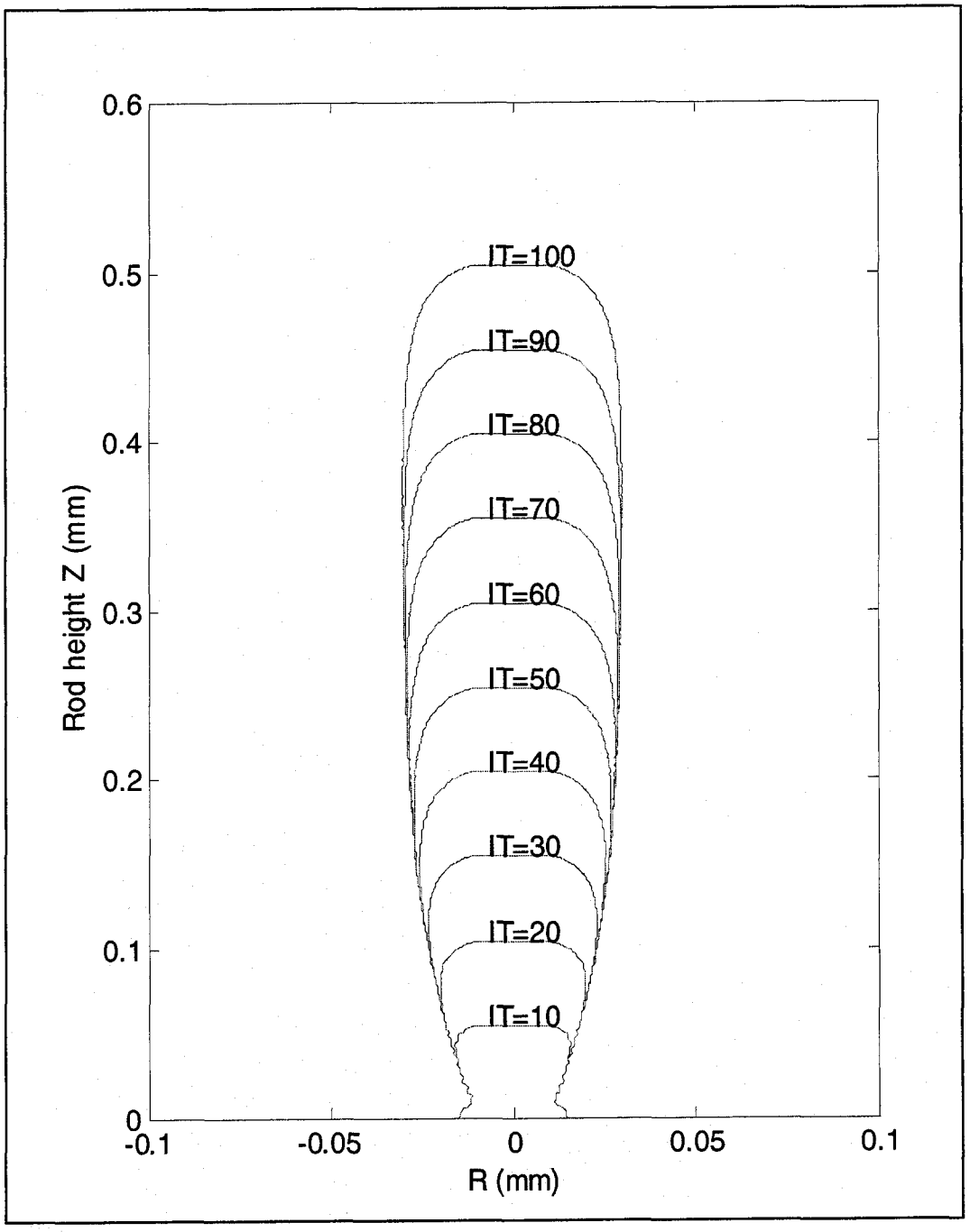

Figure 7.37 Rod shapes with respect to different iterations (IT) or deposition stages

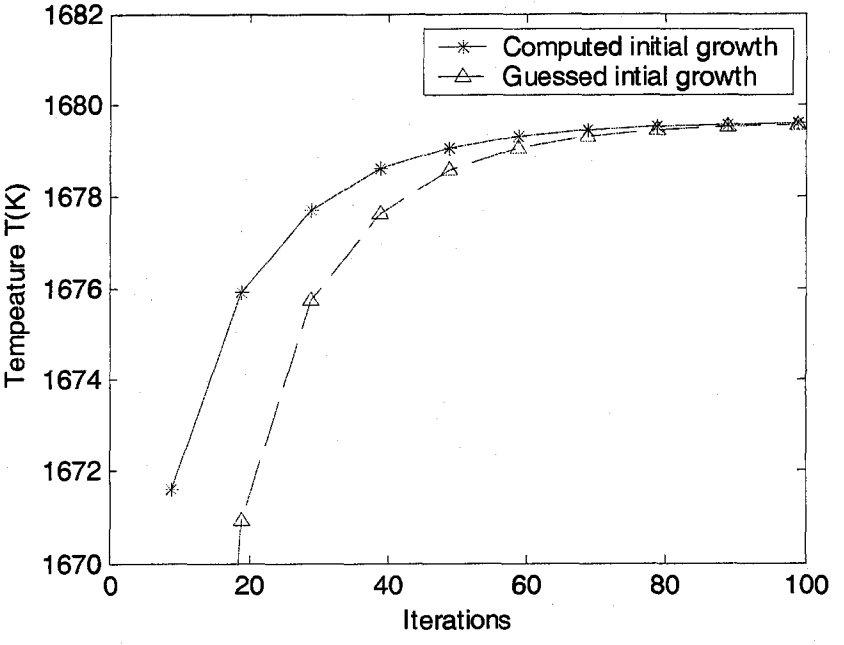

Figure 7.38 Temperature at the tip of the rod at each iteration with respect to computed initial growth and guessed initial growth

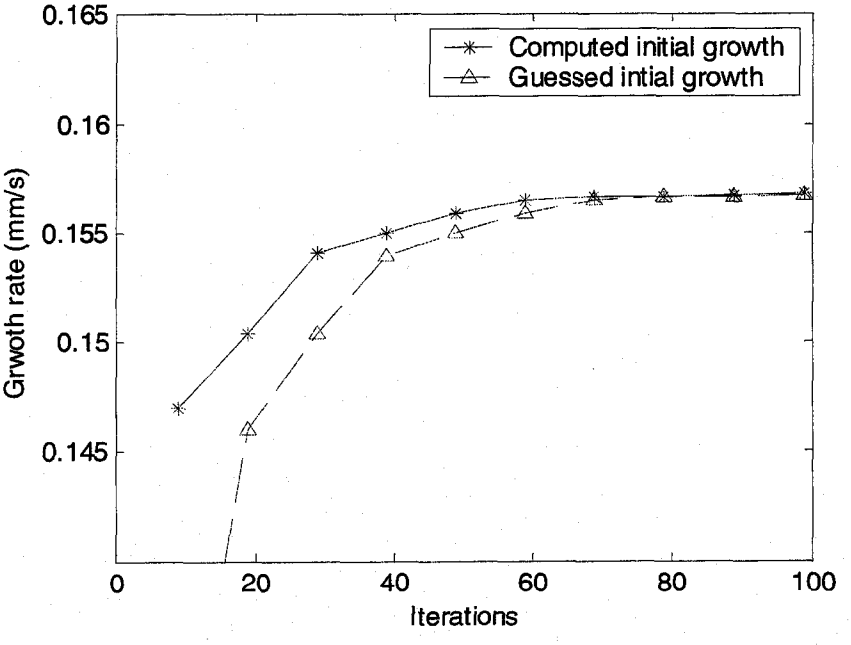

Figure 7.39 Growth rates at each iteration with respect to computed initial growth and guessed initial growth

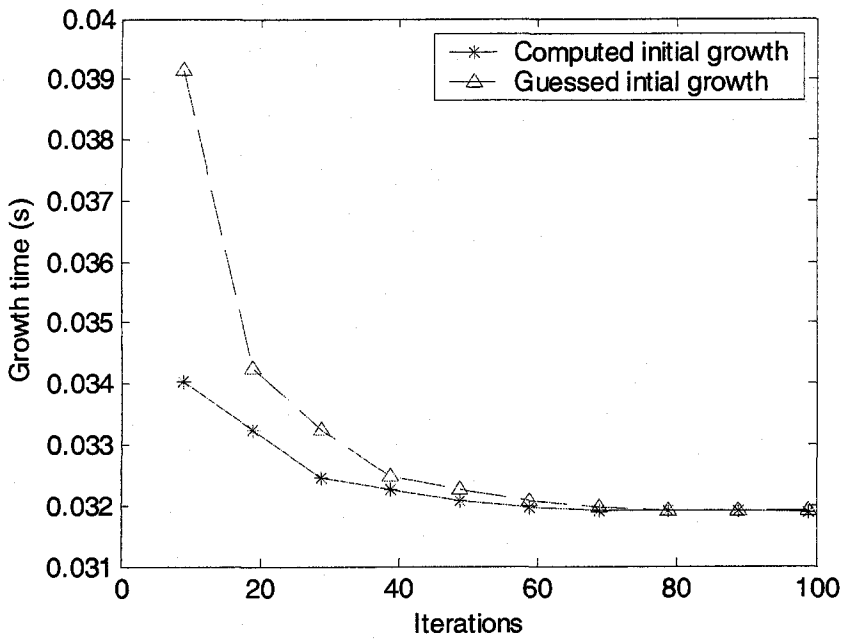

Figure 7.40 Growth time at each iteration with respect to computed initial growth and guessed initial growth

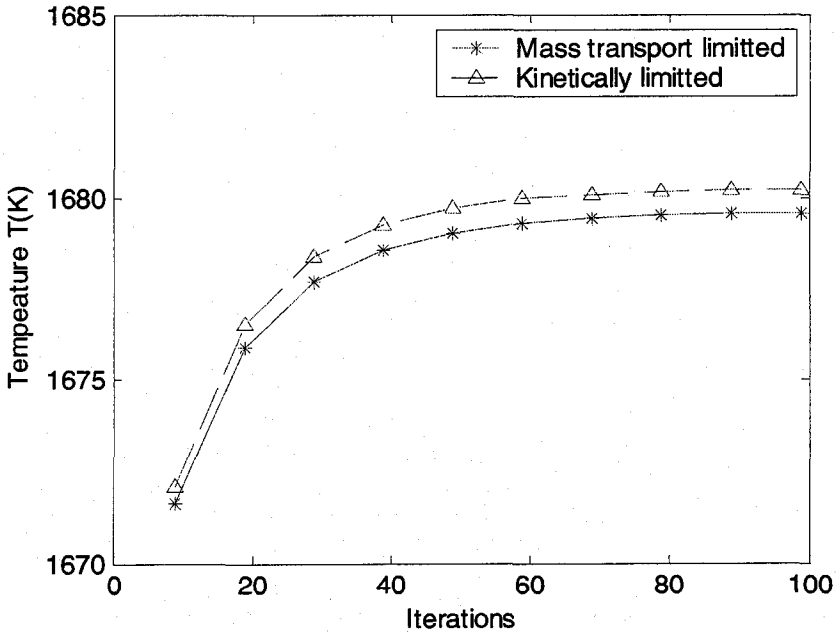

Figure 7.41 Temperature at the tip of the rod at each iteration with respect to mass transport limited deposition and kinetically limited deposition

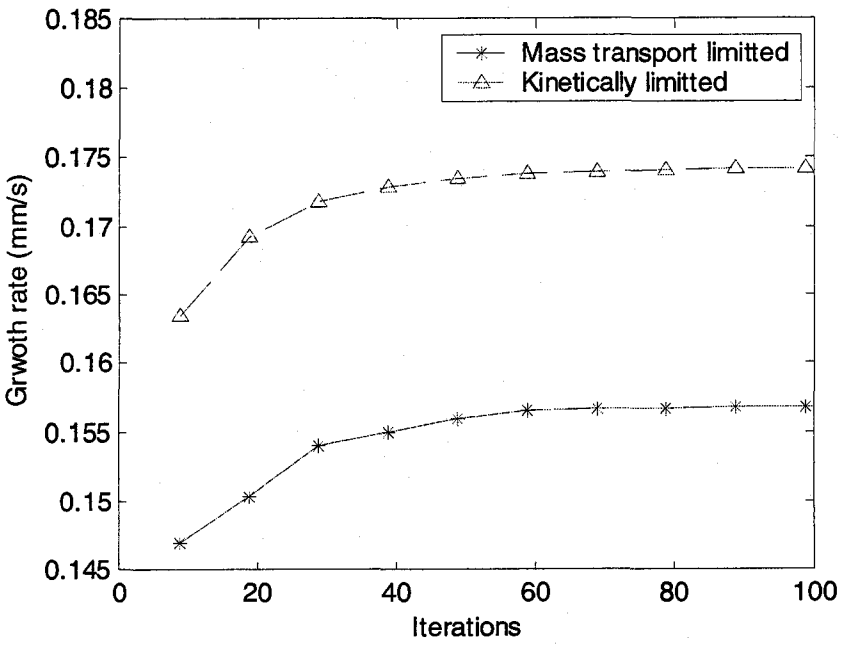

Figure 7.42 Growth rates at each iteration with respect to mass transport limited deposition and kinetically limited deposition

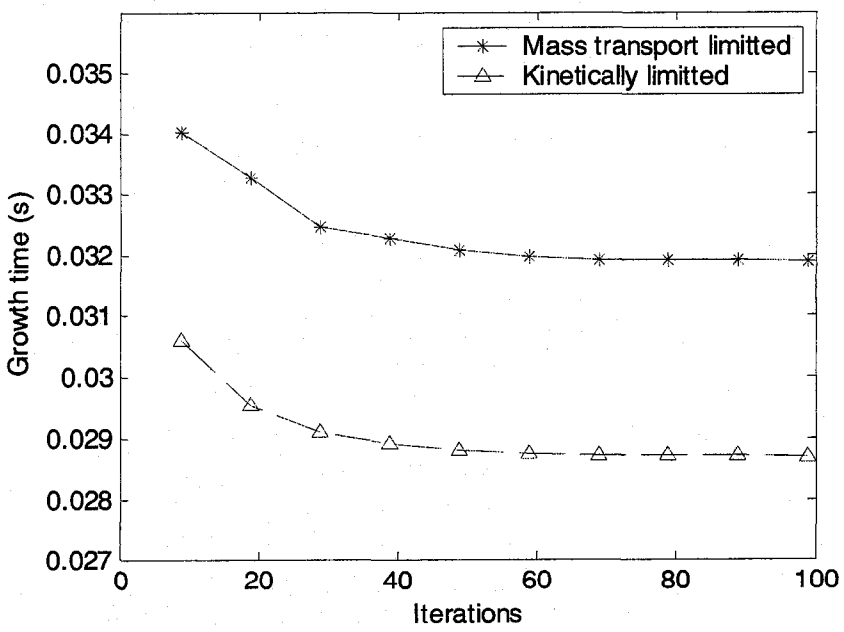

Figure 7.43 Growth time at each iteration with respect to computed or guessed initial growth

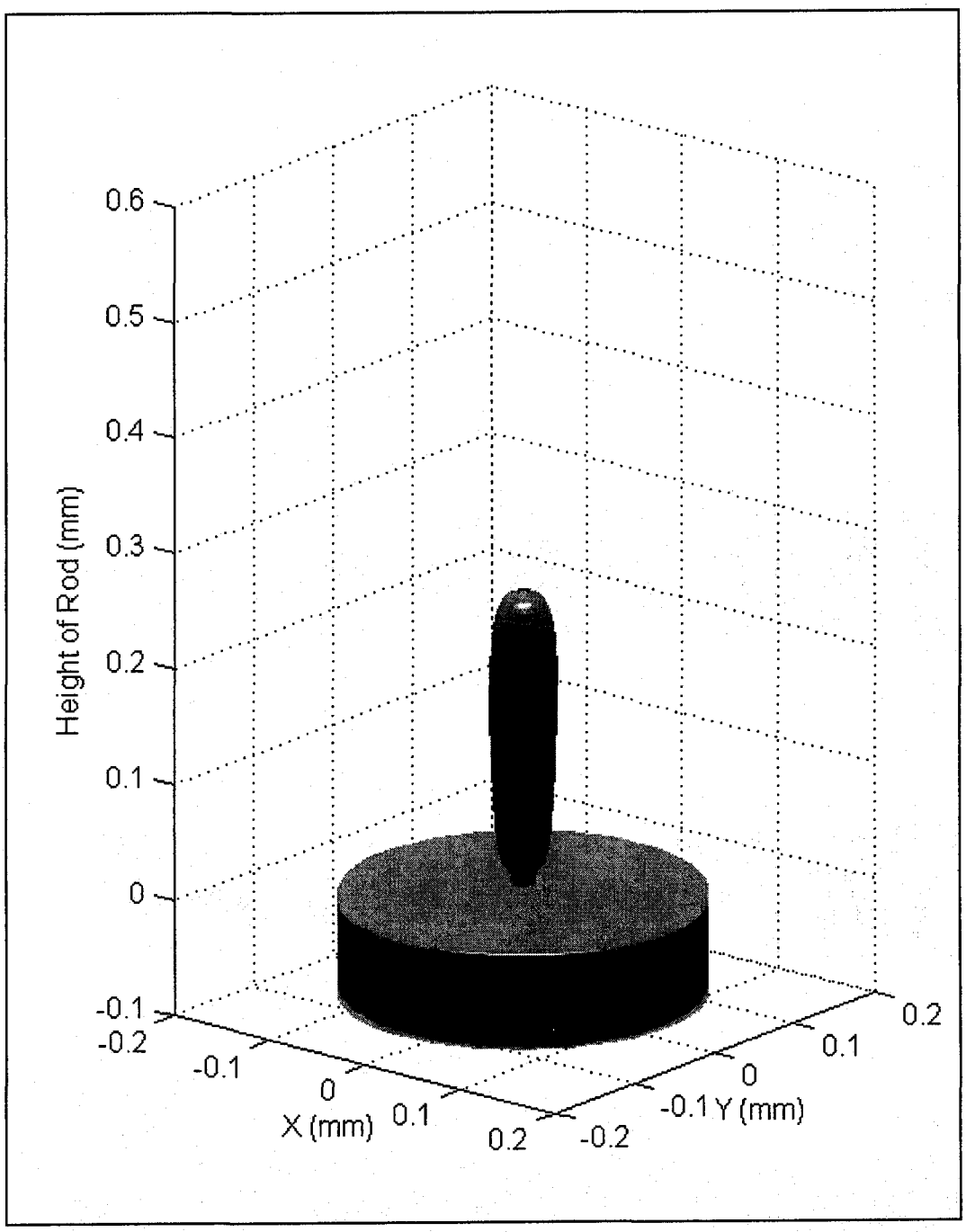

Figure 7.44 Predicted rod growth with the kinetic model (Iteration=50)

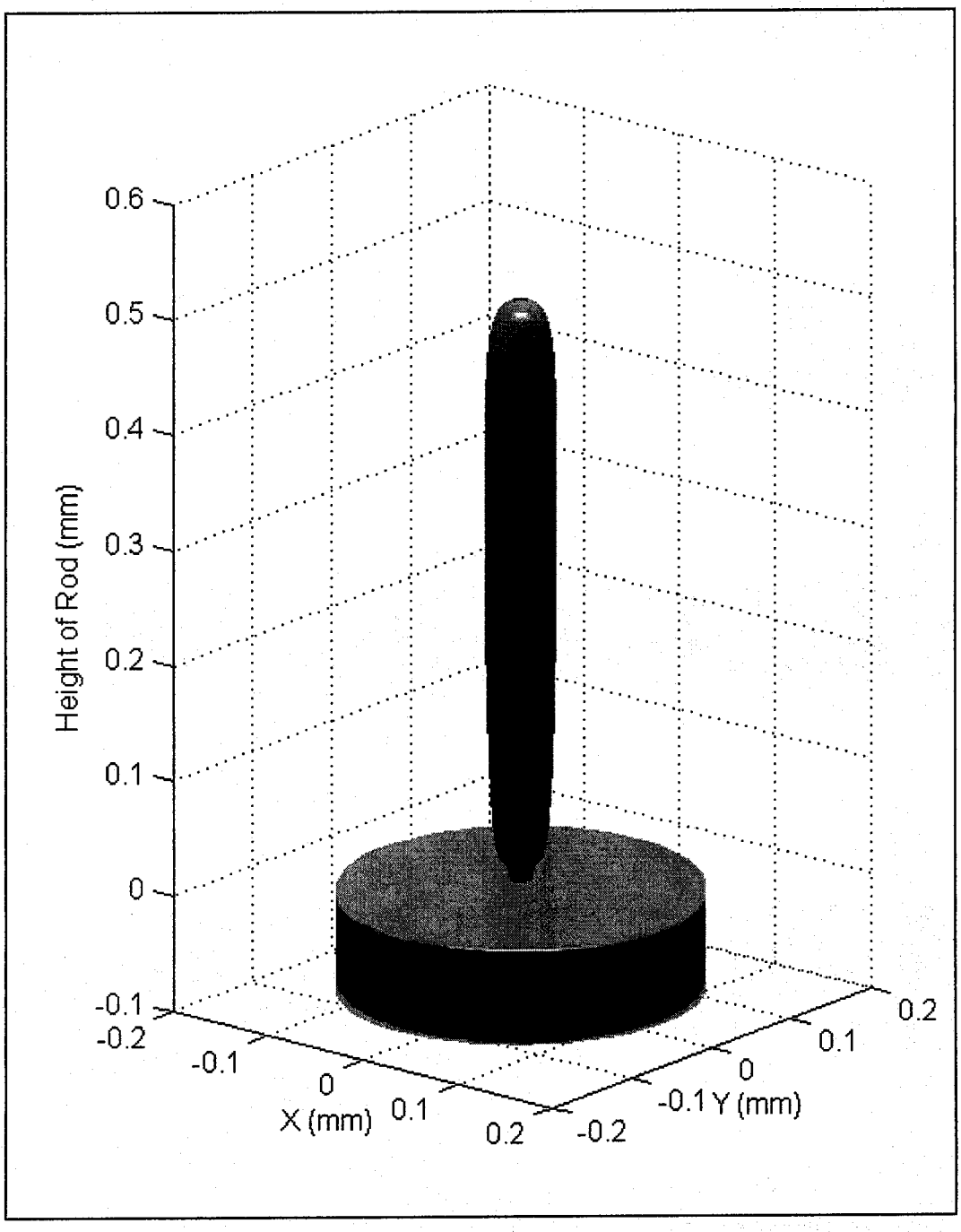

Figure 7.45 Predicted rod growth with the kinetic model (Iteration=100)

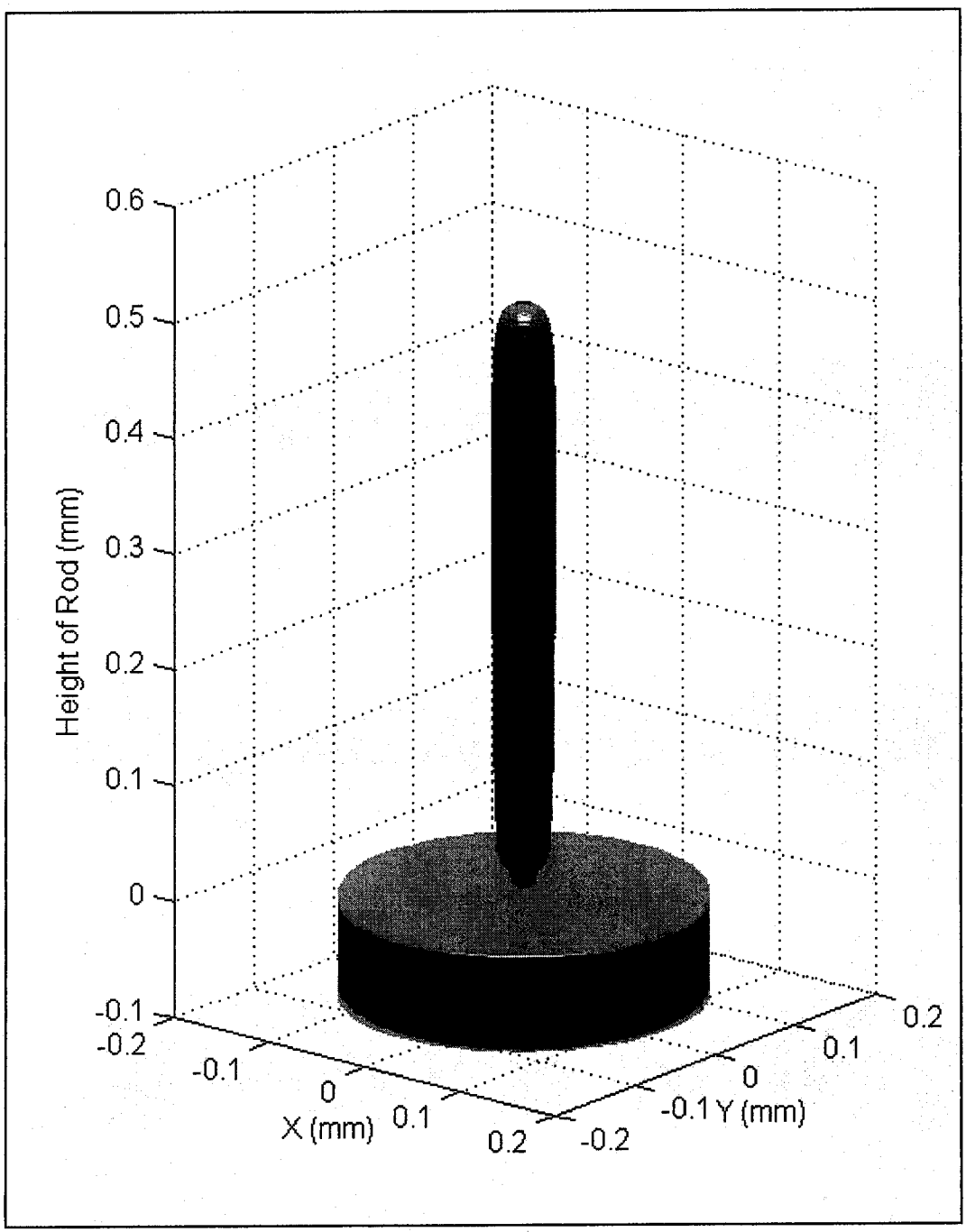

Figure 7.46 Predicted rod growth (P_0=0.02W, Iteration = 100)

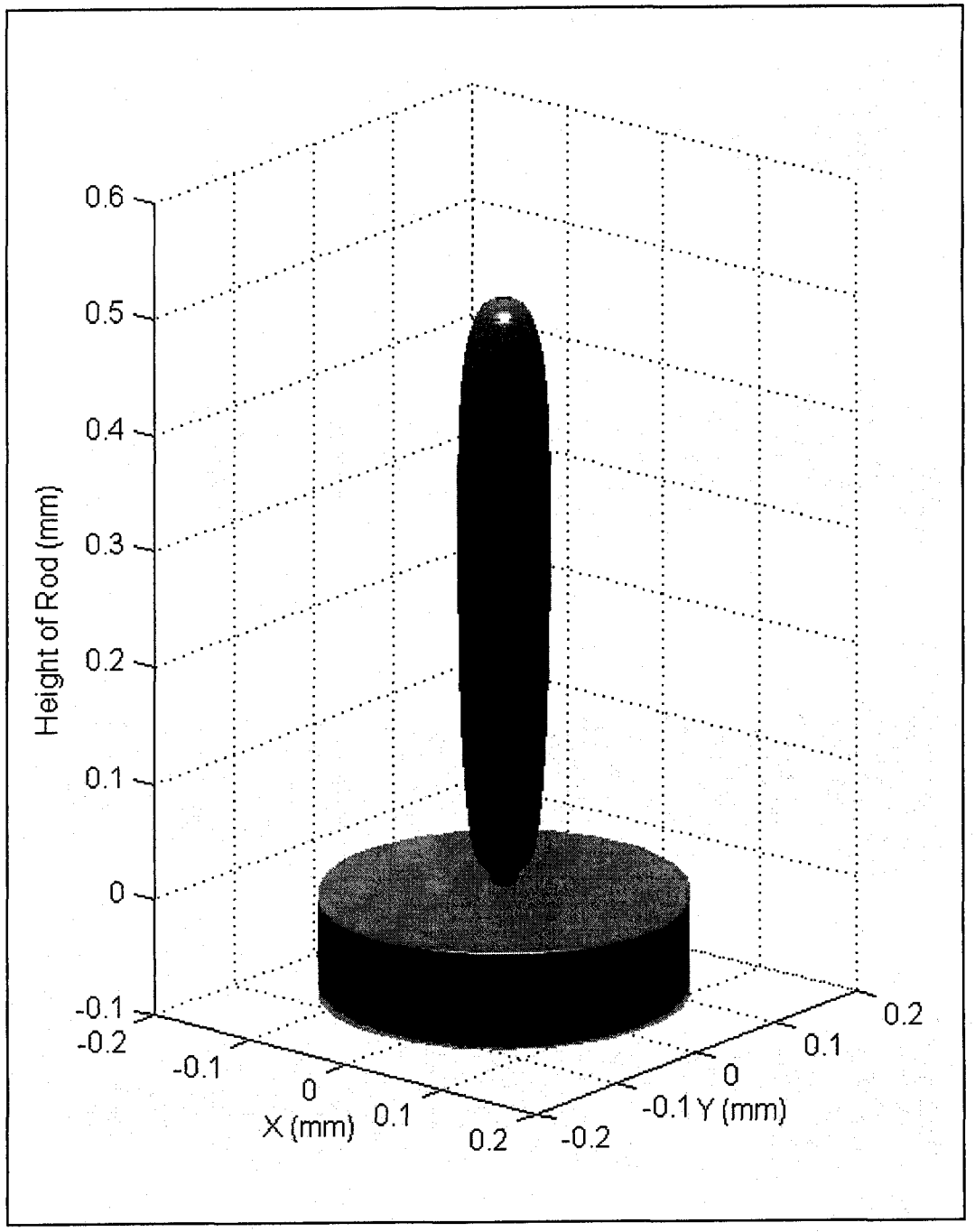

Figure 7.47 Predicted rod growth (P_0=0.05W, Iteration = 100)

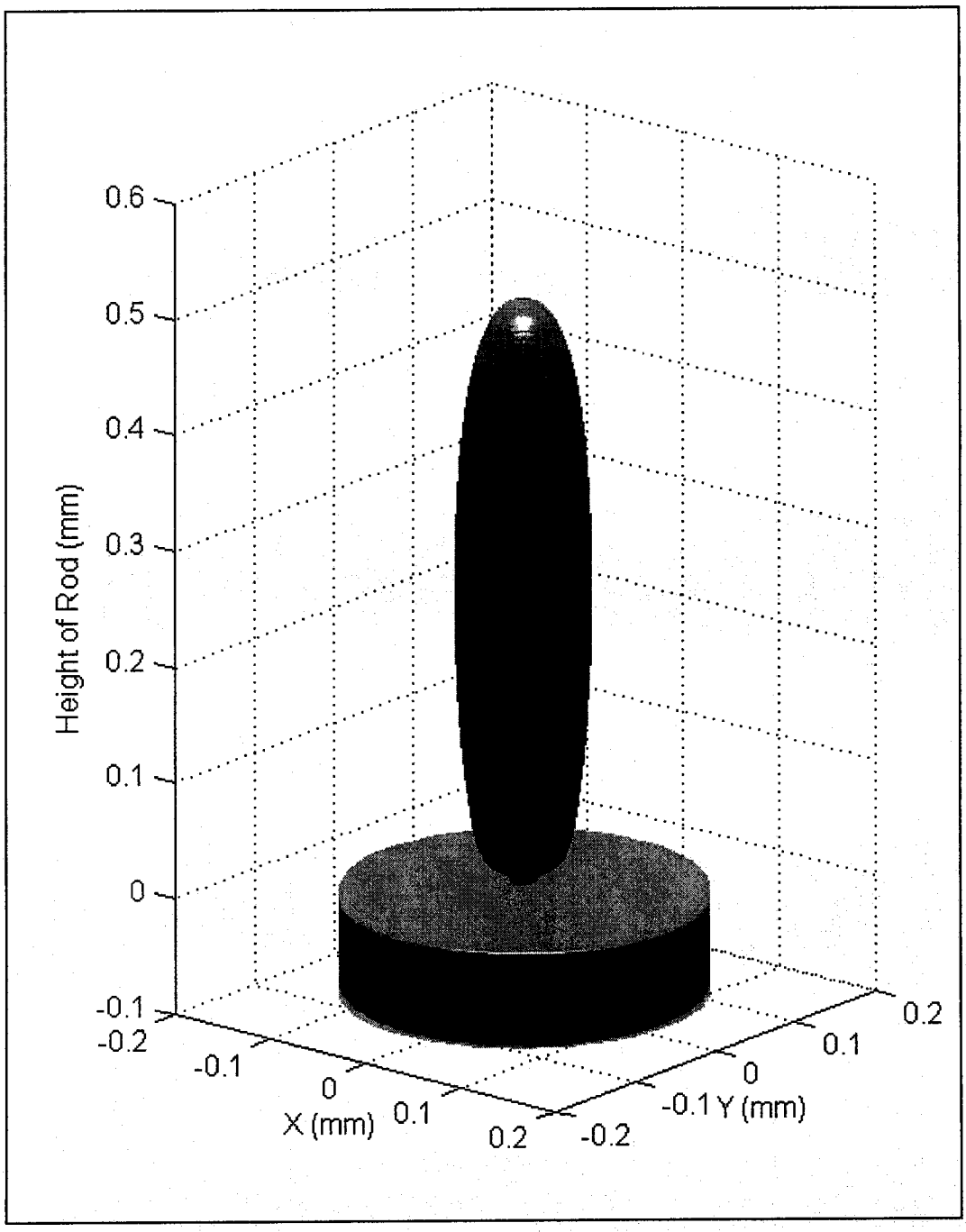

Figure 7.48 Predicted rod growth (P_0=0.10W, Iteration = 100)

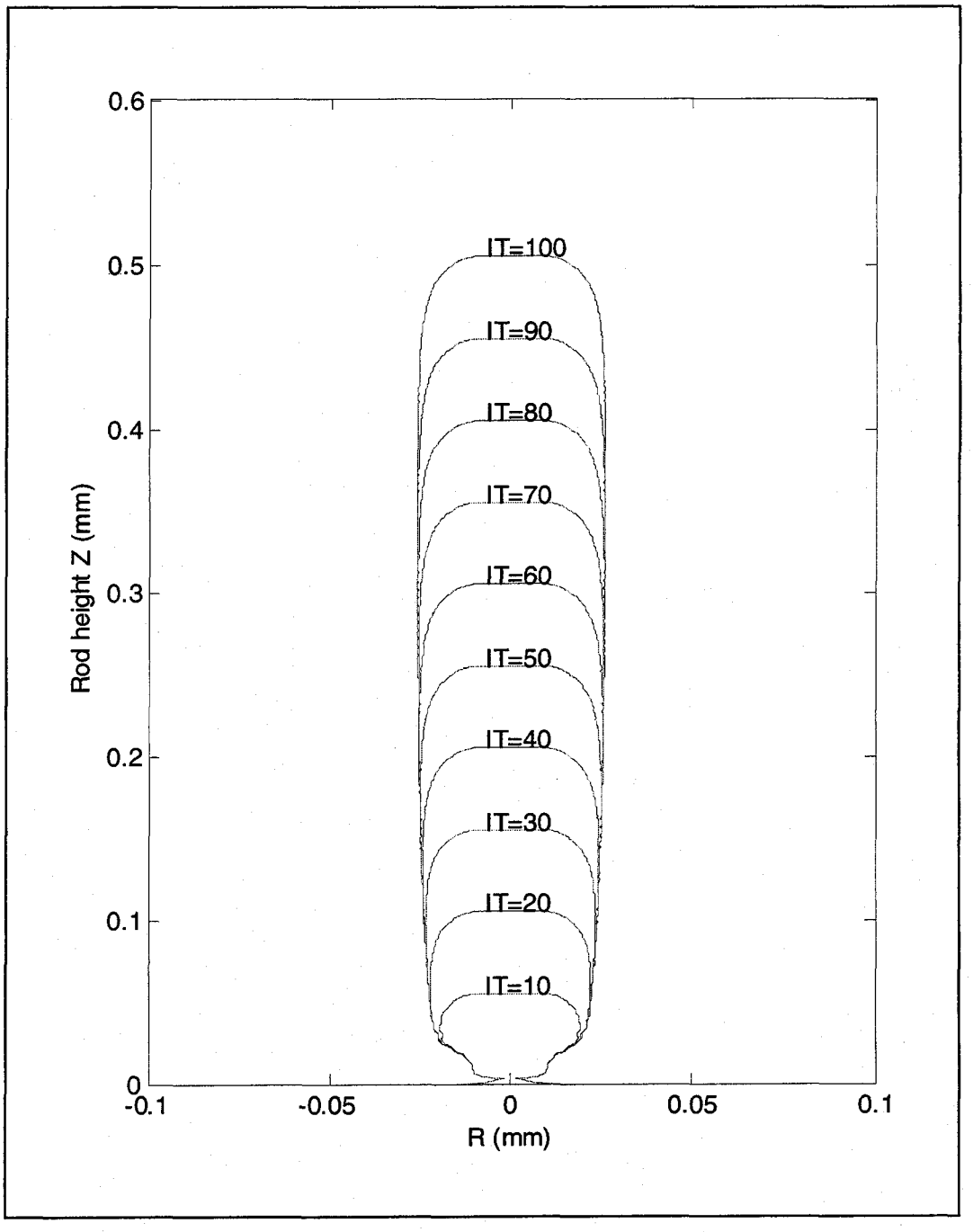

Fig. 7.49 Rod shapes with respect to different deposition stages (P_0=0.02W)

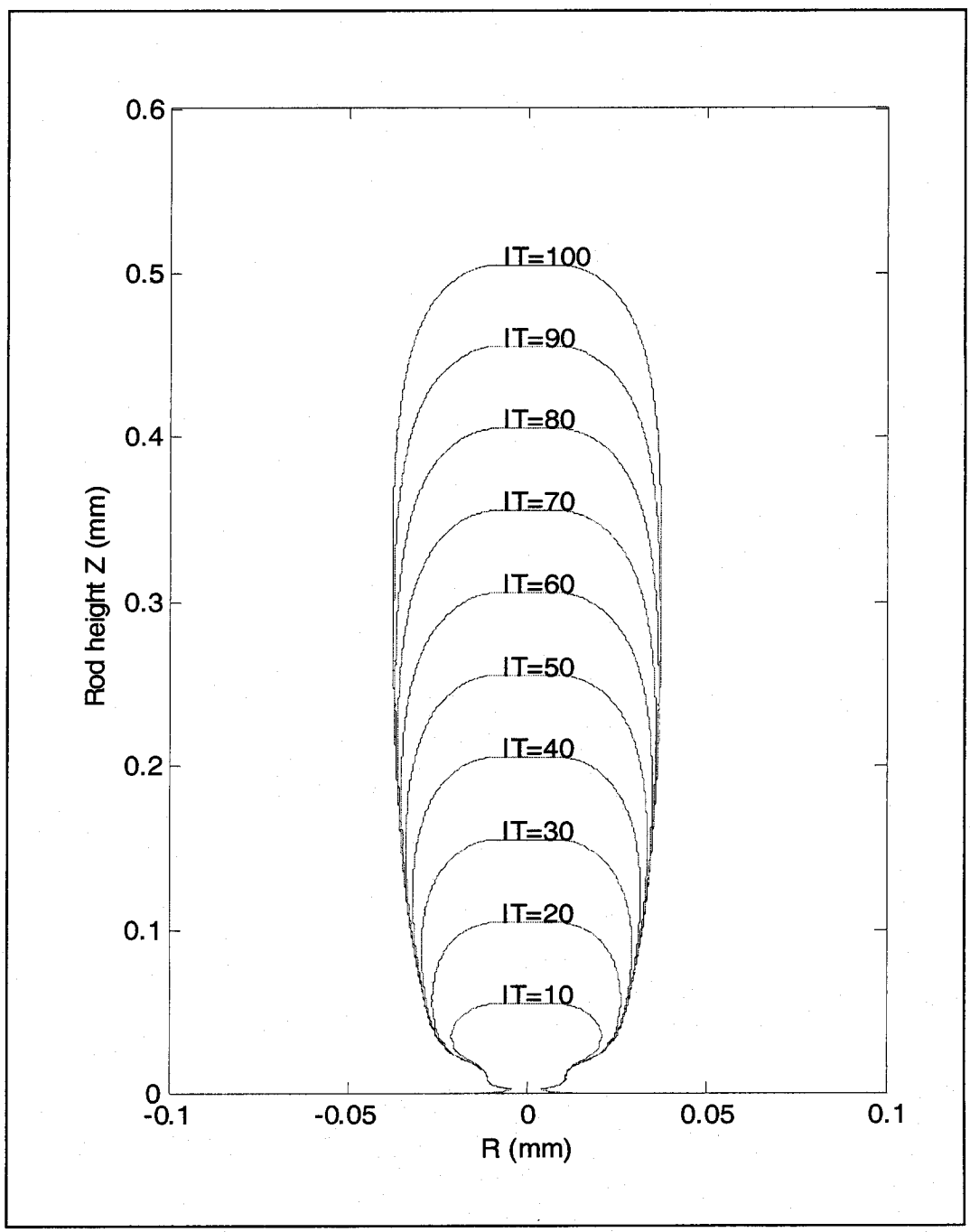

Fig. 7.50 Rod shapes with respect to different deposition stages (P_0=0.05W)

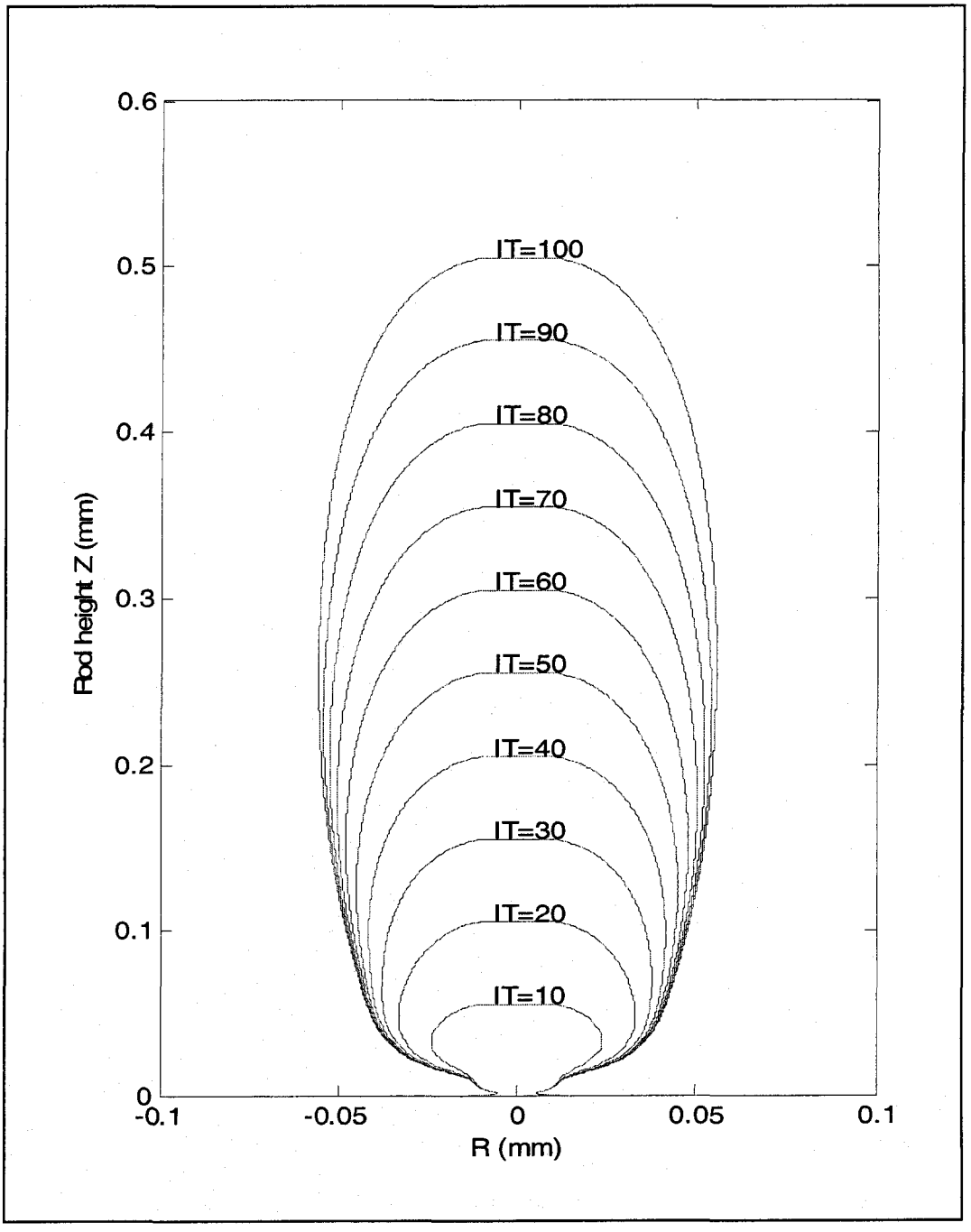

Fig. 7.51 Rod shapes with respect to different deposition stages (P_0=0.10W)

CHAPTER 8

SUMMARY AND CONCLUSION

Laser-induced Chemical Vapor Deposition (LCVD) is an emerging technique in free form fabrication with many practical applications. Usually a process is kinetically limited at low temperature and pressure, and the reaction rate rises exponentially with increasing temperature. While the surface temperature drives the deposition rate of a heterogeneous pyrolytic reaction, the rate obtained depends on the reaction activation energy and the ability of the precursor reactants and by-product to transport to and from the surface. To achieve precise control of the thermal deposition near the focus of a laser beam, specific contributions were made toward mathematical model development of the 3D-LCVD with both kinetically limited and mass transport limited reactions.

Some key contributions of this thesis are

1. A novel integrated three-dimensional mathematical model was developed not only to describe the heat transport in the deposit and substrate and growth rate, but also to simulate the gas-phase processing in the heated reaction zone and its effect on growth rate. The integrated model consisted of three components: the substrate, rod and gas-phase domain integrated together.
2. The gas-phase component is an adaptive domain attached to the top part of the rod. The part of the rod contained in the gas-phase domain is dynamically determined by the rod temperature distribution and the given threshold. The domain consists

of a solid part and a gas-phase part. The entire domain is automatically decomposed and each subdomain is indicated by different markers by which the computation process is controlled. The temperature and molar ratio distributions are predicted to determine the mass-transport limited growth rate in the gas-phase domain.

3. The substrate domain is included in the model to take into account the heat transfer toward the substrate from the interface between the substrate and rod. Most importantly, at the beginning, the laser beam is focused at the surface of the substrate and the induced temperature distribution determines the initial growth which then greatly affects the rod growth at successive stages.
4. A layer-by-layer axisymmetric model is used to simulate the temperature distribution and rod growth along the outward normal direction at each point on the rod surface. This model makes the process more predictable and easier to control by specifying the height of the rod and the number of total iterations. In this model, the natural convection is the primary heat loss mechanism.
5. Finite different methods (FDM) are proposed for solving the coupling governing equations and iterative algorithms are presented for simulating the interaction among heat transfer, growth rate, and gas-phase effect at each stage. The computation is stable, convergent and efficient.
6. The model is implemented using C++ code and can be easily installed and executed on different platforms. The computation in the gas-phase domain is encapsulated in a C++ class, and it is easy for users to choose either the integrated or the kinetic model to perform the computation.

7. High-performance computing technologies are used for the integrated model proposed. A row block decomposition technique is employed to partition the computational domains. Parallel algorithms are designed and implemented using standard C++ and MPI. The parallel computations are performed on both SGI Origin supercomputer and Windows XP. The actual speedups for the Jacobi, GS and SOR methods are obtained and their efficiencies analyzed. The parallel computation techniques can improve the performance.
8. Silane is chosen as the precursor to grow the axisymmetric rod and to demonstrate the capability of the integrated model. The integrated LCVD model and the corresponding numerical methods are applied to simulate the gas-phase reaction process, and predict heat transfer, molar ratio, initial and successive rod growths and growth time at each iteration. Rods with silicon as deposit and graphite as substrate are obtained with this model. This modeling approach may provide a useful means for investigating the effects of different model parameters, and, hence, for optimizing the LCVD process.
9. The prediction of initial growth is important because it is the starting point and determines the successive deposition process. Random guess or synthetic initial growth may result in different rod shapes.
10. The integrated model can provide more accurate prediction than the kinetic model. Usually a process is kinetically limited at low temperature and pressure and the reaction rate rises exponentially with increasing temperature. When the surface temperature increases to a certain level, the reaction proceeds rapidly. In this case, the ability of the precursor to arrive at the surface of the reaction zone is

insufficient to support the continued exponential increase with increasing temperature and the process passes into the mass-transport limited regime. The numerical results show that the gas-phase mass-transport may slow down the deposition process in which case more time will be needed to grow each layer (with height 0.0005mm).

11. Under the same computational conditions, a lower laser power may be used to grow a thin rod with a constant diameter while a lager laser power may be used to grow a fat rod with a changing diameter.

The complicated chemical and physical nature during the LCVD process determines the complexity in developing a three-dimensional model that (1) describes heat transfer in the gas-phase reaction, rod deposit, and substrate, (2) considers the gas-phase reaction and mass-transport limited growth rate, and (3) predicts the changing geometry of the rod at each deposition stage.

In light of the above work, it is possible to extend the integrated model in the following directions:

1. Experimental work is strongly suggested to verify the model and calibrate the parameters used in the model.
2. A time-dependent 3D integrated model may be developed to simulate the entire process. This may make it possible to simulate time-dependent heat transfer and growth and achieve more accurate results. The assumption of a stable temperature distribution at each deposition stage relies on layer partition and growth time needed to grow each layer. If the layer is too larger, the temperature may not be

able to reach a stable status before the next layer is grown. This improvement will broaden the range of the applications in which the integrated model can be used.

3. An integrated inverse model may be developed to control the deposition process in order to obtain a rod with the desired geometry. Given the geometry, determining the multiple parameters, such as laser power and thermal properties, is a challenging problem.
4. The integrated model includes the simulation of substrate. The boundary conditions on the interface between rod and substrate can take into account the heat transfer automatically. Thus, it is convenient to use different precursors and substrate to grow a rod by changing the physical properties in the model.
5. The full 3D integrated model may need more CPU time to achieve accurate and fast modeling of the LCVD process. The component-based model proposed in the thesis can be extended to perform distributed or parallel computing. For example, one processor computes the gas-phase temperature distribution and molar ratio, one processor calculates the temperature distribution in the substrate, one processor computes predicted values for the temperature distribution in the rod and rod growth, and one processor integrates the results from other processors and controls the entire process.

REFERENCES

[Abraham 1987] E. Abraham, and J. M. Halley. "Some Calculations of Temperature Profiles in Thin Films with Laser Heating," *J. Appl. Phys. A*, 42, (1987), pp. 279-285.

[Abtahi 1986] A. Abtahi, P. F. Braunlich, and P. Kelly. "Theory of Transient Temperature Response of a Two-Layer System Heated with a Localized Laser Beam," *J. Appl. Phys.* 60, (1986), pp. 3417-3421.

[Allen 1985] S.D. Allen, R. Y. Jan, S. M. Mazuk, and S. D. Vernon. "Real Time Measurement of Deposition Initiation and Rate in Laser Chemical Vapor Deposition," *J. Appl. Phys.* 58, (1985), pp. 327-331.

[Allen 1986] S. D. Allen, J. A. Goldstone, J. P. Stone, and R. Y. Jan, "Transient Nonlinear Laser Heating and Deposition: A Comparison of Theory and Experiment," *J. Appl. Phys.* Vol. 59, No. 5, (1986), pp. 1653-1657.

[Arnord 1993] N. Arnold, R. Kullmer and D. Bäuerle, "Simulation of Growth in Pyrolytic Laser-CVD of Microstructure I. One-Dimensional Approach," *Microelectronic Engineering*, Vol. 20, (1993), pp. 31-41.

[Arnold 1993.2] N. Arnold and D. Bäuerle, "Simulation of Growth in Pyrolytic Laser-CVD of Microstructure II. Two-Dimensional Approach," *Microelectronic Engineering*, Vol. 20, (1993), pp. 43-54.

[Bartholomeusz 1988] B. J. Bartholomeusz, "Thermal Response of a Laser-Irradiated Metal Slab," *J. Appl. Phys.*, Vol. 64. No. 8, (1988), pp. 3815-3819.

[Bäuerle 1984] D. Bäuerle, "Laser-Induced Chemical Deposition," in *Laser Processing and Diagonostics, Springer Series in Chemical Physical 39*, pp. 166-182, Springer, New York, 1984.

[Bäuerle 1986] D. Bäuerle, *Laser Processing and Chemistry*, Springer-Verlag, New York, (1986).

[Bäuerle 1990] D. Bäuerle, B. Luk'yanchuk, and K. Piglmayer, "On the Reaction Kinetics in Laser-Induced Pyrolytic Chemical Processing," *J. Appl. Phys. A*, Vol. 50, (1990), pp. 385-396.

[Baum 1989] T. H. Baum, C. E. Larson, and R. L. Jackson, "Laser-Induced Chemical Vapor Deposition of Aluminum," *J. Appl. Phys. Lett.*, Vol. 55, No. 12, (1989), pp. 1264-1266.

[Bloembergen 1978] N. Bloembergen, "Foundations of Laser-Solid Interactions, Laser-Solid Interactions and Laser Processing," *AIP Conf. Proc.*, No. 50, (1978), pp. 1-9.

[Boman 1995] M. Boman and D. Bäuerle, "Laser-Assisted Chemical Vapor Deposition of Boron," *J. of Chinese Chemical Society*, Vol. 42, (1995), pp. 405-411.

[Boyd 1984] I. W. Boya, T. D. Binnie, J. I. B. Wilson and M. J. Colles, "Absorption of Infrared Radiation in Silicon," *J. Appl. Phys.*, Vol. 55, No. 8, (1984), pp. 3061-3063.

[Brugger 1972] K. Brugger, "Exact Solution for the Temperature Rise in a Laser-Heated Slab," *J. Appl. Phys.*, Vol. 43, No. 2, (1972), pp. 577-583.

[Burden 1997] R. L. Burden and J. D. Faires, *Numerical Analysis*, Sixth Edition, Brooks, (1997).

[Burgener 1982] M. L. Burgener and R. E. Reedy, "Temperature Distributions Produced in a Two-layer Structure by a Scanning CW Laser or Electron Beam," *J. Appl. Phys.*, Vol. 53, No. 6, (1982), pp. 4357-4363.

[Calder 1982] I. D. Calder and R. Sue, "Modeling of CW Laser Annealing of Multilayer Structure," *J. Appl. Phys.* Vol. 53, No. 11, (1982), pp. 7545-7550.

[Cardslaw 1959] H. S. Cawslaw, J. C. Jaeger, *Conduction of Heat in Solid*, 3ed Ed., Clarendon Press, Oxford, (1959), p. 264.

[Chang 1996] H. Chang, L. Lee, R. Huang, et al., "Physical and Chemical Properties of the Cylindrical Rods SiCx (x=0.3-1.2) Growth from $Si(CH_3)CL_2$ by Laser Pyrolysis," *Material Chemistry and Physics*, Vol. 44, (1996), pp. 59-66.

[Cheburaeva 1986] P. F. Cheburaeva and I. N. Chaporova, "Role of Tantalum in the Tic-WC-TaC-Co Hard Metals. I. Efect of Tantalum Concentration on the Composition and Properties of the Carbide and Cobalt Phase in the TiC-WC-Tac-Co Hard Metals," Translated from *Poroshkovaya Metallurgiya*, No. 4, (1986), pp. 75-79.

[Chou 1989] W. B. Chou, M. N. Azer, and J. Mazunder, "Laser Chemical Vapor Deposition of Ti from TiBr4," *J. Appl. Phys.*, Vol. 66, No. 1, (1989), pp. 191-195.

[Dai 1999] W. Dai, R. Nassar, C. Zhang, S. Shabanian, and J. Maxiwell, "A Numerical Model for Simulating Axisymmetric Rod Growth in Three-Dimensional Laser Chemical Vapor Deposition," *J. Numerical Heat Transfer*, Vol. 36, (1999), pp. 251-262.

[David 1988] D. E. Kotecki and I. P. Herman, "A Real Time Monte Carlo Simulation of Thin Film Nucleation in Localized-Laser Chemical Vapor Depositin," *J. Appl. Phys.* Vol. 64, No. 10, (1988), pp. 4920-4942.

[Doppelbauer 1984] J. Doppelbauer, G. Leyendecker, and D. Bäuerle, "Raman Diagnostics of Heterogeneous Chemical Processes, Determinationof Local Concentrations," *J. Appl. Phys. B*, Vol. 33, (1984), pp. 141-147.

[Doppelbauer 1987] J. Doppelbauer and D. Bäuerle, "Kinetics of Laser-Induced Pyrolytic Chemical Processes and the Problem of Temperature Measurements, in Interfaces under Laser Irradiation," ed. by L. D. Laude, D. Bäuerle and M. Wautelet, NATO ASI Series (Nijhoff, Dordrecht 1987) p.277.

[El-Adawi 1986] M. K. El-Adawi and E. F. Elshehaway, "Heating a Slab Induced by a Time-Dependent Laser Irradiance – an Exact Solution," *J. Appl. Phys.*, Vol. 60, No. 7, (1986), pp. 2250-2255.

[Falk 1997] F. Falk, J. Meinschien, G. Mollekopf, K. Schuster, and H. Stafast, "CNx Thin Films Prepared by Laser Chemical Vapor Deposition," *Material Science and Engineering B,* Vol. 46, (1997), pp. 89-91.

[Freeman 1992] T.L. Freeman and C. Phillips, *Parallel Numerical Algorithms*, Prentice Hall International (UK) Ltd., (1992).

[Garrido 1991] C. Garrido, B. Leon and M. Perez-Amor, "A Model to Calculate the Temperature Induced by a Laser," *J. Appl. Phys.*, Vol. 69, No. 3, (1991), pp. 1133-1140.

[Ghez 1975] R. A. Ghez and R. A. Laff, "Laser Heating and Melting of Thin Films on Low-Conductivity Substrate," *J. Appl. Phys.*, Vol. 46, No. 5, (1975), pp. 2103-2110.

[Grama 2003] A. Grama, A. Gupta, G. Karypis and V. Kumar, *Introduction to parallel computing*, Addison Wesley, (2003).

[Harrach 1977] R. J. Harrach, "Analytical Solution for Laser Heating and Burnthrough of Opaque Solid Slabs," *J. Appl. Phys.,* Vol. 48, No. 6, (1977), pp. 2370-2383.

[Imen 1989] K. Imen, J. Y. Lin, and S. D. Allen, "Steady-State Temperature Profile in Thermally Thin Substrate induced by Arbitrary Shaped Laser Beams," *J. Appl. Phys.* Vol. 66, No. 2, (1989), pp. 488-491.

[Incropera 1985] Frank P. Incropera and David P. DeWitt, *Fundamentals of Heat and Mass Transfer,* Second Edition, John Wiley & Sons, (1985).

[Jang 1998] T. Jang, W. Moon, et al, "Effect of Temperature and Substrate on the Growth Behaviors of Chemical Vapor Deposited a Films with Dimethylethylamine Alane Source," *Thin Solid Films*, Vol. 333, (1989), pp.137-141.

[Jellison 1983] G. E. Jellison and F. A. Modine, "Optical Functions of Silicon between 1.7 and 4.7 eV at Elevated Temperatures," *Physical Review B*, Vol. 27, No. 12, (1983), pp. 7466-7472.

[Kar 1989] A. Kar and J. Mazumder, "Three-Dimensional Transient Thermal Analysis for Laser Chemical Vapor Deposition on Uniformly Moving Finite Slab," *J. Appl. Phys.* Vol. 65, No. 8, (1989), pp. 2923-2934.

[Kar 1991] A. Kar, M. N. Azer and J. Mazumder, "Three-Dimensional Transient Mass Transfer Model for Laser Chemical Vapor Deposition of Titanium Finite Slab," *J. Appl. Phys.* Vol. 69, No. 2, (1991), pp. 757-765.

[Karniadakis 2003] G. E. Karniadakis and R. M. Kirby, *Parallel Scientific Computing in C++ and MPI*, Cambridge University Press, (2003).

[Kirichenko 1990] N. Kirichenko, K. Piglmayer, and D. Bäuerle, "On the Kinetics of Non-Equimolecular Reactions in Laser Chemical Processing," *J. Appl. Phys. A,* Vol. 51, (1990), pp. 498-507.

[Lan, 2003] H. Lan, R. Nassar, W. Dai and C. Zhang, "Mathematical model for simulating axisymmetric rod growth with kinetically limited and mass transport limited rates," *Micromaching and Microfabrication Process Technology VIII, Proc SPIE*, pp. 549-560, CA 2003.

[Lehmann 1994] O. Lehmann and M. Stucke, "Three-Dimensional Laser Direct Writing of Electrically Conducting and Isolating Microstructures," *Materials Letter*, Vol. 21, (1994), pp. 131-136.

[Levoska 1989] J. Levoska, T. T. Rantala and J. Lenkkeri, "Numerical Simulation of Temperature Distribution in Layered Structures During Laser Processing," *Applied Surface Science*, Vol. 36, (1989) pp. 12-22.

[Leyendekecker 1983] G. Leyendekecker, J. Doppelbauer, and D. Bäuerle, "Raman Diagnostics of CVD System: Determination of Local Temperature," *J. Appl. Phys. A*, Vol. 30, (1983), pp. 237-243.

[Liau 1994] Z. L. Liau, D. W. Nam, and R. G. Waarts, "Tolerances in Microlens Fabrication by Multilevel Etching and Mass-Transport Smoothing," *Applied Optics*, Vol. 33, No. 31, (1994), pp. 7371-7376.

[Maxwell 1996] J. Maxwell, *Three-Dimensional Laser-Induced Pyrolytic Modeling, Growth Rate Control, and Application to Micro-Scale Prototyping*, Ph.D. Thesis, Rensselaer Polytechnic Institute, Troy, New York, (1996).

[Mizunami 1995] T. Mizunami, N. Toyama, and T. Sakaguchi, "Laser-Energy Dependence of Optical Emission from Radical and Atoms in Laser-Induced Chemical-Vapor Deposition of SiC," *J. Appl. Phys.* Vol. 78, (1995), pp. 3525-3527.

[Mansuripur 1982] M. Mansuripur, et al., "Laser-Induced Local Heating of Multilayers," *Applied Optics*, Vol. 21, No. 6, (1982), pp. 1106-1114.

[Nassar 2000] R. Nassar, W. Dai, C. Zhang, H. Lan and J. Maxwell, "A Mathematical Model for Process Control in Laser Chemical Vapor Deposition," *Proceeding of the Third International Conference on Modeling and Simulation of Microsystems*, San Diego, California, (2000), pp. 517-519.

[Nassar 2002] R. Nassar, W. Dai, and Q. Chen, "An axisymmetric numerical model for simulating kinetically limited growth of a cylindrical rod in 3d laser-induced chemical vapor deposition," *Journal of Material Science and Technology*, vol. 18, (2002), pp. 127-132.

[Oh 1985] J. E. Oh, N. J. Ianno and A. U. Ahamed, "Temperature Profiles Induced by a Stationary CW Laser Beam in a Multi-Layer Structure: Applications to Solar Cell Interconnect Welding," *Applied Physics Communications*, Vol. 5, No. 3, (1985), pp. 113-138.

[Paek 1973] U. C. Paek and A. Kestenbaum, "Thermal Analysis of Thin-Film Micormachining with Lasers," *J. Appl. Phys.*, Vol. 44, No. 55, (1973), pp. 2260-2268.

[Pacheco 1997] P.S. Pacheco, *Programming with MPI*, Morgan Kaufmann Publishers, Inc., (1997).

[Perecherla 1988]A. Perecherla and W. S. Williams, "Room-Temperature Thermal Conductivity of Cemented Transition-Metal Carbides," *J. Am. Ceram. Soc.*, Vol. 71, No. 12, (1988), pp.1130-33.

[Peterson 1989] G. P. Peterson and L. S. Fletcher, "On the Thermal Conductivity of Dispersed Veramics," *J. of Heat Transfer*, Vol. 111, (1989), pp. 824-829.

[Piglmayer 1984] K. Piglmayer, J. Doppelbauer, and D. Bäuerle, "Temperature Distribution in CW Laser Induced Pyrolytic Deposition," *Mat. Res. Soc. Symp. Proc.* Vol. 29, (1984), pp. 47-54.

[Scholl 1982] M. S. Scholl, "Target Temperature Distribution Generated and Maintained by a Scanned Laser Beam," *Applied Optics*, Vol. 21, No. 12, (1982), pp. 2147-2152.

[Seigel 1992] Seigel, R., Howell, J. R., *Thermal Radiation Heat Transfer, 3rd Ed.*, Hemisphere Publishing Corp., Boston, (1992), p.113.

[Shappur 1987] F. Shappur and S. D. Allen, "Experimental Determination of Laser Heated Surface Temperature Distribution," *Appl. Phys. Lett.* Vol. 50, No. 12, (1987), pp. 723-724.

[Skouby 1988] D. C. Skouby, K. F. Jensen, "Modeling of Pyrolytic Laser-Assisted Chemical Vapor Deposition: Effects of Kinetics and Choice of Substrate," *Material Research Society Symposium Proceedings*, Vol. 101, Laser and particle-Beam Chemical Processing for Microelectronics, (1998), pp. 107-113.

[Suh 1984] S. Y. Suh and D. L. Anderson, "Latent Heat Effect of Pulsed Laser Beam Induced Temperature Profiles in Optical Recording Thin Films," *Applied Optics*. Vol. 23, No. 22, (1984).

[Tamir 1995] S. Tamir, Y. Komem, M. Eizenberg and J. Zahavi, "Growth Mechanism of Silicon Films Produced by Laser-Induced Chemical Vapor Deposition," *Thin Solid Firms*, Vol. 261, (1995), pp. 251-255.

[Wang 1996] Q. Wang, Y. Zhang and D. Gao, "Theoretical Study on the Fabrication of a Microlens Using the Excimer Laser Chemical Vapor Deposition Technique," *Thin Solid Films*, Vol. 287, (1996), pp.243-246.

[Zhang 2003] C. Zhang, W. Dai, R. Nassar and H. Lan, "Inverse model for optimizing the process of fabricating a microstrucutre," *Micromaching and Microfabrication Process Technology VIII, Proc SPIE*, pp. 540-548, 2003.

[Zhang 2004] C. Zhang, Y. Ye, A. Ali and H. Lan, "An adaptive load balancing approach to parallel optical image reconstruction systems," *proceedings of the 8th World Multiconference on Systemics, Cybernetics and Informatics* (SCI 2004), Volume IX, (2004), pp. 212-217.